MOCVD Growth and Characterisation of Semi-polar (11-22) GaN on Stripes Patterned Silicon Substrates for III-nitrides Based Optoelectronics

Xuanming Zhao

The University of Sheffield
Faculty of Engineer
Department of Electronic Electrical Engineering
Centre for GaN Materials and Devices
Supervisor: Professor Tao Wang

A thesis submitted for the degree of Doctor of Philosophy
November 2021

Abstract

III-nitride semiconductors have shown superior performance on solid-state lighting and advance optoelectronic devices due to the wide bandgap and excellent properties. In addition, the merits of silicon substrate such as low cost-effect, large scalability and technology of integration have enabled the III-nitrides grown on silicon substrates to draw extensive attention in recent years. Currently, the III-nitrides grown on silicon substrates are dominated by conventional polar c-plane ones. In addition to some growth challenges for GaN-on-Si, such as stress issue and Ga melt-back etching, polarization-induced piezoelectric fields within active regions, which separate the electrons and holes, hinder the achievement of high-efficiency optoelectronic devices especially in the long-wavelength range. III-nitrides along semi-polar orientations are expected to have great potential in reducing polarization, increasing internal quantum efficiency, and enhancing indium incorporation efficiency (especially (11-22) GaN). Thus, this project aims to achieve high crystal quality semi-polar (11-22) GaN film on Si by solving these issues. A two-step approach has been developed, namely adopting techniques of thick AlN layer and selective area growth to grow semi-polar (11-22) GaN film on patterned (113) silicon substrate without any Ga melt-back etching occur during a long period of high-temperature condition. The corresponding characterizations have confirmed that the (11-22) GaN film has a low basal stacking faults and high crystal quality by means of photoluminescence (PL) measurements, X-ray diffraction and optical pumping measurements.

Through an investigation on the mechanism of Ga melting-back etching, another approach, with simplified one-step, has been well-developed to achieve high quality (11-22) GaN film on patterned (113) silicon substrate by means of a specially designed stripe pattern. The influence of trench depth, initial growth temperature and AlN buffer layer thickness have been investigated. InGaN-based green LEDs subsequently grown on these semi-polar (11-22) GaN-on-Si are obtained. Excitation power-dependent photoluminescence measurements have confirmed a significant reduction of polarization-induced piezoelectric fields on the semi-polar (11-22) LEDs. Furthermore, comparing with conventional c-plane LEDs, electroluminescence of semi-polar (11-22) LEDs have demonstrated a more stable external quantum efficiency with increasing injection current.

Furthermore, an InGaN/GaN superlattice prelayer is introduced in the semi-polar (11-22) green LED structure to improve the efficiency of LEDs. The influence of the superlattice prelayer has been investigated via temperature-dependent photoluminescence, time-resolved photoluminescence and cathodoluminescence measurements. An enhancement in optical performance has been observed in the sample with a superlattice prelayer structure compared to the reference sample without it. However, the enhancement of internal quantum efficiency for semi-polar (11-22) with a superlattice prelayer is far lower compared to the conventional c-plane case. The main cause is considered as the impact of extra misfit dislocations generated at the boundary between GaN buffer and superlattice prelayer.

Acknowledgements

It is a journey of hardship in pursuing this PhD degree throughout my past few years studying. Fortunately, despite many obstacles, I have made it all the way to this final part of my PhD study as I have received much support and encouragement from many people. At this point, I would like to express my sincere appreciations to these people who have spent their generous help in achieving my academic accomplishments.

First and foremost, I would like to express my deepest sense of gratitude to my supervisor Professor Tao Wang for the selfless support and timely guidance throughout my whole research project. Also, he is the tutor of my life who provides extremely precious experience to guide and shape the trajectory of my life.

I would like to thank Dr. Jie Bai for her kind help with device fabrication training and generous support on my LEDs fabrication work. Also, her critical advice and proofreading for this thesis helped me a lot.

I would like to thank Dr. Kai Huang for his help with my paper preparation and PL measurements. His clear logistic thinking also helped with my research project. Furthermore, I would like to thank Dr. Yuefei Cai for his loving inspiration for my whole project. And thank Dr. Sheng Jiang for his kind help on my first conference presentation.

I would like to express my special thanks to Dr. Xiang Yu and Dr. Shuoheng Shen. They are two important instructors at the initial stage of my research project on silicon and we worked closely during the past few years. Their earnest working manner and pragmatic view helped me get through many obstacles. My appreciations also go to Dr. Yipin Gong and Dr. Zhi Li for their help on MOCVD training. I would like to thank Dr. Rick Smith for his needed help and valuable suggestions for the e-beam system.

My thanks go to Professor Robert Martin and Dr. Jochen Bruckbauer from the University of Strathclyde for their support of CL measurement and precious comments on my paper.

I also acknowledge my deep sense of gratitude to the group members of Centre for GaN Materials and Devices: Dr. Nicolas Poyiatzis, Dr. Suneal Ghataora, Dr. Zohaib Ahmed Sye, Dr. Ling Jiu, Mr. Chenqi Zhu, Mr. Peter Fletcher, Mr. Peng Feng, Mr. Ye Tian, Mr. Jack Haggar, Mr. Zhiheng Lin, Mr. Volkan Esendag, Mr. Ce Xu, Mr. Guillem Martinez de Arriba and Mr. Xinchi Chen for their kind help and constructive criticism which have an immense contribution to fulfil this thesis.

I extend my gratitude to the former group members: Dr. Yaonan Hou, Dr. Yun Zhang, Dr. Benbo Xu, Dr. Kun Xing and Dr. Modestos Athanasiou for their kind support and valuable advice to this research project.

At last but not least my deep and sincere gratitude to my parents for their firm support in mentality and financing which enabled me to overcome these obstacles throughout my life in the UK. You are the only reason for everything that I have achieved. I love you all so much.

Any omissions in this acknowledgements do not mean lack of gratitude.

List of Publications

Journal Publications

1. **X. Zhao**, K. Huang, J. Bruckbauer, S. Shen, C. Zhu, P. Fletcher, F. Peng, Y. Cai, J. Bai, C. Trager-Cowan, R. Martin, and T. Wang, Investigation of the influence of an InGaN superlattice prelayer on the performance of semi-polar (11-22) green LEDs grown on silicon (113) substrates, *Scientific Reports*, 2020, 10(1), 1-8.

2. Y. Cai, S. Shen, **X. Zhao**, C. Zhu, J. Bai and T. Wang, Monolithic non-polar (11-20) GaN metal-semiconductor-metal photo-detectors with superior performance on silicon, *ACS Appl. Mater. Interfaces*, 2020, 12(22), 25031-25036.

3. S. Jiang, Y. Cai, P. Feng, S. Shen, **X. Zhao**, P. Fletcher, V. Esendag, K. Lee, and T. Wang, Explore an approach towards the intrinsic limits of GaN electronics, *ACS Appl. Mater. Interfaces,* 2020, 12(11), 12949-12954.

4. J. Bai , Y. Cai, P. Feng, P. Fletcher, **X. Zhao**, C. Zhu, and T. Wang, A direct epitaxial approach to achieving ultra-small and ultra-bright InGaN micro light emitting diodes (μLEDs), *ACS Photonics,* 2020, 7, 411-415.

5. B. Jochen, C. Trager-Cowan, B. Hourahine, A. Winkelmann, P. Vennegues, A. Ipsen, X. Yu, **X. Zhao**, X. Wallace, M. Edwards, N. Kumar, G. Hocker, B. Sebastian, M. Raphael B. Jie, T. Klaus, T. Wang and R. Martin, Luminescence behaviour of semi-polar (10-11) InGaN/GaN 'bow-tie' structures on patterned Si substrates, *Journal of Applied Physics*, 2019, 127, 035705.

6. S. Shen, **X. Zhao**, X. Yu, C. Zhu, J. Bai, T. Wang, Semi-Polar InGaN-Based Green Light-Emitting Diodes Grown on Silicon, *Phys. Status Solidi A*, 2019, 217(7), 1900654.

7. Y. Cai, X. Yu, S. Shen, **X. Zhao**, L. Jiu, C. Zhu, J. Bai and T. Wang, Overgrowth and characterization of (11-22) semi-polar GaN on (113) silicon with a two-step method, *Semiconductor Science and Technology*, 2019, 34(4), 045012.

Conference Contributions

1. **X. Zhao**, K. Huang, J. Bruckbauer, S. Shen, C. Zhu, P. Fletcher, F. Peng, Y. Cai, J. Bai, C. Trager-Cowan, R. Martin, and T. Wang, "Semi-polar InGaN-based green LEDs with super-lattice on patterned silicon", Presented at UK Nitrides Consortium, Cardiff, UK, 8th-9th January 2020

2. Y. Cai, S Shen, **X. Zhao**, C. Zhu, J. Bai, and T. Wang, "Superior performance metal-semiconductor-metal photodiode on non-polar (11-20) GaN with patterned (110) silicon", Presented at UK Nitrides Consortium, Cardiff, UK, 8th-9th January 2020

3. S. Jiang, Y. Cai, P. Feng, S. Shen, **X. Zhao**, P. Fletcher, V. Esendag, K. Lee, and T. Wang, "A new method to achieve GaN power electronics approaching its intrinsic limits", Presented at UK Nitrides Consortium, Cardiff, UK, 8th-9th January 2020

4. X. Yu, S. Shen, **X. Zhao**, C. Zhu, P. Fletcher, Y. Cai, J. Bai, and T. Wang, "Development of semi-polar (11-22) GaN for green emitters on Si substrates", Presented at UK Nitrides Consortium, Glasgow, UK, 9th-10th January 2019

5. Y. Cai, S. Shen, X. Yu, **X. Zhao**, L. Jiu, C. Zhu, J. Bai, and T. Wang, "A twostep method of growing (11-22) semi-polar GaN on (113) silicon", Presented at the Semiconductor and Integrated Opto-Electronics, Cardiff, UK, 16th-18th April 2019.

6. S. Shen, X. Yu, C. Zhu, **X. Zhao**, S. Wu, R Smith and T. Wang "Non-polar (11-20) GaN grown on patterned (110) silicon substrates" International Workshop on UV Materials and Devices (IWUMD), Kunming, China (2018).

Contents

List of Figures

List of Tables

List of Acronyms

AlN aluminium nitride

BSE backscattered electrons

Cp_2Mg biscyclopentadienyl magnesium

CO_2 carbon dioxide

CVD chemical vapor deposition

CCS close-coupled showerhead

CLFs compact fluorescent lamps

CCD charge-coupled device

CuO copper oxides

DUV deep ultraviolet

DOE department of energy

DIC differential interference contrast

DH double heterostructure

EBPVD e-Beam physical vapor deposition

EL electroluminescence

EBL electron blocking layer

EBL electron-beam lithography

EDX energy dispersive x-ray

ELOG epitaxial lateral overgrowth

EQE external quantum efficiency

FEG field emission gun

FWHM full width at half maximum

GaAs gallium arsenide

GaCI gallium monochloride

GaP gallium phosphide

Ge germanium

HMDS hexamethyldisilazane

HEMTs high electron mobility transistors

HR-XRD high-resolution x-ray diffraction

InAs indium arsenide

IRF instrument response function

IQE internal quantum efficiency

IPA isopropyl alcohol

LDs laser diodes

LEDs light-emitting diodes

LPE liquid phase epitaxy

LEEBI low energy electron beam irradiation

Mg magnesium

MFCs mass flow controllers

MOCVD metal organic chemical vapour deposition

MOVPE metal organic vapour phase epitaxy

MOVPE metal organic vapour phase epitaxy

MIS metal-insulator-semiconductor

MD misfit dislocation

MBE molecular beam epitaxy

MQW multiple quantum well

NBA n-butyl acetate

NH$_3$ ammonia

NBE near band edge

N$_2$ nitrogen

NIC nomarski interference contrast

NRCs non-radiative recombination centres

OMCVD organometallic chemical vapour deposition

OMVPE organometallic vapour phase epitaxy

PL photoluminescence

PMT photomultiplier tube

PVD physical vapor deposition

PVT physical vapour transport

PECVD plasma enhanced chemical vapour deposition

PSU power supply unit

PC pressure controller

PSF prismatic stacking fault

QB quantum barrier

QCSE quantum-confined stark effect

QCM quartz crystal microbalance

RF radio frequency

RGB red, green and blue

SEM scanning electron microscope

SEM-CL scanning electron microscope-cathodoluminescence

SE secondary electrons

SAG selective area growth

Si silicon

Si_2H_6 disilane

SiC carborundum

SSL Solid-State Lighting

SRH shockley-read-hall

SF stacking fault

SCC standard cubic centimetres

SLs superlattices

TCSPC time correlated single photon counting system card

THAH tetramethylammonium hydroxide

TDs threading dislocations

TR-PL time-resolved photoluminescence spectroscopy

TMAl trimethylaluminum

TMGa trimethylgallium

TMIn trimethylindium

UV ultraviolet

VPE vapour-phase epitaxial

VLC visible light communication

Wz wurtzite

XRD x-ray diffraction

Zn zinc

ZB zincblende

Chapter 1

Introduction

This chapter presents a brief introduction to the history of III-nitride materials and devices. The challenges faced in III-nitride research are also summarized. In particular, the motivation and aim of this project are summarized and the general background are outlined. Finally, the thesis organization is discussed at the end of this chapter.

1.1 Emergence of Solid-State-Lighting (SSL)

Lighting is an indicator of human civilization and it started from the first use of fire as lighting by early human beings from 125,000 BC. The evolution of lighting in human history begins with burning wood and animal fat. Later on, the oil lamp and candle indicate the control of the light. Afterwards the emergence of first electrical light in 19th century is regarded as a symbol of modern human history [1]. Nowadays, almost 20% of worldwide total electricity consumption is used for lighting applications [2]. And with the development of human society, the total lighting electricity consumption will increase by around 15% annually [3]. Although the portion of lighting related greenhouse gas emission only accounts for about 5% [4], the conventional lighting is heavily criticized for its inefficiency, such as incandescent light bulb and compact fluorescent lamps (CLFs), the average conversion rate from electricity to light is only 5% and 20%, respectively, which is far from satisfaction [5]. Therefore, there is a great demand to develop energy-saving lighting due to the emergence of energy crisis and the concern of global-warming. The solid-state lighting (SSL) revolution embodies a profound exploration in energy savings. Specifically, by using light-emitting diodes (LEDs) as lighting sources, more than 50% of lighting-related green-house gases can be curtailed [6]. And according to Figure 1.1 from the department of energy (DOE) in the United States, about 40% energy savings can be achieved from lighting-related power consumption by 2030 if they meet the DOE goal scenario. Furthermore, at least 10% of fuel consumption and carbon dioxide (CO_2) emission from power stations can be reduced by LED lighting in the next decade [7].

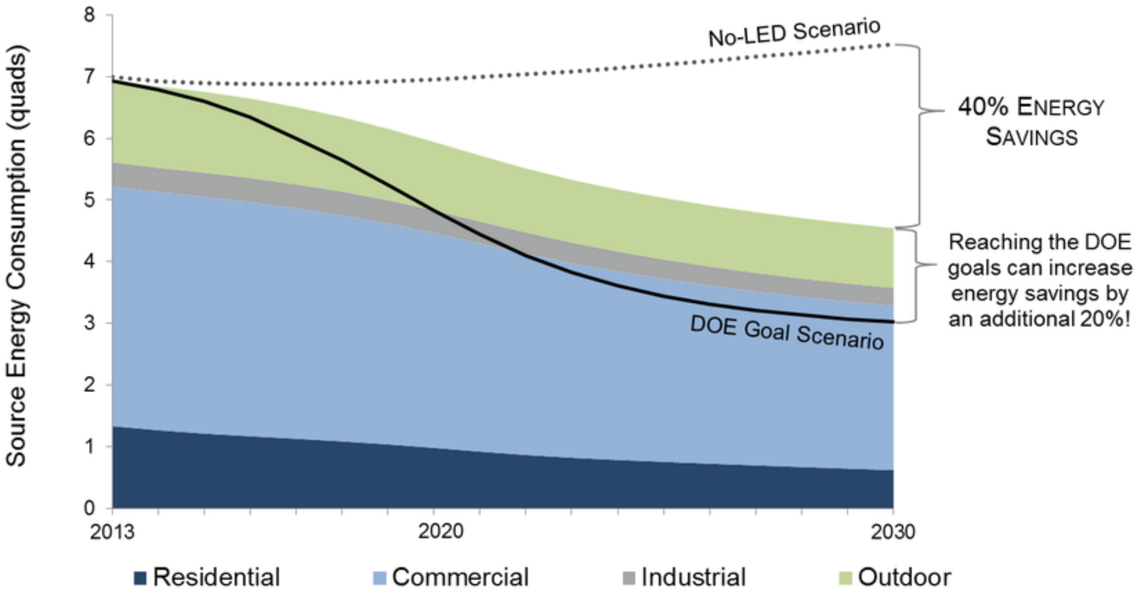

Figure 1.1: Energy consumption distribution on different purposes [7].

Within this scenario, global warming can be significantly improved by highly efficient SSL. Therefore, many countries have already started to replace conventional lighting with more energy-saving ones by implementing bans on the conventional lighting ways. For instance, incandescent bulbs were being phased out of production and sale in European Union in 2009 and completely withdraw from the market in 2012. Possible alternatives would be the fluorescent lamps and SSL due to the high luminous efficacy. For commercial fluorescent lamps, the higher cost-performance ratio can be the main advantage in the illumination market. However, limited colour performance restricts utilisation and toxic mercury content poses environmental hazards during the disposal. Therefore, Japan also announced fluorescent lamps to be banned from manufacture and import in 2020. With support from the government, SSL starts to increase the occupation of the illumination market. However, less than 20% of market occupancy in current lighting installations is owned by SSL products even though LEDs have already been commercialized for manufacturing [8]. The main concerns of LEDs are the cost-effectiveness and luminous efficiency, which still need to be further improved. For commercial LEDs, the average efficacy is 90 lm/W which is far below from the best record of 303 lm/W in the laboratory [9]. And the market price of LEDs is normally higher than other conventional lighting products. Additionally, the lifetime of LEDs cannot achieve the requirement due to patchy product quality which normally comes to lack of appropriate thermal management, leading to premature failure. As a result, there is still much need to overcome the reliability and compatibility. Apart from energy saving in general illumination, the application of LEDs can expand to other utilization in terms of horticultural grow lighting, livestock housing lighting, light therapy for human health [10] and Li-Fi communication[11]. Therefore, it is necessary to further improve the performance of LEDs due to increasing demand in these areas.

1.2 History of LEDs and materials for LEDs

1.2.1 History of LEDs

Electroluminescence is a well-known phenomenon in electroluminescent materials and described as the light emission in response to the application of a strong electric field or the conveyance of an electrical current. After the first report of yellow electroluminescence from carborundum (SiC, also known as silicon carbide) by an English electrical engineer Henry Joseph Round in 1907 [12]. And in the following decades, rectifying effects were observed from silicon (Si), carborundum (SiC), germanium (Ge), and copper oxides (CuO) by contacting a sharp metal point to the material's surface [13]. In 1927, Oleg Lossev reexamined electroluminescence on SiC with forward and reverse-biased point-contact diodes and published this phenomenon in detail [14]. Based on this work, Georges Destriau first proposed the term of electroluminescence when he observed the emission of visible light from zinc sulfide in 1936 [15]. In early 1940, the semiconductor properties were further understood with the development of quantum physics, Russell Ohl ascertained p-type and n-type properties of Si and William Shockley published a paper regarding the theory of p-n junctions in 1949, providing an explanation for the light emission effect in p-n junctions and conceived of as the initial stage of p-n junction LEDs [16].

In fall 1961, the first practical infrared LED was demonstrated by James R. Biard [17]. In the next year, the first visible-light (red) LED was invented by Nick Holonyak Jr who was employed by General Electric [18]. In 1968, the first commercial LED products came out in six years' material science investigation program were launched by HP [19] Initially, these applications of visible-light LEDs were only within the range of signal indicator and sevensegment displays due to its low brightness and extremely high cost [20]. Until the 1970s, a critical step had been taken that Fairchild Optoelectronics began to produce low-cost LEDs by developing a planar process for semiconductor chip fabrication and packaging method. As a result, the LED started to evolve into other applications rather than staying in laboratory test equipment and the spectrum range extended from crimson (650 nm) to olivine(570 nm) after utilizing of GaAs/GaP materials [21]. With continuous and intensive research work into LED technology, ultra-bright red and amber LEDs were achieved on AlInGaP by HP in the early 1990s [22]. In 1994, Shuji Nakamura of Nichia Corporation developed high-brightness InGaN/GaN based blue and green LEDs [23], [24] and awarded the Nobel Prize in Physics with Isamu Akasaki and Hiroshi Amano in 2014. These ultra-bright blue LEDs quickly lead to the development of white LEDs as scientists discovered that coating fluorescent phosphors on the blue LED chip could generate white light. And the first reported white light LED was achieved in 1995 [25]. In addition, from 1980 to 1990, the emergence of OLED allows another major area of SSL application [2].

1.2.2 Materials for LEDs

In 1947, J. Bardeen, W. Brattain and W. Shockley provided a scientific step forward in semiconductor physics and revolutionized the field of electronics by developing transistors [5]. Afterwards, extensive research began in the field of semiconductor materials. The early research was mainly focused on silicon (Si), germanium (Ge) and II-VI materials since they are natural existence. In the early stage of LEDs, the spectra were limited in the infrared range from the materials of gallium arsenide (GaAs) and indium arsenide (InAs) with direct bandgap. Due to an indirect bandgap, gallium phosphide (GaP) with the visible spectrum has an extremely low efficiency [13]. Until the early 1960s, Herbert Nelson from RCA Laboratories invented liquid phase epitaxy (LPE), enabled the demonstration of the high-quality heterojunction materials. Later on, amber and yellow-green GaAsP LEDs were manufactured as a result of high-quality epitaxial growth of LPE [13]. Furthermore, different ternary alloys such as AlGaAs, GaAsP, InAlAs, InGaAs, AlAsP, InGaP were also explored for optoelectronic devices [26]–[29]. However, LPE has limited control of layer thickness which obstacles further improvement of quantum efficiency. In the 1970s, LPE was supplanted by metal organic vapour phase epitaxy (MOVPE) and molecular beam epitaxy (MBE) for their precise control on layer thickness. Additionally, MOVPE can achieve high-temperature growth condition up to 1200 ºC, thus it has been widely used in epitaxial growth of Al-containing materials. Mass production of yellow and red InAlGaP LEDs with MOVPE production technologies began at the early 1990s [13]. Till now, InAlGaP-based yellow and red LEDs are still in commercial mass production. On the other side, heteroepitaxial GaN growth on sapphire was started by Jacques Pankove and his colleagues at RCA Labs by vapour-phase epitaxial (VPE) method in the early 1970's [30]. Since then, GaN has become a potential material for LED devices. And during the period of 1990's, Akasaki and his colleagues at Nagoya University achieved the first GaN p-n junction by using magnesium (Mg) dopant for p-GaN [31]. Later on, Shuji Nakamura, from Nichia Corporation, demonstrated the first high brightness GaN blue LEDs with InGaN/GaN heterostructure [23].

1.3 Development of Nitride-based LEDs

To date, enormous progress has been achieved in III-nitride based optoelectronics and electronics devices. As shown in Figure 1.2, III-nitride materials such as AlN, GaN, InN, and their ternary alloys exhibit direct bandgaps vary from 0.7 eV (InN) to 6.2 eV (AlN) at room temperature. Thus, the entire spectrum can be covered from ultraviolet to infrared by changing their alloy composition which is impossible for the other III-V materials such as GaAs/GaP. Besides, III-nitride semiconductor materials present a high stability in physical, chemical and thermal properties which are attractive for optoelectrical applications in the harsh environment. In addition, high breakdown voltage and high carrier drift saturation velocities of III-nitride materials enable it to be a very promising candidate of high power and high breakdown field devices.

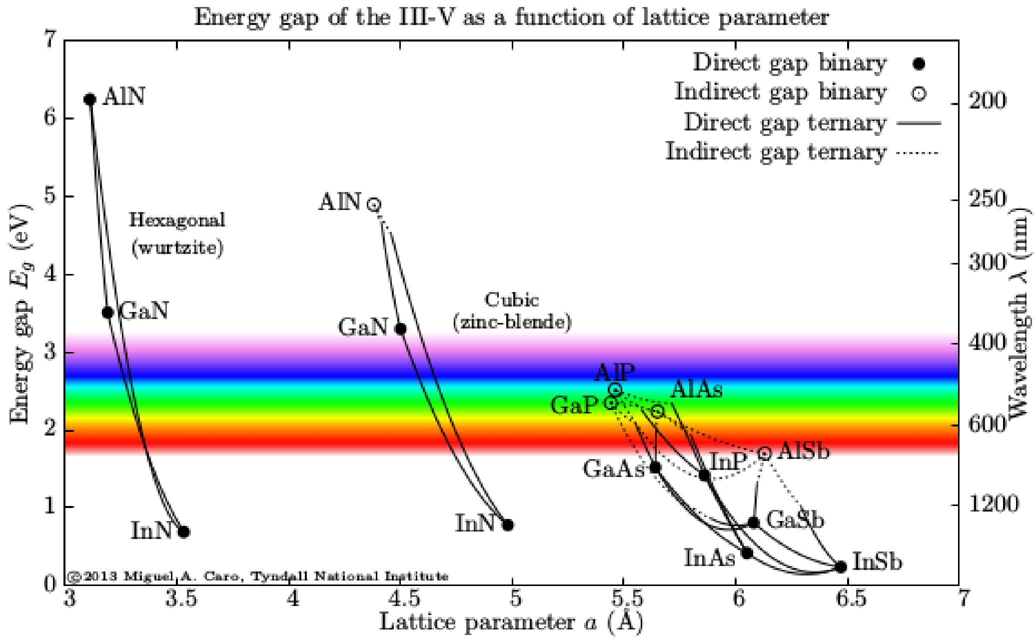

Figure 1.2: The bandgap energies and corresponding spectra wavelength of different III-nitrides and their alloys at room temperature [32].

GaN is non-natural existed material and was firstly synthesized by Johnson et al. in the reaction of metallic gallium with ammonia gas at high temperature as GaN powder in 1928 [33]. Later on, Juza et al. studied the structural properties of GaN material such as lattice constant and molecular structure [34]. In 1969, H.P Maruska and J.J. Tietjen performed the growth of single-crystalline GaN films on sapphire substrate by flowing ammonia gas to the gallium chloride (GaCI) at high temperature [35]. However, the GaN films are inherently n-type doped which may be attributed to nitrogen vacancies or impurities from the chamber material such as quartz, or reactor leaks [36]. Zinc (Zn) and magnesium (Mg) were first used as acceptor dopant for GaN. However, p-type GaN only exhibited insulating or semi-insulating properties even under heavy doping concentration. Therefore, Pankove et. al. demonstrated the first GaN-based LEDs by using a metal-insulator-semiconductor (MIS) structure to emit 475nm blue light in 1971 [37]. During that period, even though many investigations and improvements were accomplished in the area of GaN-based devices, the unavailability of p-type GaN and lack of high-quality GaN films still led to the temporary abandonment of gallium nitride as a material for blue LEDs. Until 1989, Amano et al. demonstrated the first conductive Mg-doped p-type GaN by using low energy electron beam irradiation (LEEBI) treatment [31]. It was found that the resistivity of the as-grown sample dramatically decreased from ~10^8 $\Omega \cdot \mathrm{cm}$ to ~35 $\Omega \cdot \mathrm{cm}$. However, the thickness of LEEBI treated GaN was estimated to be only around 500 nm of penetration depth by considering the energy of the incident electrons. In 1992, Nakamura et al. performed a further optimized method of thermal annealing Mg-doped GaN under nitrogen (N_2) ambient in the MOCVD, achieving p-type GaN by breaking the Mg-H complex to obtain free holes. [38].

Apart from the issue of achieving p-type GaN, the high density of dislocation of GaN films, which resulted from the large lattice mismatch between GaN thin fim and sapphire substrate, also impeded the development of GaN-based devices. Until 1983, Yoshida et. al. achieved high crystal quality of GaN films by applying a two-step growth, namely, inserted aluminium nitride (AlN) layer prior to the growth of GaN by using Molecular Beam Epitaxy (MBE) [39]. Thus, the AlN films have lattice matching and small thermal expansion coefficients with GaN, leading to the improvement of GaN crystal quality. In 1986, a low-temperature AlN buffer layer was applied by Amano to the two-step growth of GaN, leading to a GaN film with smooth morphology by using metal organic chemical vapour deposition (MOCVD) [40]. In 1991, Nakamura applied further optimization to achieve defect annihilation by inserting low-temperature GaN buffer and annealing at high temperature to obtain superior GaN thin firm. The ternary InGaN-is one candidate for blue emission as its bandgap covered from 1.9 to 3.4 eV by altering indium composition. In 1993, the first blue (440 nm) [41] and violet (varies from 411 nm to 420 nm) [42] LED with p-GaN/n-InGaN/n-GaN double heterostructure (DH) was performed by Nakamura et al.. The external quantum efficiency (EQE) was 0.22% and 0.15% respectively at a 20 mA injection current. In the next year, their group further enhanced the performance of blue LEDs by using Zn-doped InGaN/Si-doped AlGaN DH and inserting an AlGaN layer which works as an electron blocking layer (EBL) [43]. The luminous intensity was increased over 1 cd and the EQE was 2.7% at a 20 mA injection current. Their work also led to achieving of first InGaN-based green and yellow LED by introducing InGaN/GaN multiple quantum well (MQW) structures [44]. In 1995, the first white LED was integrated InGaN-based blue LED with yellow phosphor [25]. And until nowadays, it is still the main commercial way to fabricate white LEDs.

1.4 III-Nitrides Challenges

Tremendous research and development in III-nitrides have been made in the last two decades, leading to abundant III-nitrides based optoelectronic devices. However, the majority achievements are still limited to conventional c-plane III-nitrides, in particular blue LEDs grown sapphire substrate. There still exist a number of issues and challenges which need to be overcome, such as quantum-confined Stark effects (QCSE), efficiency droop, etc. The details of main issues are discussed in this section.

1.4.1 Quantum-Confined Stark Effect (QCSE)

In order to achieve different emission wavelengths, quantum wells (QWs) are applied to provide carrier confinement into a small region and tuning the emission energy by changing the concentration ratios of components in the confinement layer. For near UV or visible light emitters, the InGaN/GaN QWs are widely used in III-nitride LEDs. As GaN is a wurtzite structure with a strong spontaneous polarization, and the present of QWs will induce piezoelectric polarization due to the lattice mismatch between InGaN quantum well (QW) and GaN quantum barrier (QB). Consequently, the large spontaneous and piezoelectric polarization will result in charge accumulation at the interfaces of heterojunction, leading to strong electric fields with a range of 1.5-3 $MVcm^{-1}$ [45]. The relationship between electric field and polarization follows the equation as shown below:

$$F_{qw} = \frac{P_{sp,b} - P_{sp,qw}}{\varepsilon_{e,qw}\varepsilon_o} - \frac{P_{pz,qw}}{\varepsilon_{e,qw}\varepsilon_o} \tag{1.1}$$

Where the $P_{sp,qw}$ *and* $P_{sp,b}$ are the spontaneous polarisation of quantum well and barrier respectively, $\varepsilon_{e,qw}$ is the relative dielectric permittivity of the QW material.

However, this equation only shows validity on a QW structure with unstrained QBs. For InGaN/GaN QWs structure with compressive strain in quantum wells, extra piezoelectric polarisation will be induced from the system. As a result, the polarisation generates an electric field, leading to an inclination of energy bandgap in the QW structure. Accordingly, as shown in Figure 1.3, spontaneous polarisation (P_{sp}) along [0001] direction will appear in the conventional polar Ga-face material system due to no-centrosymmetric and no-inversion symmetric of wurtzite hexagonal III-nitride materials [46], [47]. III-nitride materials have large piezoelectric coefficients d_{33}, such as GaN is 2.13 pm/V [48], [49]. Thus, due to the compressive strain in InGaN QW material, a piezoelectric polarisation (P_{pz}) charges with opposite direction to P_{sp} appears at the interface between QW and QB [50]. And the resultant polarisation is normally dominated by P_{pz} as the large lattice mismatch (up to ~11%) between InN and GaN materials , leading to a induced internal polarisation filed (F_{pol}) is directed from top interface to the bottom interface [50], [51]. Consequently, electrons in InGaN QW are accumulated on the left bottom side of the conduction band. In the meanwhile, holes are distributed on the right top side of the valence band. The overlap of electron-hole wavefunctions is decreased by the spatial separation of carriers, leading to a lower probability of carrier recombination. In addition, the transition energy is reduced as the internal electric fields band bends the bandgap structure. As a result, a significant reduction of internal quantum efficiency (IQE) occurs on III-nitride LEDs with longer emission wavelength. This phenomenon is referred as quantum confined stark effect (QCSE). In addition, the strain increases with higher indium composition, thus inducing stronger piezoelectric field. And with the increasing injection current, the sheet changes at interfaces are screened by injected carriers, flattens the QW bandgap profile, leading to a blue shift at the emission wavelength [52], [53]. These limits the efficiency improvement of InGaN based LEDs especially in long wavelength range.

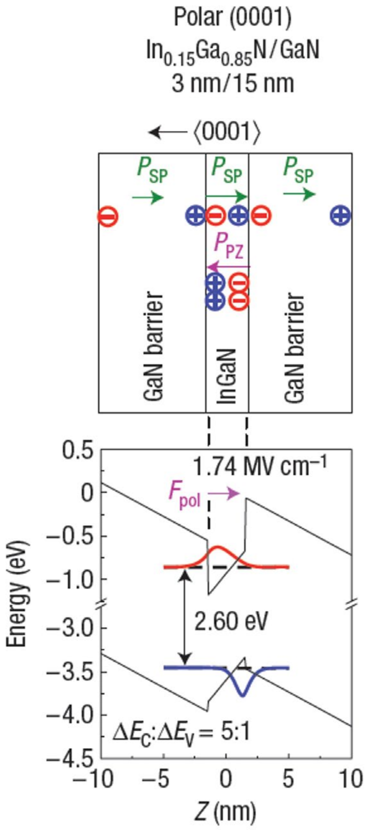

Figure 1.3: schematic of the polarizations and the bandgap structure of strained $In_{0.15}GaN_{0.85}N/GaN$ *quantum wells* [54].

1.4.2 Efficiency Droop

In order to measure the performance of photonic devices, internal quantum efficiency (IQE) and external quantum efficiency (EQE) are introduced to assess the efficacy of the device. IQE is defined as the faction of absorbed photos in the device to the collected carriers. Temperature-dependent photoluminescence (TD-PL) is a typical approach to estimate the IQE by calculate the ratio of room-temperature (RT) to low-temperature (LT) PL intensity as the PL intensity could reach saturation in virtun of the freeze out effect of defect-recombination under low temperature and only radiative recombination occurs due to the lower activation energy [55]. The EQE is defined as the fraction of incident photons which emitted from the device to the injected carriers passing through. Integration sphere is the typical kit to measure this parameter.

Another widely observed phenomenon in III-nitride LEDs is “efficiency droop”. Specifically speaking, as shown in Figure 1.4, the efficiency of LEDs typically reaches to a peak at low current densities (normally at 5-10 A/cm^2, depending on the wavelength of emission), and then, with further increasing injection current, a gradual degradation occurs in the LED efficiency. The fundamental mechanisms of the efficiency droop are still controversial. However, several possible mechanisms have been proposed, such as Auger recombination [56], electron overflow [57], carrier delocalization [58], density activated defect recombination [59] etc.

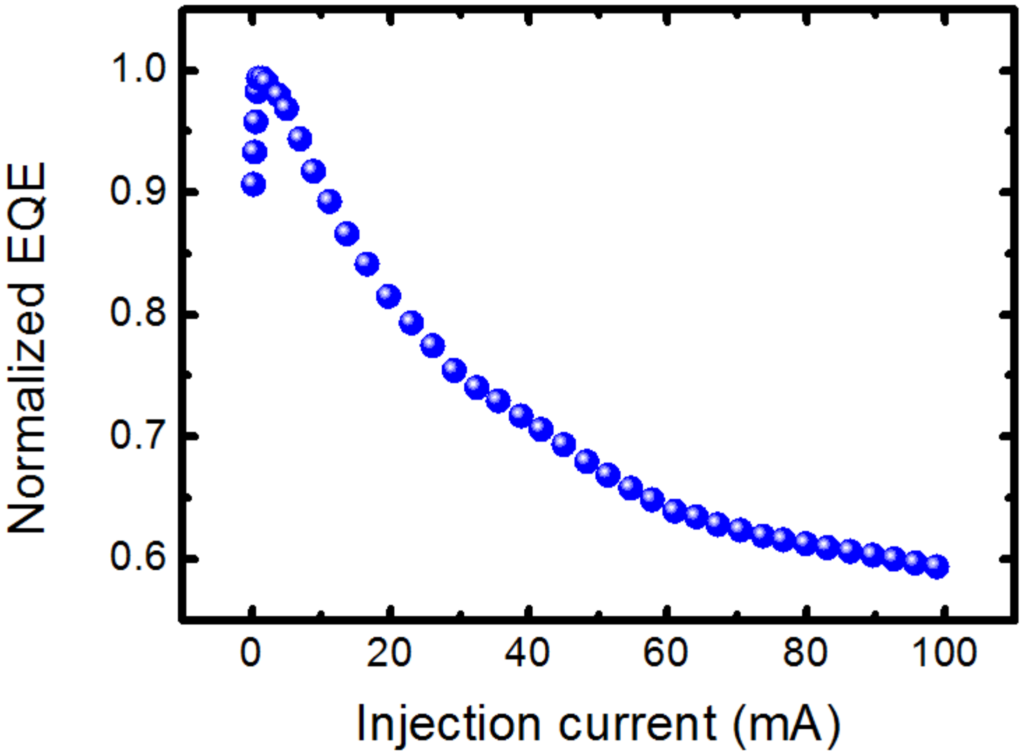

Figure 1.4: A typical normalized external quantum efficiency (EQE) of LED as a function of injection current.

The Auger recombination is a non-radiative recombination process which generates thermal energy instead of emitting photons, leading to a reduction in LED efficiency. More details regard to Auger recombination will be introduced in next chapter. The electron overflow is defined as electrons escaping from the active region under the electric field without any occurrence of the radiative recombination process. With further increase of injection current, more electrons are able to escape from the active region, resulting in reduced efficiency of optical devices. The carrier delocalization is an opposite process of carrier localization which increases the mobility of localised carrier under a high temperature or high carrier density. As a result, the carriers have more probability to roam to defect area and serve as non-radiative recombination centres, thus reducing the efficiency of LEDs. Despite extensive research has been conducted on these subjects, the real mechanism of efficiency droop still has not been clarified.

1.4.3 Green Gap

The efficiency droop raised another serious issue, the green gap. To be specific, InGaN based LEDs suffer more severe efficiency droop when it comes to longer emission wavelengths. As shown in Figure 1.5, Nichia corporation has achieved a high-performance InGaN-based blue LED with an IQE of 86.9% under 50 mA injection current [60]. However, based on a very recent report from UCSB, the performance of green LEDs is only 30% EQE at 20 A/cm^2 current density with 527nm emission wavelength [61]. For III-phosphides system, the AlInGaP based red LEDs have achieved >70% EQE [9], and the efficiency decreases dramatically with shorter wavelength. Thus, the green spectrum region suffers the lowest quantum efficiency, and this is so-called “green gap” [62].

The highest EQE of InGaN based greed LEDs were reported by Q. Lv at 2019 with sandwich-like MQW structure in which composed of slightly larger bandgap QW and slightly smaller bandgap near p-GaN. The carrier interaction between wells and concomitant is improved with uniform carrier distribution in active region, leading to a highest peak EQE of 56.2% was achieved on GaN-on-silicon template [63].

To date, the most commercial way to achieve white light LEDs is still through integrating a blue LED with down-conversion yellow phosphor. The overall efficacy of such kind of LED is limited by down-conversion energy loss and the emission exhibits a low colour rendering. To overcome these drawbacks, a combination of red, green and blue (RGB) emission from high efficacy LEDs is a promising way. Therefore, it is necessary to resolve the obstacle of the green gap, achieving high-efficiency RGB white LEDs.

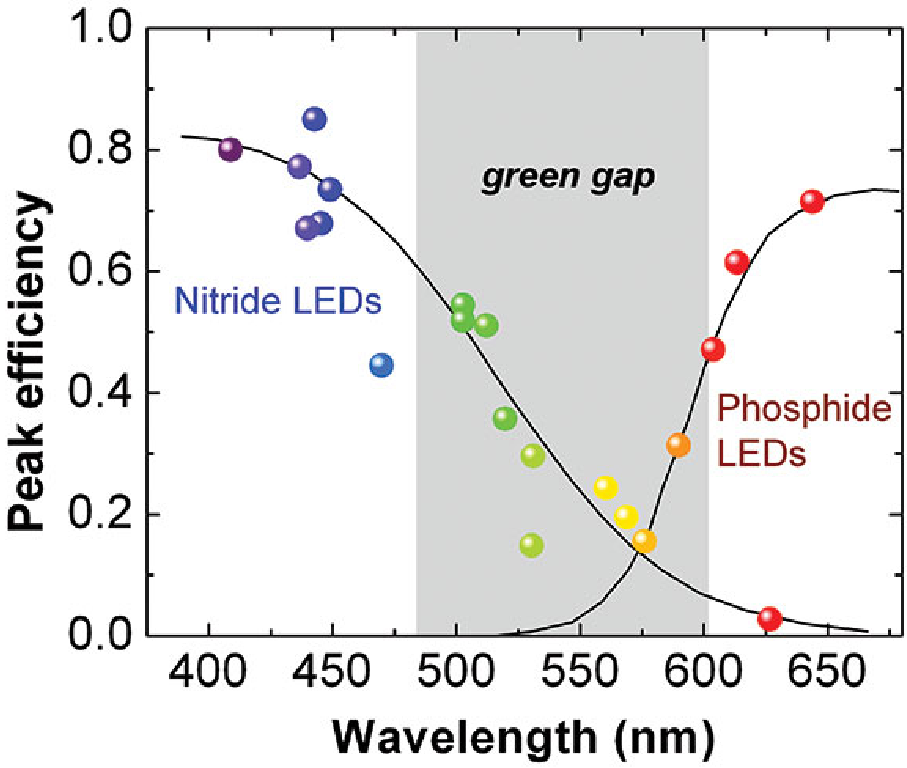

Figure 1.5: External quantum efficiency of LEDs as a function of the wavelength of emission [62].

1.4.4 Epitaxial Substrates

In order to achieve growth of GaN on different substrates, homoepitaxial growth and heteroepitaxial growth would be two available options. Homoepitaxial growth on bulk GaN substrates is ideal, but the unaffordable cost of substrates (up to $800) and limited size (typical 1×1 cm^2) impede the massive production of industrial manufacture. As a result, extensive research of heteroepitaxial growth of III-nitrides on foreign substrates is carried out. The most promising candidates such as silicon carbide (SiC), sapphire and silicon (Si) are widely adopted in III-nitrides research and commercial manufacturing to date. However, due to the large lattice mismatch, the growth of GaN on foreign substrates normally observed a high density of dislocations. These defects will act as non-radiative recombination centres [59] and limit transport properties of carriers [64], leading to degradation of the optical performance.

SiC substrates have the smallest (3.5%) lattice mismatch and the highest thermal conductivity (4.9 W/cmK) among the foreign substrates [65]. Therefore, the GaN grown on SiC substrate exhibits a lower dislocation density and suitable for high-power electronic applications [66].

However, SiC substrate shares the same drawbacks with bulk GaN substrates which cannot be produced by conventional crystal pulling. The commercial SiC substrate is normally grown by physical vapour transport (PVT), thus, expensive price and limited length of grown boule make it less attractive to be an industry-compatible substrate [65].

Sapphire is the most used substrate for III-nitride growth which benefits from its hexagonal symmetry, highly stable chemical properties and close matching of thermal expansion coefficient. However, GaN and sapphire still suffer a large lattice mismatch of 16% [67]. Such a large lattice mismatch will result in high dislocation density in subsequent GaN growth. In order to improve the crystal quality of GaN, complicated methods such as epitaxial lateral overgrowth (ELOG) are introduced in the subsequent GaN growth which further increases the cost of manufacture.

Since the last half-century, silicon, as the first generation of semiconductor material, revolutionized the semiconductor industry. Therefore, the silicon technology is mature and well developed compared with other semiconductor materials. Currently, the availability of large size commercial silicon can be up to 8-inch. However, the lattice mismatch between GaN and silicon is 17% which is the largest one during the commercially available substrates [68]. And the thermal expansion coefficient mismatch between silicon and GaN is as large as 46% [68] and produces tensile strain, leading to seriously wafer bowing and epilayer cracking during the cooling-down process. In addition, the Ga droplet can strongly react with silicon during high-temperature growth and form a eutectic alloy [69], leading to a damaged morphology of epilayers and substrate. Despite these changeling, silicon substrate could offer several advantages through combining existing mature silicon technologies such as chemical etching with integrated semiconductor circuits to be an inexpensive alternative to sapphire substrates.

1.5 Motivation and Aim

III-nitride semiconductor materials have exhibited excellent properties in terms of large bandgap and high stability in both chemical and physical properties, showing great potential for optoelectronic devices such as LEDs, high electron mobility transistors (HEMTs) [70] and photodetectors. In particular, III-nitride materials on silicon substrates have attracted extensive attention recently as a result of very mature silicon technology [71], low costs, high integration level and scalability. However, III-nitrides on silicon substrates still encounter many challenges as mentioned above especially for the semi-polar GaN growth on silicon substrates which will be introduced in the next chapter.

Conventional c-plane GaN-based devices intrinsically flaws with QCSE which is caused by the piezoelectric fields across the active region of heterostructures. In order to solve this issue, semi-polar (11-22) GaN can be one of the promising approaches to significantly reduce the QCSE to further improve the performance of corresponding devices [51], [72], [73]. In addition, semi-polar (11-22) GaN is reported to exhibit high indium incorporation as the surface atomic configuration with lower chemical potential [74]–[76] which is critical for achieving long wavelength emitters.

This thesis firstly presents a two-step growth of semi-polar (11-22) GaN on (113) silicon substrates with a low density of dislocations and no melt-back etching, which gives insight to subsequent AlGaN structure required for high-temperature growth. And then, green LEDs with excellent performance are achieved on high crystal quality (11-22) GaN buffer with one-step growth method. Specially designed silicon stripe pattern and initial growth with high temperature to perform a better selective area growth, demonstrating a potential approach to manufacturing long-wavelength emitter on the silicon substrate. Finally, an investigation is carried out on the effect of an InGaN superlattices prelayer inserted prior to the active region on the performance on semi-polar (11-22) InGaN LEDs.

1.6 Thesis Organization

This thesis consists of seven chapters as follows:

Chapter 1 briefly introduces the history and development of III-nitride based LEDs, then followed by current challenges in improving performance and achieving longer emission wavelength. The motivation and aim are presented at the end.

Chapter 2 describes the background of semiconductors in terms of physical and electrical properties. A detailed background of semi-polar and non-polar III-nitrides on silicon substrates is presented.

Chapter 3 provides the detailed configuration of employed fabrication or characterization equipment and epitaxial facility (MOCVD).

Chapter 4 introduces a two-step approach for the growth of semi-polar (11-22) GaN on patterned (113) silicon substrate.

Chapter 5 demonstrates an InGaN/GaN based green LEDs on high-quality (11-22) GaN buffer with improved one-step growth approach on patterned (113) silicon substrate.

Chapter 6 investigates the impact of a SLS prelayer on semi-polar (11-22) green LEDs on pattered (113) substrate.

Chapter 7 concludes the research which are presented in this thesis and gives an outlook for the future plan.

Reference

[1] D. DiLaura, “A brief history of lighting,” *Opt. Photonics News*, vol. 19, no. 9, pp. 22–28, 2008.

[2] A. Bergh, G. Craford, A. Duggal, and R. Haitz, “The promise and challenge of solid-state lighting,” *Phys. Today*, vol. 54, no. 12, pp. 42–47, 2001.

[3] US.D.of Energy, “Solid-State Lighting R&D Plan.”

[4] P. Waide and S. Tanishima, *Light's labour's lost: policies for energy-efficient lighting*. OECD Publishing, 2006.

[5] P. Waide, “Phase out of incandescent lamps: Implications for international supply and demand for regulatory compliant lamps,” 2010.

[6] E. G. Hertwich *et al.*, “Material efficiency strategies to reducing greenhouse gas emissions associated with buildings, vehicles, and electronics—a review,” *Environ. Res. Lett.*, vol. 14, no. 4, p. 43004, 2019.

[7] C. J. Humphreys, “Solid-state lighting,” *MRS Bull.*, vol. 33, no. 4, pp. 459–470, 2008.

[8] D. Feezell and S. Nakamura, “Invention, development, and status of the blue light-emitting diode, the enabler of solid-state lighting,” *Comptes Rendus Phys.*, vol. 19, no. 3, pp. 113–133, 2018.

[9] P. M. Pattison, M. Hansen, and J. Y. Tsao, “LED lighting efficacy: status and directions,” *Comptes Rendus Phys.*, vol. 19, no. 3, pp. 134–145, 2018.

[10] Z. Grajcar, “LED lighting for livestock development.” Google Patents, 11-Jul-2017.

[11] I. C. Robin *et al.*, “Complete solid state lighting (SSL) line at CEA LETI,” in *Thirteenth International Conference on Solid State Lighting*, 2014, vol. 9190, p. 91900I.

[12] H. J. Round, “A note on carborundum,” in *Semiconductor Devices: Pioneering Papers*,

World Scientific, 1991, p. 879.

[13] R. D. Dupuis and M. R. Krames, “History, development, and applications of high-brightness visible light-emitting diodes,” *J. Light. Technol.*, vol. 26, no. 9, pp. 1154–1171, 2008.

[14] O. V Lossev, “CII. Luminous carborundum detector and detection effect and oscillations with crystals,” *London, Edinburgh, Dublin Philos. Mag. J. Sci.*, vol. 6, no. 39, pp. 1024–1044, 1928.

[15] G. Destriau, “Recherches sur les scintillations des sulfures de zinc aux rayons α,” *J. Chim. Phys.*, vol. 33, pp. 587–625, 1936.

[16] W. Shockley, “The Theory of p-n Junctions in Semiconductors and p-n Junction Transistors,” *Bell Syst. Tech. J.*, vol. 28, no. 3, pp. 435–489, 1949.

[17] T. M. Okon and J. R. Biard, “The first practical LED,” *Edison Tech Cent.*, vol. 9, 2015.

[18] N. Holonyak Jr and S. F. Bevacqua, “Coherent (visible) light emission from Ga (As1− x P x) junctions,” *Appl. Phys. Lett.*, vol. 1, no. 4, pp. 82–83, 1962.

[19] E. F. Schubert, T. Gessmann, and J. K. Kim, “Light emitting diodes,” *Kirk-Othmer Encycl. Chem. Technol.*, 2000.

[20] B. Kramer, *Advances in solid state physics*, vol. 42. Springer, 2007.

[21] R. Haitz and J. Y. Tsao, “Solid-state lighting: Why it will succeed, and why it won’t be overtaken,” *Opt. Photonik*, vol. 6, no. 2, pp. 26–30, 2011.

[22] M. G. Craford, “LEDs challenge the incandescents,” *IEEE Circuits Devices Mag.*, vol. 8, no. 5, pp. 24–29, 1992.

[23] S. Nakamura, T. Mukai, and M. Senoh, “High-power GaN pn junction blue-light-emitting diodes,” *Jpn. J. Appl. Phys.*, vol. 30, no. 12A, p. L1998, 1991.

[24] S. Nakamura, M. Senoh, N. Iwasa, S. Nagahama, T. Yamada, and T. Mukai, “Superbright green InGaN single-quantum-well-structure light-emitting diodes,” *Jpn.*

J. Appl. Phys., vol. 34, no. 10B, p. L1332, 1995.

[25] K. Bando, K. Sakano, Y. Noguchi, and Y. Shimizu, “Development of high-bright and pure-white LED lamps,” *J. Light Vis. Environ.*, vol. 22, no. 1, pp. 1_2-1_5, 1998.

[26] H. Morkoç, *Handbook of nitride semiconductors and devices, Materials Properties, Physics and Growth*, vol. 1. John Wiley & Sons, 2009.

[27] S. Nakamura and M. R. Krames, “History of gallium–nitride-based light-emitting diodes for illumination,” *Proc. IEEE*, vol. 101, no. 10, pp. 2211–2220, 2013.

[28] H. P. Maruska and W. C. Rhines, “A modern perspective on the history of semiconductor nitride blue light sources,” *Solid. State. Electron.*, vol. 111, pp. 32–41, 2015.

[29] J. Cho, J. H. Park, J. K. Kim, and E. F. Schubert, “White light-emitting diodes: History, progress, and future,” *Laser Photon. Rev.*, vol. 11, no. 2, p. 1600147, 2017.

[30] J. I. Pankove, *Optical processes in semiconductors*. Courier Corporation, 1975.

[31] H. Amano, M. Kito, K. Hiramatsu, and I. Akasaki, “P-type conduction in Mg-doped GaN treated with low-energy electron beam irradiation (LEEBI),” *Jpn. J. Appl. Phys.*, vol. 28, no. 12A, p. L2112, 1989.

[32] D. of Physics, “III-V Compound Semiconductirs,” *WARWICK*, 2020. [Online]. Available: https://warwick.ac.uk/fac/sci/physics/current/postgraduate/regs/mpagswarwick/ex5/intro/iii-v-compoundsemiconductors/. [Accessed: 22-Sep-2020].

[33] W. C. Johson, J. B. Parsons, and M. C. Crew, “Nitrogen coumponds of Gallium-III. Gallic nitride,” *J. Phys. Chem*, vol. 36, p. 2651, 1932.

[34] S. Strite and H. Morkoç, “GaN, AlN, and InN: a review,” *J. Vac. Sci. Technol. B Microelectron. Nanom. Struct. Process. Meas. Phenom.*, vol. 10, no. 4, pp. 1237–1266, 1992.

[35] H. P. Maruska and J. J. Tietjen, "The preparation and properties of vapor-deposited single-crystal-line GaN," *Appl. Phys. Lett.*, vol. 15, no. 10, pp. 327–329, 1969.

[36] C. G. Van de Walle, C. Stampfl, and J. Neugebauer, "Theory of doping and defects in III–V nitrides," *J. Cryst. Growth*, vol. 189, pp. 505–510, 1998.

[37] J. I. Pankove, E. A. Miller, and J. E. Berkeyheiser, "GaN electroluminescent diodes," in *1971 International Electron Devices Meeting*, 1971, p. 78.

[38] S. Nakamura, T. Mukai, M. Senoh, and N. Iwasa, "Thermal annealing effects on p-type Mg-doped GaN films," *Jpn. J. Appl. Phys.*, vol. 31, no. 2B, p. L139, 1992.

[39] S. Yoshida, S. Misawa, and S. Gonda, "Improvements on the electrical and luminescent properties of reactive molecular beam epitaxially grown GaN films by using AlN-coated sapphire substrates," *Appl. Phys. Lett.*, vol. 42, no. 5, pp. 427–429, 1983.

[40] H. Amano, N. Sawaki, I. Akasaki, and Y. Toyoda, "Metalorganic vapor phase epitaxial growth of a high quality GaN film using an AlN buffer layer," *Appl. Phys. Lett.*, vol. 48, no. 5, pp. 353–355, 1986.

[41] S. Nakamura, M. Senoh, and T. Mukai, "P-GaN/N-InGaN/N-GaN double-heterostructure blue-light-emitting diodes," *Jpn. J. Appl. Phys.*, vol. 32, no. 1A, p. L8, 1993.

[42] S. Nakamura, M. Senoh, and T. Mukai, "High-power InGaN/GaN double-heterostructure violet light emitting diodes," *Appl. Phys. Lett.*, vol. 62, no. 19, pp. 2390–2392, 1993.

[43] S. Nakamura, T. Mukai, and M. Senoh, "Candela-class high-brightness InGaN/AlGaN double-heterostructure blue-light-emitting diodes," *Appl. Phys. Lett.*, vol. 64, no. 13, pp. 1687–1689, 1994.

[44] S. Nakamura, M. Senoh, N. Iwasa, and S. Nagahama, "High-brightness InGaN blue, green and yellow light-emitting diodes with quantum well structures," *Jpn. J. Appl. Phys.*, vol. 34, no. 7A, p. L797, 1995.

[45] D. A. B. Miller *et al.*, “Band-edge electroabsorption in quantum well structures: The quantum-confined stark effect,” *Phys. Rev. Lett.*, vol. 53, no. 22, pp. 2173–2176, 1984, doi: 10.1103/PhysRevLett.53.2173.

[46] O. Ambacher *et al.*, “Two-dimensional electron gases induced by spontaneous and piezoelectric polarization charges in N-and Ga-face AlGaN/GaN heterostructures,” *J. Appl. Phys.*, vol. 85, no. 6, pp. 3222–3233, 1999.

[47] H. W. Jang, J.-H. Lee, and J.-L. Lee, “Characterization of band bendings on Ga-face and N-face GaN films grown by metalorganic chemical-vapor deposition,” *Appl. Phys. Lett.*, vol. 80, no. 21, pp. 3955–3957, 2002.

[48] C. M. Lueng *et al.*, “Piezoelectric coefficient of GaN measured by laser interferometry,” *J. Non. Cryst. Solids*, vol. 254, no. 1–3, pp. 123–127, 1999.

[49] S. Muensit and I. L. Guy, “The piezoelectric coefficient of gallium nitride thin films,” *Appl. Phys. Lett.*, vol. 72, no. 15, pp. 1896–1898, 1998.

[50] F. Bernardini and V. Fiorentini, “Macroscopic polarization and band offsets at nitride heterojunctions,” *Phys. Rev. B*, vol. 57, no. 16, p. R9427, 1998.

[51] T. Takeuchi *et al.*, “Quantum-Confined Stark Effect due to Piezoelectric Fields in GaInN Strained Quantum Wells,” *Jpn. J. Appl. Phys.*, vol. 36, no. Part 2, No. 4A, pp. L382–L385, 1997, doi: 10.1143/jjap.36.l382.

[52] D. C. Reynolds, D. C. Look, and B. Jogai, “Combined effects of screening and band gap renormalization on the energy of optical transitions in ZnO and GaN,” *J. Appl. Phys.*, vol. 88, no. 10, pp. 5760–5763, 2000.

[53] E. Kuokstis, J. W. Yang, G. Simin, M. A. Khan, R. Gaska, and M. S. Shur, “Two mechanisms of blueshift of edge emission in InGaN-based epilayers and multiple quantum wells,” *Appl. Phys. Lett.*, vol. 80, no. 6, pp. 977–979, 2002.

[54] S. F. Chichibu *et al.*, “Origin of defect-insensitive emission probability in In-containing (Al, In, Ga) N alloy semiconductors,” *Nat. Mater.*, vol. 5, no. 10, pp. 810–816, 2006.

[55] X. Ji *et al.*, “Investigation into low-temperature photoluminescence internal quantum efficiency and defect-recombination in InGaN light-emitting diodes,” *Phys. status solidi*, vol. 11, no. 3-4, pp. 718–721, 2014.

[56] J. Iveland, L. Martinelli, J. Peretti, J. S. Speck, and C. Weisbuch, “Direct measurement of Auger electrons emitted from a semiconductor light-emitting diode under electrical injection: identification of the dominant mechanism for efficiency droop,” *Phys. Rev. Lett.*, vol. 110, no. 17, p. 177406, 2013.

[57] D. S. Meyaard *et al.*, “Identifying the cause of the efficiency droop in GaInN light-emitting diodes by correlating the onset of high injection with the onset of the efficiency droop,” *Appl. Phys. Lett.*, vol. 102, no. 25, p. 251114, 2013.

[58] Y. Yang, X. A. Cao, and C. Yan, “Investigation of the nonthermal mechanism of efficiency rolloff in InGaN light-emitting diodes,” *IEEE Trans. Electron Devices*, vol. 55, no. 7, pp. 1771–1775, 2008.

[59] J. Hader, J. V Moloney, and S. W. Koch, “Density-activated defect recombination as a possible explanation for the efficiency droop in GaN-based diodes,” *Appl. Phys. Lett.*, vol. 96, no. 22, p. 221106, 2010.

[60] I. E. Titkov *et al.*, “Temperature-dependent internal quantum efficiency of blue high-brightness light-emitting diodes,” *IEEE J. Quantum Electron.*, vol. 50, no. 11, pp. 911–920, 2014.

[61] A. I. Alhassan *et al.*, “High luminous efficacy green light-emitting diodes with AlGaN cap layer,” *Opt. Express*, vol. 24, no. 16, pp. 17868–17873, 2016.

[62] S. Nakamura, “Current status of GaN-based solid-state lighting,” *MRS Bull.*, vol. 34, no. 2, pp. 101–107, 2009.

[63] Q. Lv *et al.*, “Realization of highly efficient InGaN green LEDs with sandwich-like multiple quantum well structure: role of enhanced interwell carrier transport,” *Acs Photonics*, vol. 6, no. 1, pp. 130–138, 2018.

[64] N. G. Weimann, L. F. Eastman, D. Doppalapudi, H. M. Ng, and T. D. Moustakas, “Scattering of electrons at threading dislocations in GaN,” *J. Appl. Phys.*, vol. 83, no. 7, pp. 3656–3659, 1998.

[65] A. Powell *et al.*, “Growth of SiC substrates,” *Int. J. high speed Electron. Syst.*, vol. 16, no. 03, pp. 751–777, 2006.

[66] C. M. Johnson *et al.*, “Recent progress and current issues in SiC semiconductor devices for power applications,” *IEE Proceedings-Circuits, Devices Syst.*, vol. 148, no. 2, pp. 101–108, 2001.

[67] L. Jiu, Y. Gong, and T. Wang, “Overgrowth and strain investigation of (11–20) non-polar GaN on patterned templates on sapphire,” *Sci. Rep.*, vol. 8, no. 1, pp. 1–8, 2018.

[68] D. Zhu, D. J. Wallis, and C. J. Humphreys, “Prospects of III-nitride optoelectronics grown on Si,” *Reports Prog. Phys.*, vol. 76, no. 10, p. 106501, 2013.

[69] W. C. Dash, “Growth of silicon crystals free from dislocations,” *J. Appl. Phys.*, vol. 30, no. 4, pp. 459–474, 1959.

[70] S. L. Selvaraj, A. Watanabe, and T. Egawa, “Influence of deep-pits on the device characteristics of metal-organic chemical vapor deposition grown AlGaN/GaN high-electron mobility transistors on silicon substrate,” *Appl. Phys. Lett.*, vol. 98, no. 25, Jun. 2011, doi: 10.1063/1.3602919.

[71] T. Li, M. A. Mastro, and A. Dadgar, *III-V compound semiconductors : integration with silicon-based microelectronics*. Boca Raton: CRC Press, 2010.

[72] T. Takeuchi, H. Amano, and I. Akasaki, “Theoretical study of orientation dependence of piezoelectric effects in wurtzite strained GaInN/GaN heterostructures and quantum wells,” *Jpn. J. Appl. Phys.*, vol. 39, no. 2R, p. 413, 2000.

[73] P. Waltereit *et al.*, “Nitride semiconductors free of electrostatic fields for efficient white light-emitting diodes,” *Nature*, vol. 406, no. 6798, pp. 865–868, 2000.

[74] A. Strittmatter *et al.*, “Semi-polar nitride surfaces and heterostructures,” *Phys. status*

solidi, vol. 248, no. 3, pp. 561–573, 2011.

[75] J. E. Northrup, “Impact of hydrogen on indium incorporation at m-plane and c-plane In 0.25 Ga 0.75 N surfaces: First-principles calculations,” *Phys. Rev. B*, vol. 79, no. 4, p. 41306, 2009.

[76] M. V Durnev, A. V Omelchenko, E. V Yakovlev, I. Y. Evstratov, and S. Y. Karpov, “Indium incorporation and optical transitions in InGaN bulk materials and quantum wells with arbitrary polarity,” *Appl. Phys. Lett.*, vol. 97, no. 5, p. 51904, 2010.

Chapter 2

Background

This chapter will introduce the general background of semiconductors and basic information of III-nitride semiconductors including semi-polar and non-polar GaN. Then the development of III-nitride on silicon substrates are also presented.

2.1 Semiconductors

Solid state materials can be divided into three classes by their electrical conductivity, namely, conductors, semiconductors and insulators. For an insulator, electrons cannot flow freely within an electric field, leading to a low electrical conductivity. For a conductor, it is opposite from insulator. And for semiconductor, the electrical conductivity is intermediate between a conductor and an insulator. The conductance of semiconductors can be altered by the presence of external energy sources, such as injection current, thermal energy and doping which will be discussed in later sections.

2.1.1 Band Structure

For the electrons of a single crystal, it can exist in several discrete energy levels to form energy bands. The energy band of the highest electron occupied orbital at absolute zero temperature is called valence band, whereas the energy band of the lowest unoccupied electron orbital is called conduction band [1]. There is an energy gap between them, which has no existence of electrons, is the so-called “bandgap”. The bandgap of three kinds of single crystalline materials are shown in the Figure 2.1, the conductors have extremely small or even zero bandgap, whereas the semiconductors and insulators have small and large bandgaps respectively.

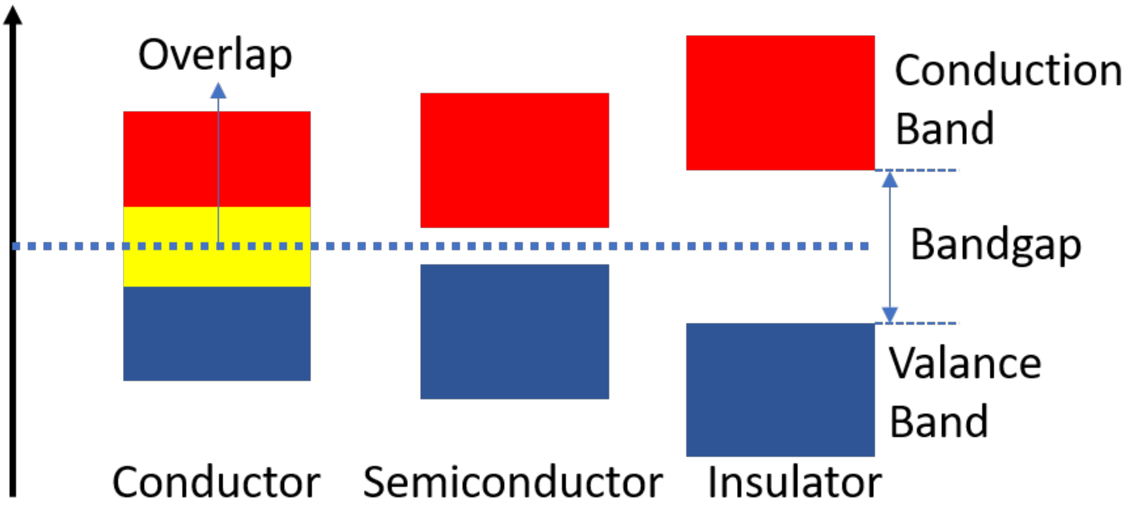

Figure 2.1: The band gap of conductor, semiconductor and insulator respectively.

Based on the crystal momentum, semiconductor materials can be divided into direct bandgap and indirect bandgap. Figure 2.2 shows the diagram of a direct and an indirect bandgap of semiconductor during a process of interband luminescence.

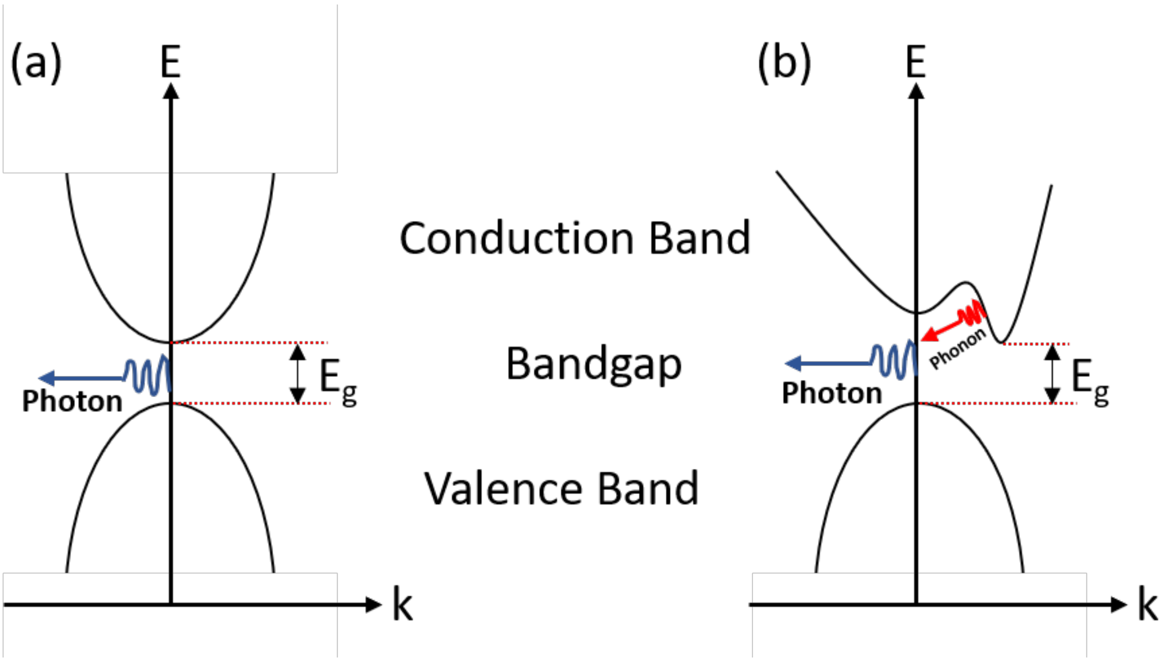

Figure 2.2: Diagram of (a) direct bandgap, (b) indirect bandgap during luminescence.

For the direct bandgap, the electrons in the minimum of conduction band recombine with the holes in the maximum of valence band, emitting photon and sharing the same crystal momentum (k-vector). However, in the indirect bandgap, the transition associates with a disparate value of k-vector. Therefore, the extra momentum is needed to satisfy the conservation of the momentum for the transition, where additional particle will be involved in the process [2]. The involved phonon will convert into heat eventually, resulting in a longer recombination lifetime and lower optical efficacy compared with direct bandgap. Thus, indirect bandgap semiconductor materials are unfavourable for the high-performance emitters.

2.1.2 Doping

For an intrinsic semiconductor material, the concentration of free carriers is limited, thus the electrical conductivity is low. In order to enhance the electrical properties of semiconductor materials, doping is applied to the intrinsic semiconductor materials for the purpose of modulation by the means of introducing impurities intentionally during the epitaxial growth to generate additional free electrons and holes. Two types of doping are classified by the element of dopant. One is n-type (donor) to provide free electrons, the other is p-type (acceptor) to provide free holes. For III-nitride materials, silicon (Si) and magnesium (Mg) are commonly used as n-type dopants and p-type dopants respectively. Si atoms occupy the substitutional position of Ga atoms and leave valence electrons, leading to additional free electrons. On the other hand, gallium (Ga) atoms will be replaced by Mg atoms, consuming the electrons from the valence band. As a result, extra vacancies will be generated in the valence band, forming a p-type semiconductor which is dominated by free holes. So far, Mg is the only p-type dopant for III-nitride materials as no real shallow acceptors have been found in GaN.

2.1.3 Recombination

The electrons from valance band jump into the conduction band by heating-up or electric field and generate holes in the valance band corresponding to a process called carrier generation. Whereas a reverse process which describes the holes be filled in the valence band is referred as carrier recombination. The excess energy from recombination can be released in the form of photons or without photons. Accordingly, the process with photons involved is called radiative recombination, while the one without photons involved is called non-radiative recombination.

There are mainly three types of radiative recombination based on their mechanisms as shown in the Figure 2.3.

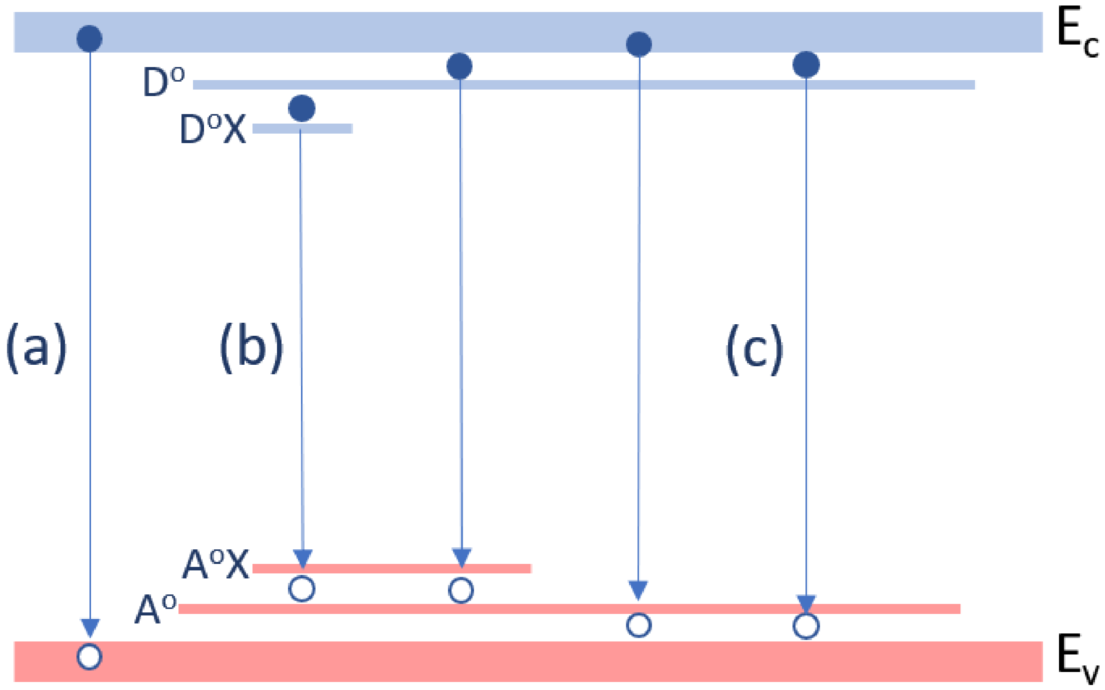

Figure 2.3: (a) band-to-band recombination (b) exciton recombination (c) DAP recombination.

Band-Band recombination [3]**:** The photon energy of emission is the same as the bandgap energy E_g of the semiconductor materials during the recombination process.

Exciton recombination [4], [5]**:** An exciton (X), a bound state which can be described as an electron and electron hole are attracted to each other under the interaction from electrostatic Coulomb force. As a result, a stable energy equilibrium can be achieved by forming donor-bound exciton (D_0X) in the conduction band and acceptor-bound exciton (A_0X) in the valance band. Thus, the exciton has slightly lower energy compare with the unbound electron and hole, leading to a smaller bandgap energy of emitted photon.

Donor-acceptor pair (DAP) recombination [6]**:** In some cases, when the semiconductor material is excited optically or injected carriers at low temperature, electrons and holes can be trapped to form neutral donors (D_0) and neutral acceptors (A_0) respectively. Consequently, the activation energy of the dopants will be reduced, leading to a smaller bandgap energy of emitted photons.

Two types of non-radiative recombination are listed below:

Trap-assisted or Shockley-Read-Hall (SRH) recombination [7], [8]**:** The new energy levels are created within the band gap by impurity atoms or structural defects, also referred to as “traps”. Since traps allow the transition of electrons step-by-step, the released energy will be exchanged in the form of phonons instead of photons. The recombination rate of such a process depends on the minority carrier concentration, which can be expressed as:

$$R_p = \frac{\Delta p}{\tau_p} \text{ (for n≫p), and } R_n = \frac{\Delta n}{\tau_n} \text{ (for n≪p)} \tag{2.1}$$

where $\Delta n,\ \Delta p$ are the density of excited minority electrons and holes respectively, and τ_n, τ_p represents for minority carrier lifetimes of electrons and holes respectively.

Auger recombination: The excited electron in the conduction band recombines with the hole in the valence band. Instead of emitting photon, the released recombination energy transfers to a third particle as kinetic energy and excites it to higher energy level. The third particle eventually loses its excess energy in the form of lattice vibration or thermal energy. Thus, auger recombination process is defined as non-radiative recombination process and the recombination rate can expressed as:

$$\mathrm{R}_{auger} = (C_n \cdot n^3 + C_p \cdot p)\,(pn - n_i^2) \tag{2.2}$$

Where $C_n,\ C_p$ stands for auger coefficients of electron and hole respectively; n and p are electron and hole concentration respectively; and n_i is the intrinsic carrier concentration. For a scenario of excess electron concentration, $\Delta n >> n,\ p$ and it can be simplified as,

$$\mathrm{R}_{auger} = C_n \cdot \Delta n^3 \tag{2.3}$$

To be noticed that auger recombination can be easily produced with high density of carrier concentration as the third particle can only be involved in this process when it is in an unstable high-energy state. Thus, auger recombination is ascribed to a potential reason of efficiency droop [9].

2.1.4 Luminescence

Basically, luminescence is the opposite process to absorption. After electrons in excited states relax from a higher energy state to a lower energy state, photons are spontaneously emitted from atoms. This process is called luminescence. Many situations can result in luminescence. In this thesis, two main types of luminescence are discussed: photoluminescence and electroluminescence.

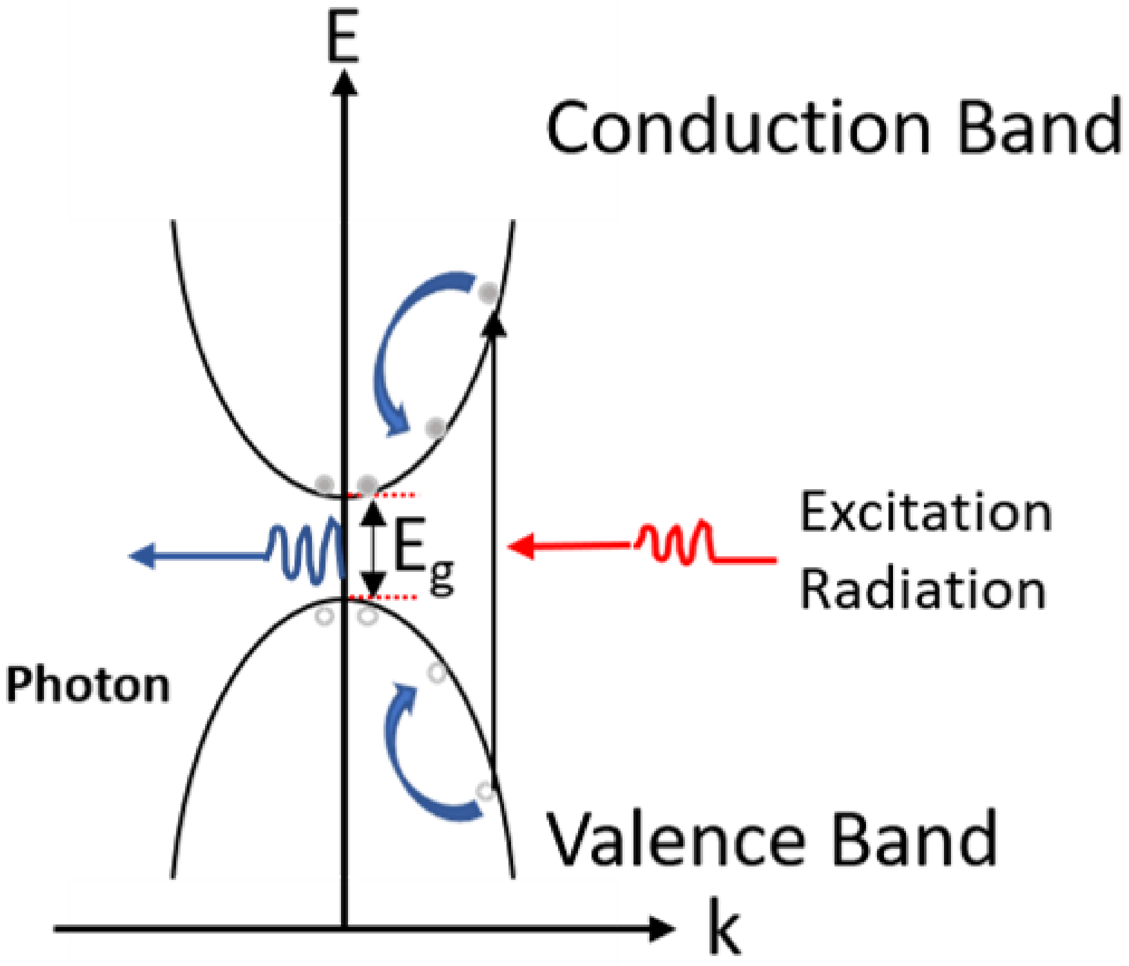

Figure 2.4: Diagram of the photoluminescence process.

In general, photoluminescence indicates that the emission is triggered by the absorption of photons with higher energy. Figure 2.4 is a diagram of the photoluminescence process in direct bandgap material. The excitation radiation has a higher energy than the bandgap of material. In contrast, the cause of electroluminescence is the electrical current across the material.

2.2 III-Nitride Semiconductors

As mentioned in the previous chapter, III-nitride semiconductors including their alloys are an excellent candidate for optoelectronic devices to cover the entire visible spectrum due to their wide bandgaps and direct bandgap structure. This section introduces alterable bandgaps of III-nitrides, their crystal structure and properties, followed by defects in III-nitrides.

2.2.1 Crystal Structure

Group III-nitride semiconductors can be divided into three kinds of crystalline structures: wurtzite (WZ), zincblende (ZB) and rock-salt structure. The most common structure within standardized ambient condition for III-nitrides is WZ structure as its thermodynamically stable property. Thus, in this thesis, all III-nitrides studied in the following chapters are WZ structure. The ZB structure of III-nitrides is metastable state, thus the stable state of ZB structure can only be achieved by means of heteroepitaxial growth on the cubic substrates such as Si [10], SiC [11], MgO [12], and GaAs [13]. However, the intrinsic tendency of converting from ZB into WZ phase always exists as its thermodynamically stable. The rock salt structure is a laboratory form which can only be achieved under high pressures. The structural phase transforms into salt-rock structure under the following estimated values of pressure: 22.9GPa for AlN [14], 52.2GPa for GaN [15], and 12.1GPa for InN [16]. To be noticed that III-nitrides with rock-salt structure cannot be obtained via epitaxial growth.

A cubic unit cell with zinc blende structure typically consists of four group III atoms and four nitrogen atoms. Such a cubic unit cell contains two face-centred cubic sublattices that penetrate each other and offset with a quarter of body diagonal. Each atom within ZB structure can form a tetrahedron with their four adjacent atoms and be regarded as the centre of the tetrahedron. The space grouping of ZB structure is $F\bar{4}3m$ and T_d^2 in Hermann-Mauguin notation and Schoenflies notation respectively.

For a hexagonal unit cell with wurtzite structure consists an in-plane lattice constant a and an out-plane lattice constant c. The lattice constant a is defined as the distance between two adjacent atoms within the same basal plane and the lattice constant c represents the perpendicular distance between two basal planes (cell height). Such hexagonal unit cell contains two interpenetrating hexagonal close-packed (hcp) sublattices which offset along c-direction with the distance of 5/8 cell height. The space grouping of wurtzite structure is $P6_3mc$ and C_{6v}^4 in the Hermann-Mauguin notation and the Schoenflies notation respectively.

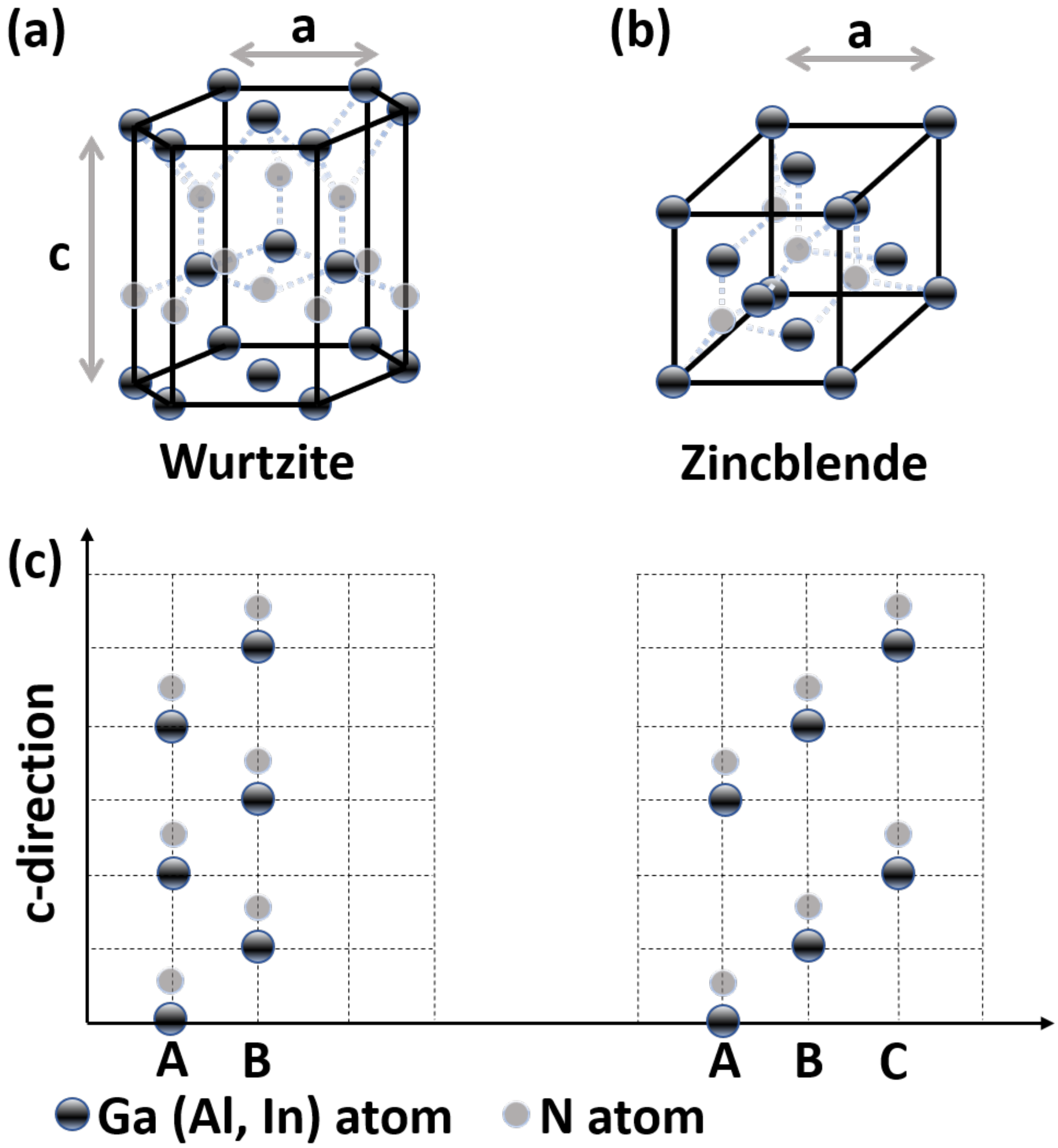

Figure 2.5: Schematics of III-nitride semiconductor with (a): wurtzite structure, (b): zinc blende structure and

(c): corresponding stacking sequences.

The wurtzite and zinc blende structures share some similarities but also some differences. As shown in Figure 2.5, for both structures, each atom is neighboured by four adjacent atoms. However, the stacking sequence of two neighbour diatomic plane shows the difference. For WZ structure, the stacking sequence of basal plane along c-direction is $AaBbAa$ as it contains two alternating diatomic close-packed (0001) planes with Ga-N pairs. The case sensitivity is used to distinguish different constituents. For ZB structure, the stacking sequence for the (111) close-packed planes along c-direction is $AaBbCc$.

The table below contains the lattice constants of III-nitrides with WZ structure: aluminium nitride (AlN), gallium nitride (GaN) and indium nitride (InN)[17][18].

Table 2-1: Lattice constants of different III-nitride materials with different physical form.

Compound	**Sample**	$\boldsymbol{a}$ (Å)	$\boldsymbol{C}$ (Å)
AlN	Bulk crystal	3.1106	4.9795
	Powder	3.1130	4.9816
	Pseudopotential LDA	3.06	4.91
GaN	Bulk crystal	3.189	5.1864
	Relaxed layer on sapphire	3.1892	5.1850
	Powder	3.1893	5.1851
	GaN substrate-LEO	3.1896	5.1855
	Pseudopotential LDA	3.162	5.142
InN	Powder	3.538	5.703
	Pseudopotential LDA	3.501	5.669

LDA: local density approximation;

In order to describe the crystal planes and directions of wurtzite III-nitrides, Miller indices (h,k,i,l) are introduced [19]. As Figure 2.6 shows, the indices (h,k,l) represent the intercept reciprocals along the three directions (a_1,a_2,a_3) which are always angled at 120° to each other within the basal plane, and l indicates the intercept reciprocals along c axis. In wurtzite structure, as $i=-(h+k)$, thus an abbreviated form of (h,k,l) can also be denoted.

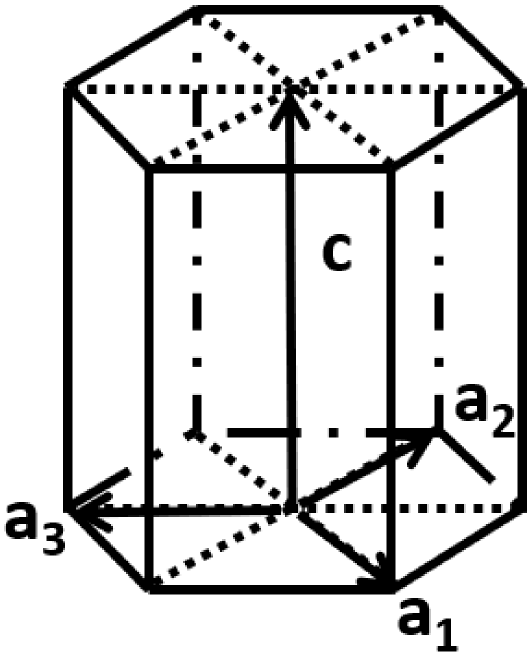

Figure 2.6: Bravais Miller indices in a wurtzite unit cell.

The WZ structure exhibits non-centrosymmetric property, specifically, it has no inversion symmetry, leading to the existence of two polar directions which are defined as (0001) and (000-1) respectively. For the (0001) plane, which is also referred as Ga-polar, is terminated with group III atoms on the outer surface plane, while the (000-1) plane (N-polar) is terminated with N atoms. Normally, Ga-polar GaN has many practical applications as its smooth surface, whereas the N-polar GaN exhibits a rough surface featured with hexagonal hillocks. The polarity also has many impacts on surface morphology, internal polarisation, chemical property, defect generation and impurity incorporation.

The ZB structure GaN material is considered as one of approaches to produce high efficiency green/yellow emission emitters due to the centrosymmetry in crystal structure, leading to the absence of spontaneous and piezoelectric polarisation fields [20]. In addition, ZB InGaN has a lower bandgap energy up to 0.14 eV at room temperature [21], [22] compare with WZ InGaN, therefore, lower In content would require which can allow GaN grow at higher temperature to reduce defect density. However, ZB GaN is in a metastable phase which is easily to transform into WZ structure. Thus, precise control of crystal polytype is required for ZB GaN growth to minimise the amount of WZ inclusions. Currently, only few reports investigated the LED devices on ZZB GaN with full LED structure [23], [24]. The best results are from Stark et al. which was reported a IQE at 36 % on green InGaN based LEDs with 516 nm emission wavelength by estimating with cathodoluminescence intensity ratio at 78K and 300K [24].

2.2.2 Alterable Bandgaps of III-Nitrides

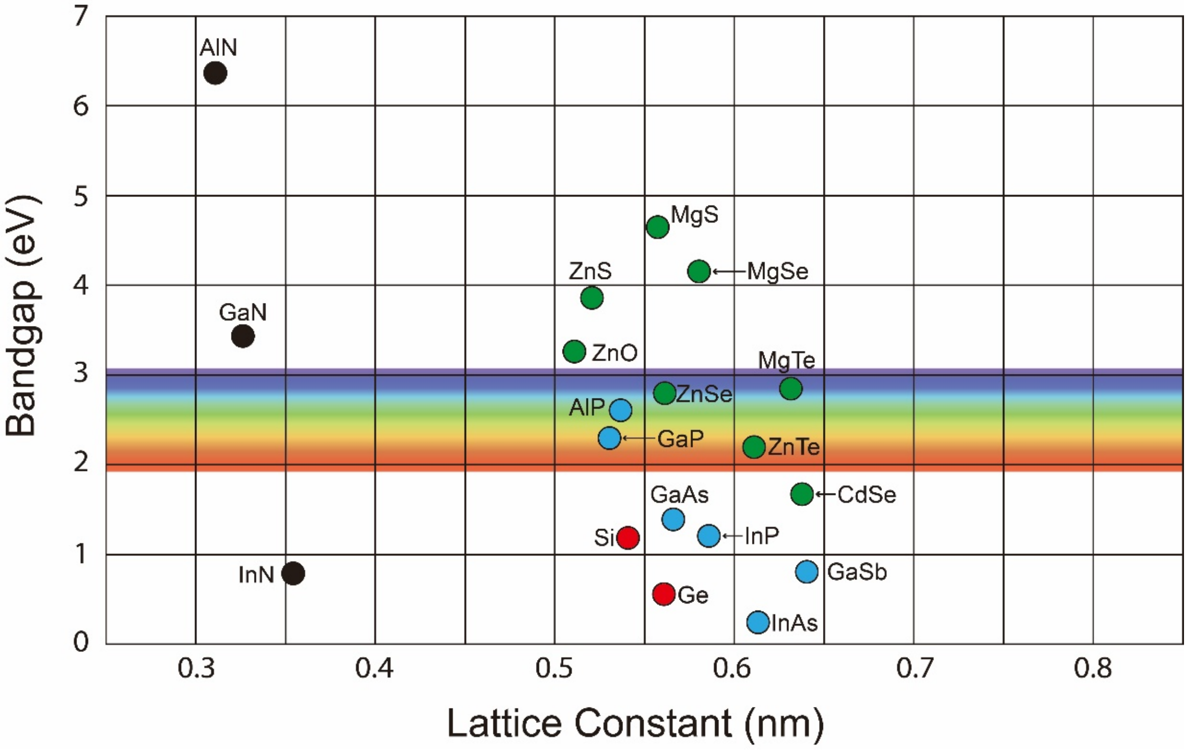

Figure 2.7: Bandgap of different materials as function of lattice constant at room temperature (modified from [25]*).*

A photon is generated when the radiative recombination process occurs in a direct bandgap. The transitional energy E and the wavelength λ of the emitted photon are followed by Planck equation which is described as [26]:

$$\lambda = \frac{hc}{E} \tag{2.4}$$

where h is the Planck constant and c is the light speed in vacuum condition.

As mentioned at the beginning of this section, the III-nitride semiconductors have a wide bandgap range. Thus, the luminescence of III-nitride based optoelectronic devices covers a wide spectrum range from deep UV to infrared. Figure 2.7 is the wavelengths and lattice constant of some typical semiconductor materials. From that figure, the alloys of III-nitrides (black spots) have linear lattice constants that can be illustrated by Vegard's law.

$$a_{A_xGa_{(1-x)}N} = (1-x)a_{AN} + xa_{GaN} \tag{2.5}$$

In this equation, element A represents In or Al. $a_{A_xGa_{(1-x)}N}$ represents the lattice constant of the alloy. a_{AN} and a_{GaN} are the lattice constants of InN or AlN and GaN respectively.

The luminescence wavelength of III-nitride alloys corresponds to the bandgaps. Similar to lattice constants, bandgaps of III-nitrides have a linear relation from the smallest for InN to the largest for AlN. The emission wavelengths depend on the composition of the compound. For InN, the wavelength is infrared and deep ultraviolet (DUV) for AlN. Table 2-2 shows the bandgap energy and emission wavelength of III-nitride materials [27].

Table 2-2: Bandgap and emission wavelength of III-nitride materials.

Material	Bandgap (eV)	Wavelength (nm)
AlN	6.42	193
GaN	3.42	362
InN	0.78	1589

Thus, the wavelength of III-nitride material is tuneable by creating ternary alloys with AlN, GaN and InN. In DUV to UV range, the wavelength can be obtained by different aluminium composition of the AlGaN alloy. From UV to infrared, InGaN alloy can cover the range by altering the indium composition. Consequently, the alterable wavelength and wide range of spectrum make III-nitrides ideal to be used for opto-electronic devices.

2.2.3 Properties

The general properties of GaN are summarized in Table 2-3 and compared with other III-V semiconductors such as GaAs and InP in aspects of electron mobility, electron saturation velocity, breakdown field, thermal conductivity and melting point.

Table 2-3: Semiconductor material properties at 300K [25], [28]–[35].

Material	Electron Mobility ($cm^2V^{-1}s^{-1}$)	Electron Saturation Velocity (10^7s^{-1})	Breakdown Field ($kVcm^{-1}$)	Thermal Conductivity ($W\cdot cm^{-1}K^{-1}$)	Melting Point (˚C)
GaN	1245	2.5	5000	1.3	2500
GaAs	9400	2.0	400	0.55	1238
InP	4000	0.6	500	0.68	1062

The electron mobility is denoted by how quickly carriers (electrons and holes) flow through the material under an electric field. Scattering is what determines the electron mobility of semiconductors. The direction, momentum or energy of carriers can be changed by ionized impurities, defects and phonons (lattice vibrations) which is referred as scattering event. Therefore, the higher the frequency of scattering events, the lower the electron mobility. Normally, the electron mobility of GaN epilayer grown on foreign substrate is around 1000 $cm^2V^{-1}s^{-1}$. So far, the highest electron mobility is 1245 $cm^2V^{-1}s^{-1}$ achieved on bulk GaN from HVPE [35]. In addition, high electron saturation velocity and large breakdown voltage make GaN to be a promising candidate of high-power, high-frequency electronic devices.

In terms of physical properties, GaN exhibits high thermal conductivity and high melting point which allow GaN-based devices can competently work under high-temperature condition. For the chemical properties of GaN, Ga-polar GaN exhibits high stability and can resist the etching from the common acidic and alkaline solutions [36]. However, N-polar GaN can be easily etched by a variety of etchants, typically potassium hydroxide and phosphoric acid are the most common etchants for testing [37].

2.3 Semi-polar and Non-polar III-Nitrides

Conventional polar GaN-based devices are significantly influenced by polarisation induced

QCSE, leading to limited efficiency of optical performance. Reducing strain-induced piezoelectric fields by strain relaxation and shielding active region from QCSE by screening effect are the two main approaches to mitigate this issue. However, the polarization induced QCSE still cannot be eliminated fundamentally especially when it comes to longer wavelength. The most promising way to eliminate or effectively reduce the QCSE is to grow GaN along with either non-polar or semi-polar orientation.

2.3.1 Semi-polar and Non-polar Planes

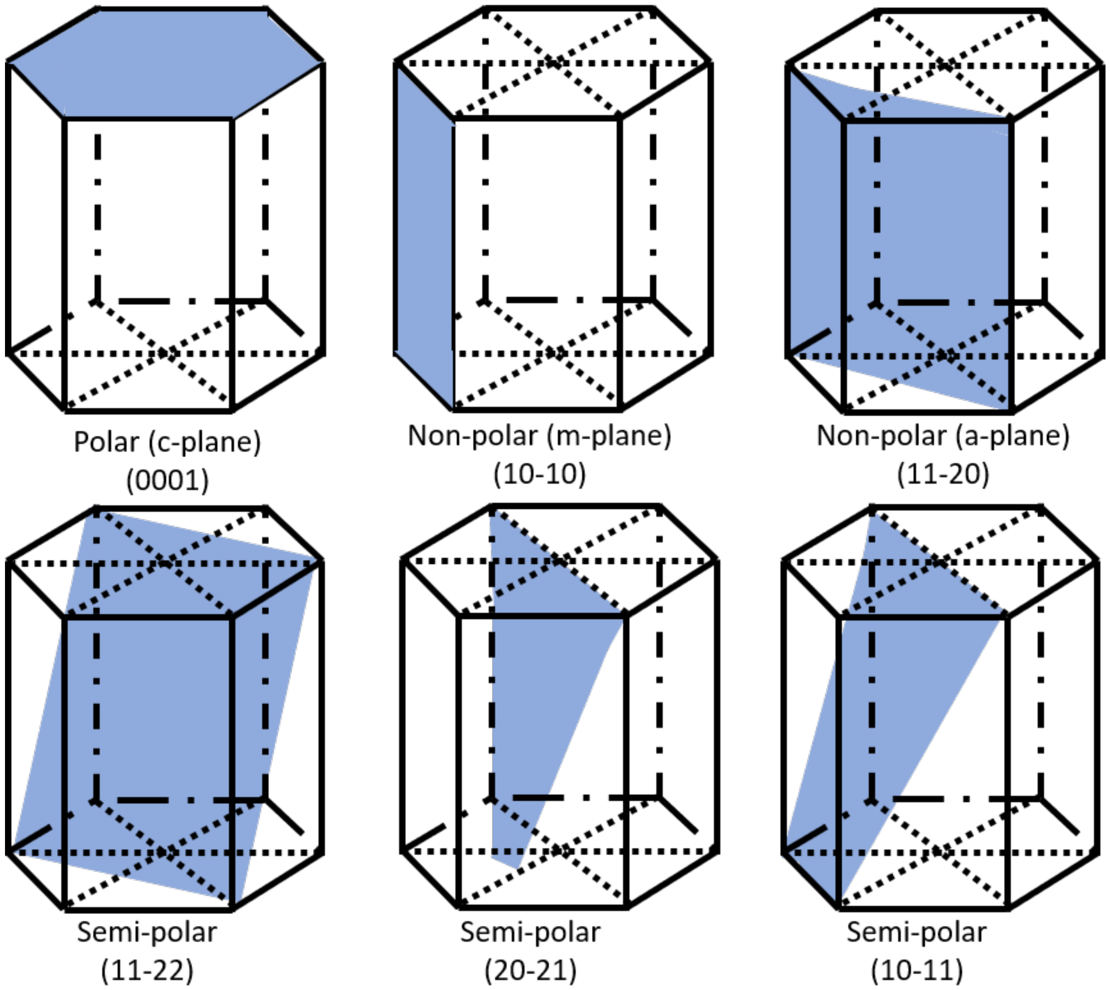

Figure 2.8: Six common crystallographic planes in wurtzite GaN.

Figure 2.8 shows six common crystallographic planes in wurtzite GaN, polar type, and their Miller indices. (0001) *c*-plane is the most widely used polar plane for GaN-based devices. Two non-polar planes: (1-100) *m*-plane and (11-20) *a*-plane are perpendicular to *c*-plane. (11-22) plane, (20-21) plane and (10-11) plane are divided into semi-polar planes which are inclined to the *c*-plane between 0° to 90°. For instance, (11-22) plane exhibits an inclination angle of 58.41° respect to the *c*-plane [38].

The inclination angle respect to the *c*-axis is critical for reduction or elimination of piezoelectric polarization in InGaN/GaN quantum well structures. A conventional coordinate system can convert into a new coordinate system by matrix rotation. Correspondingly, a new elastic tensor and piezoelectric coefficient of III-nitrides can be concluded as well. Thus, Northrup reported the polarization with different In composition in InGaN/GaN structure as a function of the inclination angle respect to c-direction, which is shown in Figure 2.9.

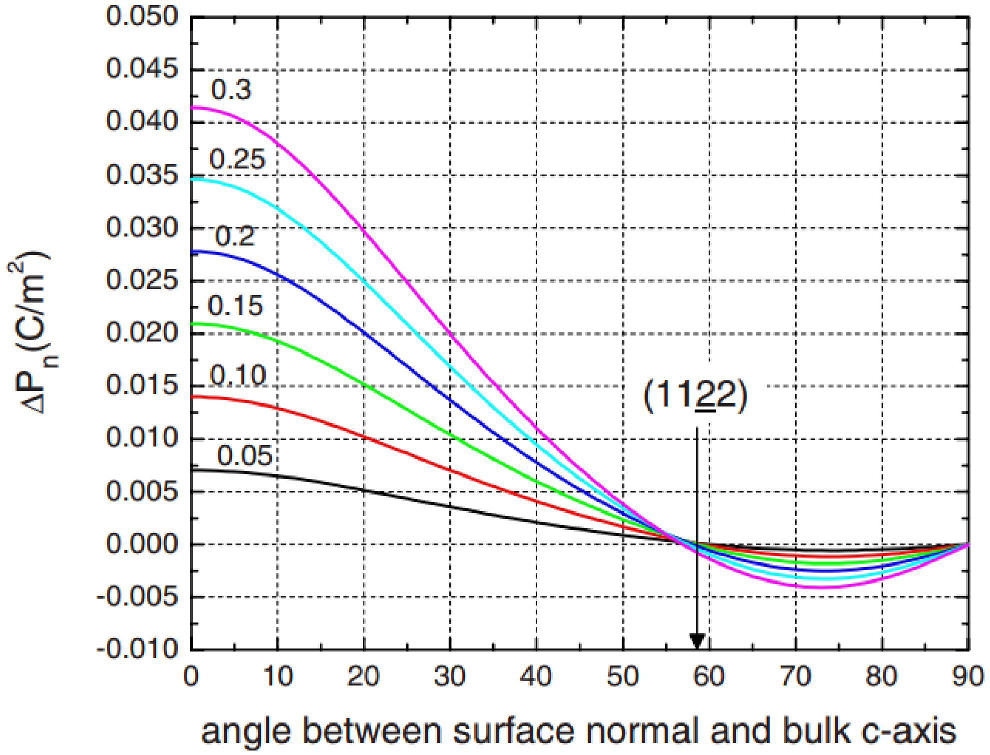

Figure 2.9: Schematic of polarization with different In composition as a function of inclination angle respect to c-direction (Modified from [39]*).*

All the polarizations of different indium contents start to decrease with the increase of the inclined angle and reach to zero polarization at about 55°, followed by a negative reverse before terminating at zero polarization at 90°. The two inclination angles of zero polarization points are non-polar planes. Semi-polar (11-22) plane shows a significant reduction in piezoelectric polarisation which is approximately 10% of (0001) c-plane.

2.3.2 Crystallographic Defects in Semi-polar and Non-polar III-nitrides

For a crystalline material, the atoms are supposed to be situated in a repeating or periodic array with atomic distance and in a repetitive three-dimensional pattern. However, defects always occur and affect the behaviour of the materials. In particular, for semi- or non-polar heteroepitaxial GaN grown on foreign substrates, there exhibit a high density of defects during the initial growth of GaN films. According to the geometry or dimensionality, the crystallographic defects (microscopic defects) can be classified into three types: point defects (zero-dimensional), line defect (one-dimensional) and planar defect (two-dimensional). In addition to other macroscopic defects which are normally have much larger than microscopic size, such as bulk defects (three-dimensional).

Point Defects

A point defect is a zero-dimensional defect in a form of an isolated crystal lattice with distortion. According to the intrinsic or extrinsic origin of the crystal lattice, the point defects can be classified into four kinds as shown in Figure 2.10. The intrinsic point defect is normally associated with the presence of atomic vacancies (absent atoms or antisites) or atomic interstitials (adding atoms), whereas extrinsic point defects typically related to the existence of foreign atoms in the crystal. A foreign atom can occur in two forms: substitutional or interstitial. In III-nitrides, nitrogen (N) vacancy, gallium (Ga) vacancy and extrinsic substitutional atoms like silicon, oxygen and carbon impurities are commonly occurred during the epitaxial growth. It is believed that “unintentional n-type doping” is attributed to N vacancy or oxygen impurity [40], and the “yellow-band emission” is caused by Ga vacancy [41].

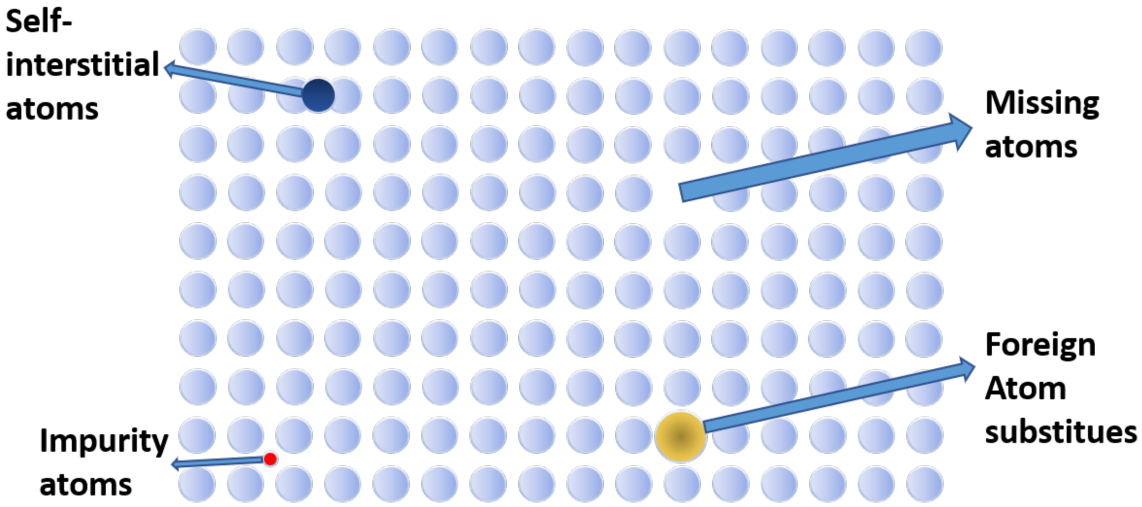

Figure 2.10: Diagram of point defects.

Line Defect

A type of dislocation is called line defect which exhibits the misalignment of many atoms in length. Threading dislocations (TDs) are commonly occurred as a type of line defects which will propagate from substrate interface to the top surface in c-plane III-nitrides. In order to characterise the lattice distortion caused by a dislocation, a Burgers vector and dislocation line are introduced. A Burgers vector ***b*** indicates the magnitude of displacement resulting from a dislocation and the distortion direction of the lattice. Generally, there are three types of threading dislocations which are shown in Figure 2.11: edge dislocations, screw dislocations and mixed dislocations (combining of both two types). For the edge dislocation, an extra half-plane is introduced into the crystal structure and the Burgers vector is perpendicular to the dislocation line. For the screw dislocation, the atoms from one plane slip in a form of helical pattern in the crystal and the Burgers vector is parallel to the dislocation line.

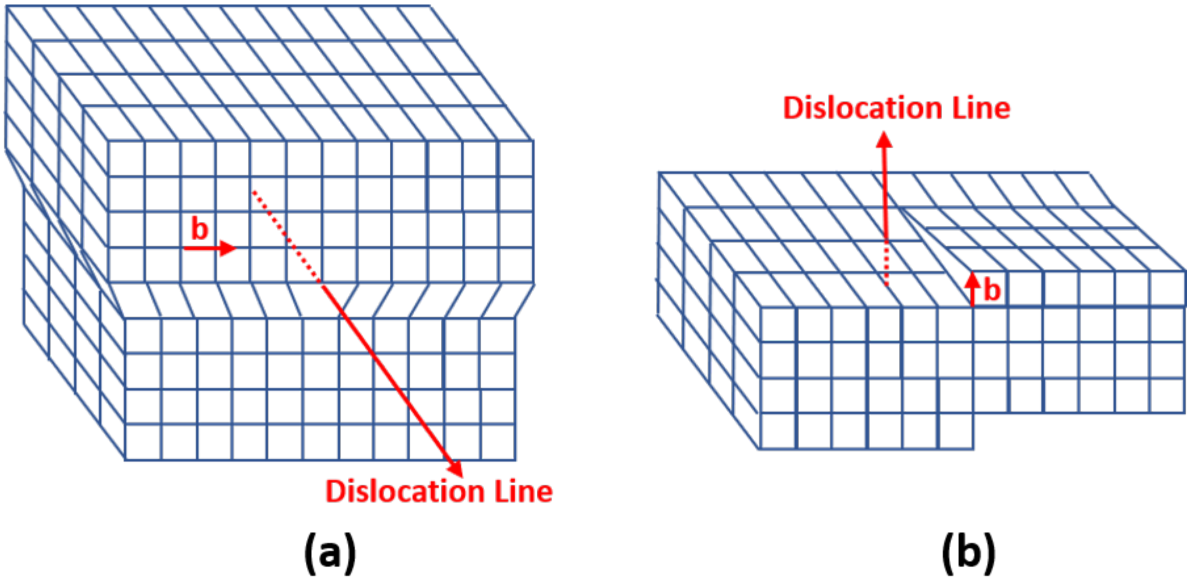

Figure 2.11: Schematics of (a): edge dislocation, (b): screw dislocation.

The misfit dislocation (MD) is another type of line defect in III-nitrides which is caused by the induced strain from in-plane lattice-mismatch and localized at the substrate or layer interface. Figure 2.12 shows the formation of MD is caused by the lattice-mismatch between epitaxial layer and substrate. Normally, when the strained epitaxial layer exceeds the critical thickness h_c, MDs will be generated to release the strain. The relationship between MD and the critical thickness h_c are shown below [42]:

$$h_c = \frac{\boldsymbol{b}}{2\pi f}\frac{(1 - v cos^2\alpha)}{(1 + v)\, cos\,\lambda}\left(\ln\frac{h_c}{\boldsymbol{b}} + 1\right) \tag{2.6}$$

where f, $\boldsymbol{b}$ and v represent the misfit parameter, Burgers vector of dislocation and Poisson's ratio respectively. α is the angle between the dislocation line and Burgers vector, λ is denoted as the angle between slip direction and a line perpendicular to the dislocation line. In semi-polar (11-22) orientation of III-nitrides, it has been reported that misfit dislocations exhibit a dislocation line along the m-direction [43], [44].

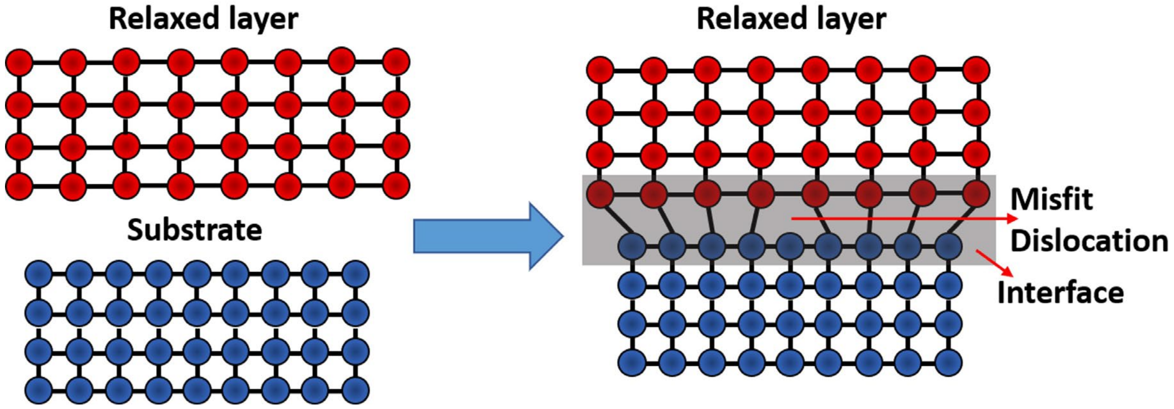

Figure 2.12: The formation of misfit dislocation.

Planar Defect

Stacking fault (SF) is a type of planar defects which exhibit a disruption of the stacking sequence at one direction (vertical, horizontal, or inclined) of the crystal. For a normal III-nitride wurtzite structure, it consists of *ABABAB* stacking sequence of basal planes along *c*-direction as shown in Figure 2.13. However, the stacking sequence could be intrinsically disrupted by the substitution or insertion of wrong bilayer C, or extrinsically by an insertion of extra layer. Based on the layers with defects, the BSF could be categorized into three kinds, I_1-type (ABCBCB), I_2-type (ABCBAB) and *E*-type (ABCABA) respectively. I_1-type BSFs are typically generated by removing or inserting a bilayer during epitaxial growth as the formation energy is the lowest compared with other types of BSF [45]. Therefore, I_1-type BSFs commonly occurred in semi-polar and non-polar III-nitrides. I_2-type BSFs are formed by a shear of the basal plane during a strain relaxation process. *E*-type BSFs can only be produced from an insertion of an extra layer during epitaxial growth as the highest formation energy. BSFs are normally bounded by partial dislocations and can be terminated at internal interfaces (for example, at grain boundaries). Thus, BSFs have limited effect on conventional c-plane III-nitride. However, for semi-polar and non-polar cases, growth direction is inclined to the basal plane, thus, BSFs could propagate to the sample surface, leading to a deterioration of surface morphology and crystal quality.

Prismatic stacking fault (PSF) is another type of planar defect which normally lie either on (1-100) or (11-20) planes. The (1-100) PSF is typically associated with the atomic steps at the substrate surface and could be a part of closed faulted domains by *I₁*-type BSFs. The (11-20) PSF has extra shear of displacement and slightly lower formation energy than (1-100) PSF [46].

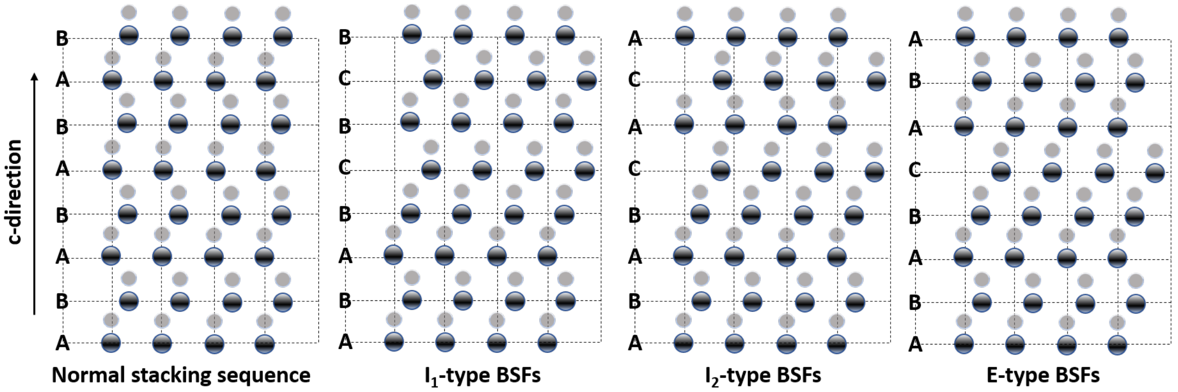

Figure 2.13: Schematic diagrams of III-nitrides in normal stacking sequence, I1-type, I2-type, and E-type BSFs in wurtzite along c-direction.

Bulk Defect

The bulk defect is a three-dimensional defect which generally occurs on a much larger scale than the microscopic defects. These defects can be observed in form of cracks and voids in III-nitrides. For the III-nitride growth on silicon substrate, cracks can be easily generated due to the large thermal coefficient difference between adjacent materials. Voids are normally associated with small regions without atoms, and which can be considered as clusters of vacancies.

2.3.3 Indium incorporation

Indium incorporation varies with different crystal orientations in III-nitrides. Strain state [47] and surface atomic configuration [39] are considered as primary causes.

The elastic strain can lead to a strong enlargement of bandgap for strained InGaN compared with unstrained one. The minimum bandgap for strained InGaN can be obtained with the inclination angle respect to c-plane ranging from 45° to 60°. Thus, (10-11) and (11-22) are considered as an excellent candidate to achieve long emission wavelength with high In content.

In addition, the surface atomic configuration of GaN along different orientations has a great impact on In incorporation, which have been reported by many papers [48]–[50]. In can incorporates in adlayer sites and in threefold coordinated sites to form bonds with three N atoms on (0001) surface, while it could incorporate in binding sites which bond with one or two N atoms on the (10-11) or (11-22) surfaces. Moreover, In atom can be incorporated below the adlayer on the (11-22) plane due to lower In chemical potential. In this respect, (11-22) orientation is expected to be more favourable for growth of InGaN with high In composition.

In practice, Zhao et al. have also investigated the In incorporation for several semi-polar and non-polar planes, including (11-22), (20-21), (30-31) and (10-10) planes. Under the same growth condition, results exhibit that (11-22) plane poses the highest In incorporation rate which is in good agreement with the theoretical study [51]. Overall, these results indicate (11-22) plane could provide a solution to achieve a high-In-content active region on III-nitrides.

2.4 III-Nitrides Epitaxy on Silicon Substrates

This section firstly introduces the development of III-nitrides epitaxy on silicon substrates, and then followed by the current issues such as lattice mismatch, thermal expansion coefficient mismatch and Ga melt-back etching.

2.4.1 Development of III-Nitrides Epitaxy on Silicon Substrates

The extensive research of III-nitrides epitaxy on silicon substrates started from the late 1990s due to enormous demand for power electronic devices and SSL market. Guha performed the first GaN-based LED on (111) Si by using MBE in 1998 [52]. A thin AlN buffer layer was inserted prior to the GaN film to avoid melt-back etching as Al requires high bonding energy to form alloy with silicon substrate. The performance of LED exhibited a high turn-on voltage. However, both surface morphology and crystal quality on (111) Si are not comparable with contemporaneous sapphire one. The issues of considerable high lattice mismatch and large thermal expansion coefficient mismatch between two hetero-materials will lead to a high density of dislocation and surface crack, leading to a deterioration on the performance of III-nitrides devices. Accordingly, in-situ and ex-situ approaches have been applied to eliminate these issues.

For in-situ approaches, including Si_xN_y interlayer, low-temperature (LT) AlN layer, (AlN/GaN or AlGaN/AlN) superlattices (SLs) layer and AlGaN buffer layer, they were widely performed in the (111) Si growth. Lahreche et al. demonstrated the inserting process of in-situ Si_xN_y interlayer to form self-organized islands on the template surface. Thus, the sequent GaN growth will occur a 3D island growth and then converts to a 2D lateral growth. Thus, a significant reduction of dislocation was observed [53]. LT-AlN, SLs layer and AlGaN buffer layer served as strain management layers to counterbalance the induced thermal tensile strain during the cooling-down process which is the primary cause of the surface crack. In the meantime, the strain state transits from tensile to compressive with the increase of AlGaN buffer layer thickness. The variation of the stress will result in bending of dislocations to the lateral plane, leading to a substantial annihilation of dislocations [54], [55]. Therefore, the dislocation suppression is enhanced as a result of strain field-induced dislocation bending.

Patterned Si substrates are widely used as an ex-situ approach to ease the curvature of the substrate and strain relaxation via selective growth as shown in Figure 2.14. Dielectric grid mask (SiO_2 or Si_xN_y) is commonly deposited on a thick GaN template for subsequent selective area growth. Besides, a strain engineering structure is critical for stress release, such as the area of the open window and the thickness of GaN. Honda et al. [56] reported a crack-free GaN film can be achieved within the area of the open window less than 400×400 μm^2 and the best crystal quality GaN with 1.5 μm thickness is achieved in 200×200 μm^2 window areas. Moreover, etched trench grid with dielectric grid mask can be applied to release the tensile stress across the whole wafer. A crack free GaN with 2 μm thick in 320×320 μm^2 square islands patterned was reported by Zhang et al. [57]. However, such ex-situ approaches suffered from the edge effect which is in a form of inhomogeneity in GaN thickness, leading to a difficulty in the following device fabrication. In addition, the etched area poses a high risk of melt-back etching as AlN buffer layer shows the poor separation from Si substrate to GaN.

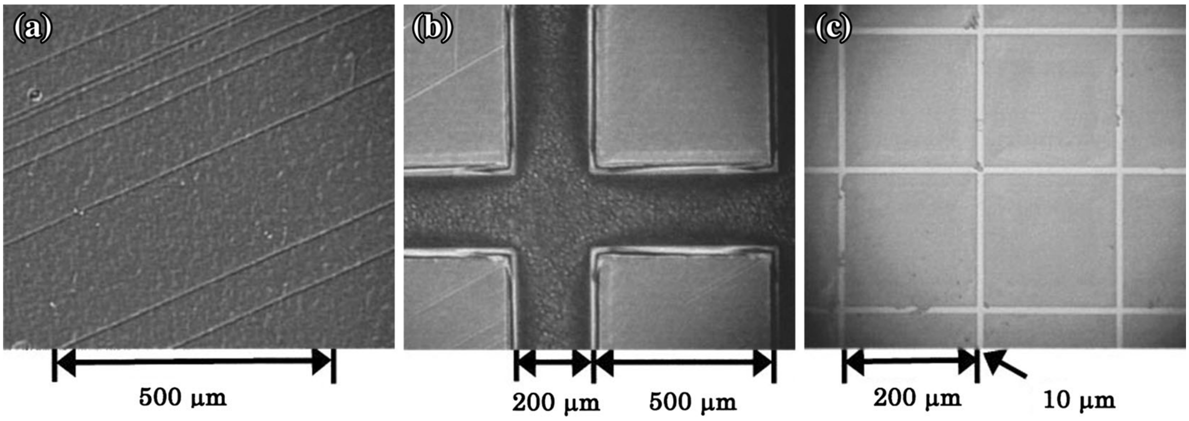

Figure 2.14: Patterned Si substrate with dielectric mask [56].

2.4.2 Lattice Mismatch

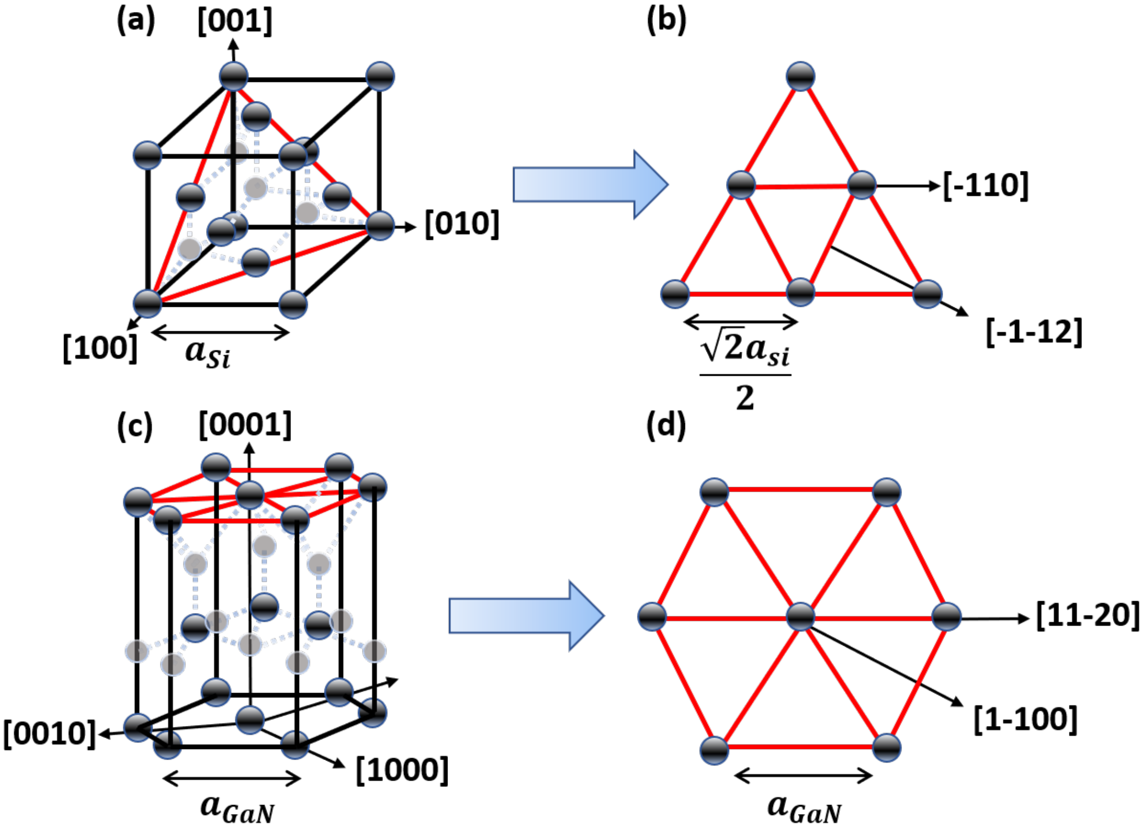

Figure 2.15: Schematic: (a): cubic crystal structure of Si; (b): atomic arrangement of (111) Si surface; (c) wurtzite crystal structure of GaN; (d): atomic arrangement of (0001) GaN surface.

The typical wurtzite GaN with six-fold symmetry structure is more favourable for the (111) Si surface with a three-fold symmetry rather than (001) Si surface with a four-fold symmetry, as the growth of GaN contains two preferred rotational alignments on (001) Si surface and leads to extremely rough surfaces [58]–[61]. Therefore, (111) Si is preferred for III-nitrides epitaxial growth. The c-plane GaN is grown with an in-plane orientation of GaN (1-100) ∥ Si (-1-12) and GaN (11-20) ∥ Si (-110) on the (111) Si substrate as shown in Figure 2.15. Under this rotational alignment, the lattice mismatch between c-plane GaN and (111) Si is calculated by the equation below:

$$\frac{a_{GaN}-\frac{\sqrt{2}a_{Si}}{2}}{\frac{\sqrt{2}a_{Si}}{2}} = -16.9\% \tag{2.7}$$

Where $a_{Si} = 5.432\ \text{Å}$ is the in-plane lattice constant of cubic silicon and $a_{GaN} = 3.190\ \text{Å}$ is that of wurtzite GaN. Thus, GaN suffers tensile stress from the (111) Si substrate due to a lattice mismatch of -16.9% between them.

2.4.3 Thermal Expansion Coefficient Mismatch

The in-plane thermal expansion coefficient of (111) Si and GaN are 2.59 $\times\ 10^{-6}/K$ and 5.59 $\times\ 10^{-6}/K$ respectively. The existence of considerable high thermal expansion coefficient mismatch between GaN film and (111) Silicon substrate could easily generate cracking due to the strong tensile stress introduced during the cooling-down process. Raghavan et al. [54] reported the critical thickness of a crack-free GaN epilayer grown upon the HT-AlN buffer layer is approximately 250 *nm* which is too thin to achieve a satisfied crystal quality for subsequent high-performance device fabrication. Corresponding methods for strain management have been explained in the 2.4.1 section, including LT-AlN interlayers, AlGaN intermediate layers and Al(Ga)N/GaN SLs.

2.4.4 Melt-back Etching

The GaN growth cannot be performed directly on the Si substrate as ammonia can easily react with Si to form a thin Si_xN_y layer with amorphous morphology [62] at high temperature during the growth, leading to an obstacle for subsequent GaN growth. In addition, gallium (Ga) can also react with Si substrate when the temperature over 1000 ˚C, forming a eutectic alloy [63], [64]. Such reaction is referred as "Melt-back etching" which can out-diffuse the Si up to the GaN layer and cause polycrystalline GaN growth, leading to deterioration for the morphology of GaN surface as shown in Figure 2.16. Thus, a Ga-free buffer layer is essential to grow prior to the GaN layer to prevent from melt-back etching occurring. AlN buffer layer is a common candidate for coverage on Si substrate. In addition, for the subsequent GaN growth, LT-AlN can suppress the generation of dislocations in the GaN firm which is discussed in Chapter 2.4.1.

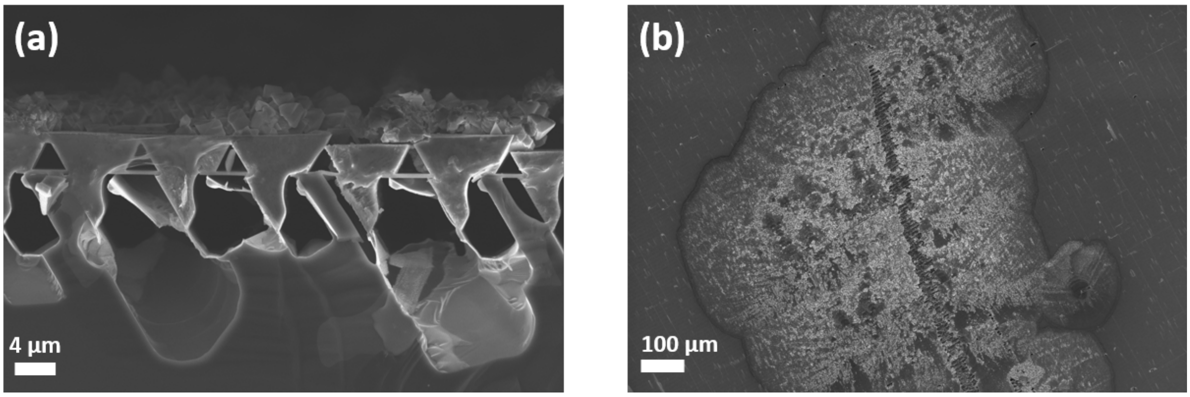

Figure 2.16: The morphology of (11-22) GaN on patterned (113) silicon with melt-back etching: (a) Cross-section image, (b): Top-view image.

2.4.5 Epitaxy Mechanism for semi-polar and non-polar GaN on Patterned Silicon Substrate

In order to achieve a large inclination angle GaN respect to the c-direction on Si substrate, a Si substrate with high index (11h) has to be adopted. The single-crystalline semi-polar GaN films have been achieved on non-patterned (112), (113), (114), (115) and (116) Si substrates. However, the GaN films show a low crystal quality based on X-ray diffraction (XRD) omega scans of GaN (10-11) and (11-20) reflections [65]. For higher index Si substrate such as (117) Si, the GaN growth occurs in a form of polycrystalline with a rough morphology as shown in Figure 2.17. Therefore, it exhibits the utmost difficulty in obtaining semi-polar or non-polar GaN on planar Si substrate.

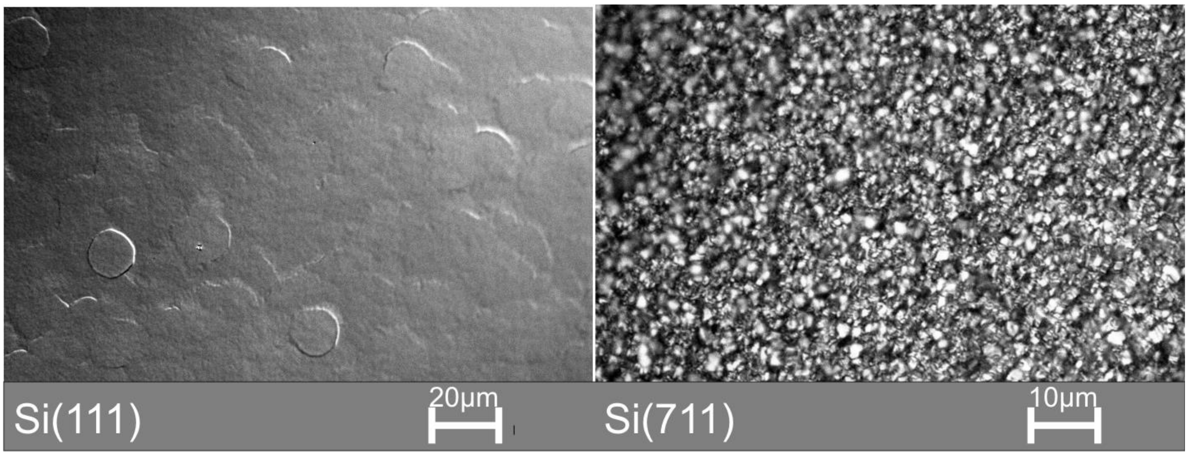

Figure 2.17: Optical microscope images of GaN film grown on (111) Si and (117) Si [66].

Another approach is using high index Si or their vicinal surface (such as the surface with slightly miscut orientation) to form inclined (111) Si facet by a selective area anisotropy wet etching technique. Subsequent selective area c-axis oriented GaN growth can be carried out on the inclined (111) Si facet, forming semi-polar or non-polar GaN as shown in Figure 2.18. Many Si anisotropic etchants, such as NaOH, KOH, LiOH, CsOH, RbOH, NH_4OH, EDP, TMAH etc., only KOH, EDP and TMAH, can provide proper selectivity against the dielectric mask materials while preserving proper Si etching rate. And KOH is commonly used as anisotropic etchant as low hazarder and controllable etching rate. Si substrates of different orientations can be etched in different etching rates, for example, (111) facet is etched at a lower rate than other planes due to the stronger bonds or a larger number of bonds [67]. Thus, the anisotropic etching can be carried out on Si substrates due to the different surface atomic arrangement along different orientations, resulting in the formation of vicinal (111) facets with a certain inclination angle.

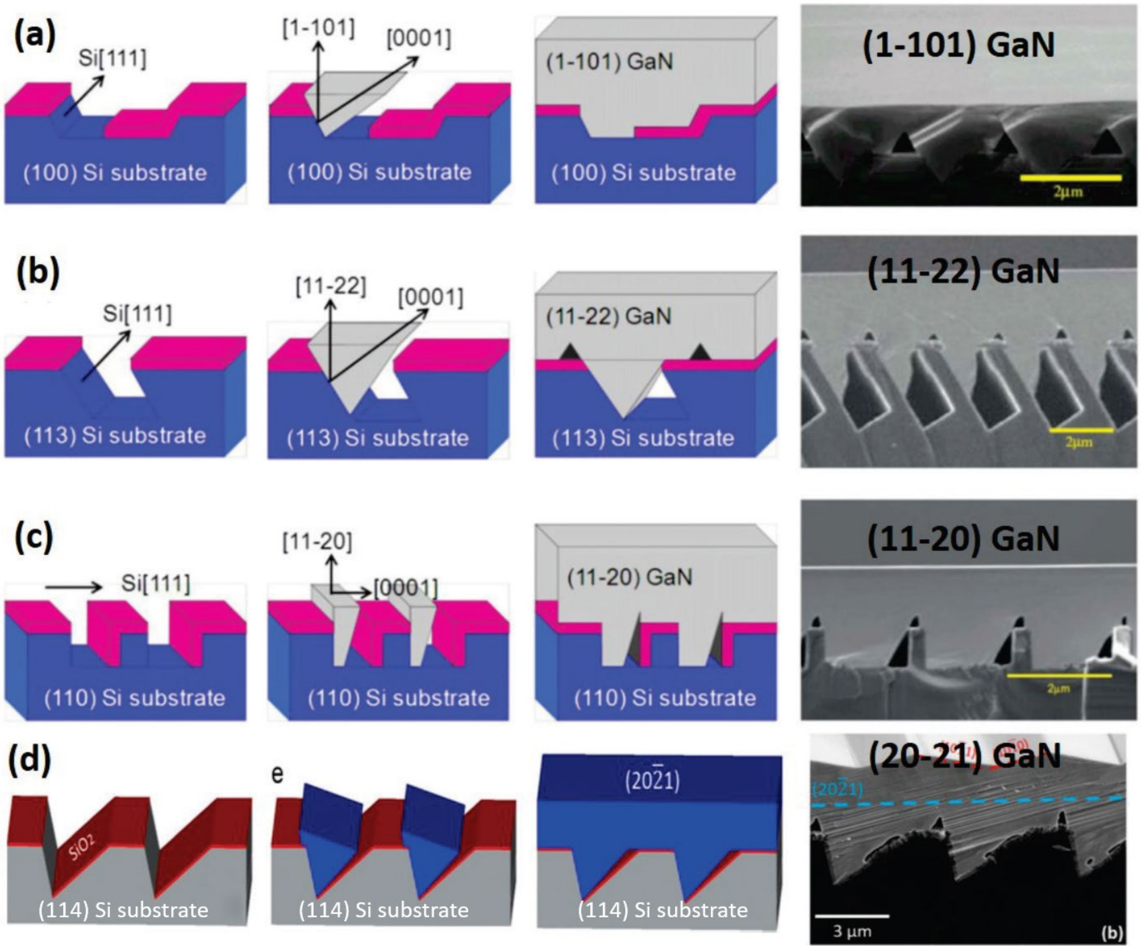

Figure 2.18: Diagrams of GaN growth on different patterned silicon substrates and corresponding cross-section SEM images [67] *[63].*

It has been proven that semi-polar (11-22) GaN can be achieved on patterned (113) Si substrate via selective area growth (SAG) [68]–[70]. An anisotropy wet etching is carried out on a pre-deposited dielectric stripe mask along (21-1) axis of (113) Si substrate to form grooves with (1-11) and (-11-1) lateral facets and (011) or (113) bottom facets. Subsequent GaN SAG can only be performed on (1-11) Si facet and coalesces with adjacent stripe to form a semi-polar (11-22) GaN surface which is parallel to (113) Si substrate. However, such growth mode results in a "closed" configuration after the coalescence of GaN, increasing the risk of melt-back etching as (-11-1) Si facets are unable to receive the protection from Ga flux. In addition, any misalignment of transferring stripe pattern will lead to rough (111) Si facet with steps after anisotropic etching as shown in Figure 2.19, deteriorating the morphology of GaN surface [70].

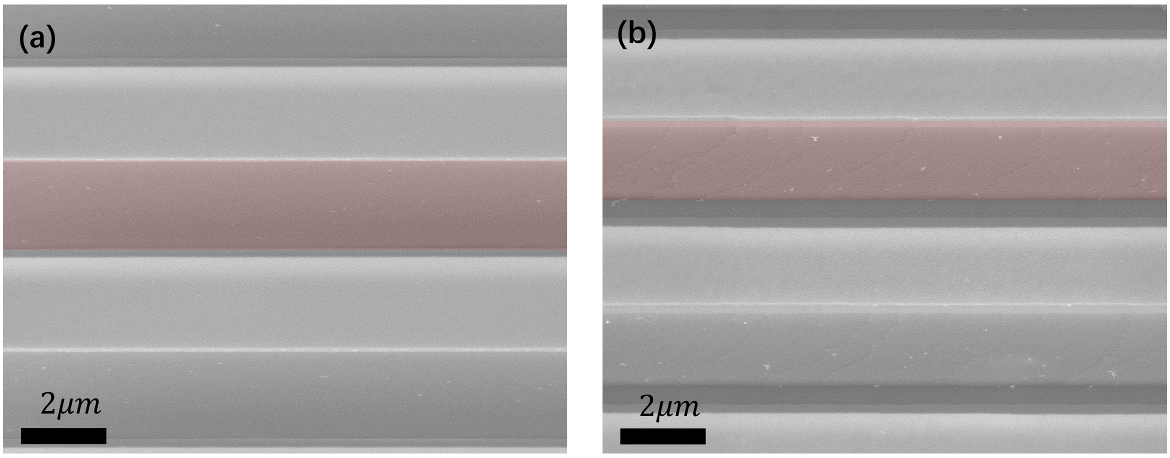

Figure 2.19: (a) smooth (111) Si facet in red with precise alignment, (b) rough (111) Si face covered by red region with misalignment.

Reference

[1] J. R. Hook and H. E. Hall, *Solid state physics*, vol. 30. John Wiley & Sons, 1995.

[2] M. Fox, "Optical properties of solids." American Association of Physics Teachers, 2002.

[3] F. Scholz, *Compound Semiconductors: Physics, Technology, and Device Concepts*. CRC Press, 2017.

[4] G. H. Wannier, "The structure of electronic excitation levels in insulating crystals," *Phys. Rev.*, vol. 52, no. 3, p. 191, 1937.

[5] W. Y. Liang, "Excitons," *Phys. Educ.*, vol. 5, no. 4, p. 226, 1970.

[6] M. A. Reshchikov and H. Morkoç, "Luminescence properties of defects in GaN," *J. Appl. Phys.*, vol. 97, no. 6, pp. 5–19, 2005.

[7] R. N. Hall, "Electron-hole recombination in germanium," *Phys. Rev.*, vol. 87, no. 2, p. 387, 1952.

[8] W. Shockley and W. T. Read Jr, "Statistics of the recombinations of holes and electrons," *Phys. Rev.*, vol. 87, no. 5, p. 835, 1952.

[9] J. Iveland, L. Martinelli, J. Peretti, J. S. Speck, and C. Weisbuch, "Direct measurement of Auger electrons emitted from a semiconductor light-emitting diode under electrical injection: identification of the dominant mechanism for efficiency droop," *Phys. Rev. Lett.*, vol. 110, no. 17, p. 177406, 2013.

[10] T. Lei, T. D. Moustakas, R. J. Graham, Y. He, and S. J. Berkowitz, "Epitaxial growth and characterization of zinc-blende gallium nitride on (001) silicon," *J. Appl. Phys.*, vol. 71, no. 10, pp. 4933–4943, 1992.

[11] D. Gerthsen, B. Neubauer, C. Dieker, R. Lantier, A. Rizzi, and H. Lüth, "Molecular beam epitaxy (MBE) growth and structural properties of GaN and AlN on 3C-SiC (0 0 1) substrates," *J. Cryst. Growth*, vol. 200, no. 3–4, pp. 353–361, 1999.

[12] V. K. Lazarov, J. Zimmerman, S. H. Cheung, L. Li, M. Weinert, and M. Gajdardziska-Josifovska, “Selected growth of cubic and hexagonal GaN epitaxial films on polar MgO (111),” *Phys. Rev. Lett.*, vol. 94, no. 21, p. 216101, 2005.

[13] M. E. Lin, G. Xue, G. L. Zhou, J. E. Greene, and H. Morkoc, “p-type zinc-blende GaN on GaAs substrates,” *Appl. Phys. Lett.*, vol. 63, no. 7, pp. 932–933, 1993.

[14] H. VOLLSTÄDT, E. ITO, M. AKAISHI, S. AKIMOTO, and O. FUKUNAGA, “High pressure synthesis of rocksalt type of AlN,” *Proc. Japan Acad. Ser. B*, vol. 66, no. 1, pp. 7–9, 1990.

[15] H. Xia, Q. Xia, and A. L. Ruoff, “High-pressure structure of gallium nitride: Wurtzite-to-rocksalt phase transition,” *Phys. Rev. B*, vol. 47, no. 19, p. 12925, 1993.

[16] M. Ueno, M. Yoshida, A. Onodera, O. Shimomura, and K. Takemura, “Stability of the wurtzite-type structure under high pressure: GaN and InN,” *Phys. Rev. B*, vol. 49, no. 1, p. 14, 1994.

[17] I. Vurgaftman, J. áR Meyer, and L. áR Ram-Mohan, “Band parameters for III–V compound semiconductors and their alloys,” *J. Appl. Phys.*, vol. 89, no. 11, pp. 5815–5875, 2001.

[18] H Morkoç, “Handbook of nitride semiconductors and devices; v.1. Materials properties, physics and growth.,” *Scitech B. News*, 2008.

[19] G. R. (Gautam R. . Desiraju, *Crystal engineering : a textbook*. New Jersey: World Scientific, 2011.

[20] T. Hanada, “Basic properties of ZnO, GaN, and related materials,” in *Oxide and nitride semiconductors*, Springer, 2009, pp. 1–19.

[21] D. Chandrasekhar, D. J. Smith, S. Strite, M. E. Lin, and H. Morkoç, “Characterization of Group III-nitride semiconductors by high-resolution electron microscopy,” *J. Cryst. Growth*, vol. 152, no. 3, pp. 135–142, 1995.

[22] A. Trampert, O. Brandt, H. Yang, and K. H. Ploog, “Direct observation of the initial

nucleation and epitaxial growth of metastable cubic GaN on (001) GaAs," *Appl. Phys. Lett.*, vol. 70, no. 5, pp. 583–585, 1997.

[23] S. A. Church *et al.*, "Photoluminescence efficiency of zincblende InGaN/GaN quantum wells," *J. Appl. Phys.*, vol. 129, no. 17, p. 175702, 2021.

[24] C. J. M. Stark, T. Detchprohm, S. C. Lee, Y.-B. Jiang, S. R. J. Brueck, and C. Wetzel, "Green cubic GaInN/GaN light-emitting diode on microstructured silicon (100)," *Appl. Phys. Lett.*, vol. 103, no. 23, p. 232107, 2013.

[25] N. Das, *Advances in Optical Communication*. BoD–Books on Demand, 2014.

[26] M. Planck, "On the law of distribution of energy in the normal spectrum," *Ann. Phys.*, vol. 4, no. 553, p. 1, 1901.

[27] D. K. Gaskill, C. D. Brandt, and R. J. Nemanich, "III-Nitride, SiC and Diamond Materials for Electronic Devices. Symposium Held April 8-12 1996, San Francisco, California, USA Volume 423.," MATERIALS RESEARCH SOCIETY PITTSBURGH PA, 1996.

[28] J. S. Blakemore, "Semiconducting and other major properties of gallium arsenide," *J. Appl. Phys.*, vol. 53, no. 10, pp. R123–R181, 1982.

[29] S. Porowski, "Growth and properties of single crystalline GaN substrates and homoepitaxial layers," *Mater. Sci. Eng. B*, vol. 44, no. 1–3, pp. 407–413, 1997.

[30] D. R. Lide, *CRC handbook of chemistry and physics: a ready-reference book of chemical and physical data*. CRC press, 1995.

[31] S. M. Sze and K. K. Ng, *Physics of semiconductor devices*. John wiley & sons, 2006.

[32] P. Norton, T. Braggins, and H. Levinstein, "Impurity and lattice scattering parameters as determined from Hall and mobility analysis in n-type silicon," *Phys. Rev. B*, vol. 8, no. 12, p. 5632, 1973.

[33] A. S. Kyuregyan and S. N. Yurkov, "Room-temperature avalanche breakdown voltages

of p-n# 3 junctions made of Si, Ge, SiC, GaAs, GaP, and InP," *Sov. Physics--Semiconductors(English Transl.*, vol. 23, no. 10, pp. 1126–1131, 1989.

[34] C. J. Glassbrenner and G. A. Slack, "Thermal conductivity of silicon and germanium from 3 K to the melting point," *Phys. Rev.*, vol. 134, no. 4A, p. A1058, 1964.

[35] D. C. Look and J. R. Sizelove, "Predicted maximum mobility in bulk GaN," *Appl. Phys. Lett.*, vol. 79, no. 8, pp. 1133–1135, 2001.

[36] H. Morkoç, *Handbook of nitride semiconductors and devices, Materials Properties, Physics and Growth*, vol. 1. John Wiley & Sons, 2009.

[37] J. Marini, J. Leathersich, I. Mahaboob, J. Bulmer, N. Newman, and F. S. Shahedipour-Sandvik, "MOCVD growth of N-polar GaN on on-axis sapphire substrate: Impact of AlN nucleation layer on GaN surface hillock density," *J. Cryst. Growth*, vol. 442, pp. 25–30, 2016.

[38] A. E. Romanov, T. J. Baker, S. Nakamura, J. S. Speck, and E. U. Group, "Strain-induced polarization in wurtzite III-nitride semipolar layers," *J. Appl. Phys.*, vol. 100, no. 2, p. 23522, 2006.

[39] J. E. Northrup, "GaN and InGaN (11 2_ 2) surfaces: Group-III adlayers and indium incorporation," *Appl. Phys. Lett.*, vol. 95, no. 13, p. 133107, 2009.

[40] J. Neugebauer and C. G. Van de Walle, "Gallium vacancies and the yellow luminescence in GaN," *Appl. Phys. Lett.*, vol. 69, no. 4, pp. 503–505, 1996.

[41] S. Ito *et al.*, "Nature of yellow luminescence band in GaN grown on Si substrate," *Jpn. J. Appl. Phys.*, vol. 53, no. 11S, p. 11RC02, 2014.

[42] J. W. Matthews and A. E. Blakeslee, "Defects in epitaxial multilayers: I. Misfit dislocations," *J. Cryst. Growth*, vol. 27, pp. 118–125, 1974.

[43] A. Tyagi *et al.*, "Partial strain relaxation via misfit dislocation generation at heterointerfaces in (al, in) gan epitaxial layers grown on semipolar (11 2¯ 2) gan free standing substrates," *Appl. Phys. Lett.*, vol. 95, no. 25, p. 251905, 2009.

[44] E. C. Young *et al.*, “Lattice tilt and misfit dislocations in (1122) semipolar GaN heteroepitaxy,” *Appl. Phys. express*, vol. 3, no. 1, p. 11004, 2010.

[45] D. N. Zakharov, Z. Liliental-Weber, B. Wagner, Z. J. Reitmeier, E. A. Preble, and R. F. Davis, “Structural TEM study of nonpolar a-plane gallium nitride grown on (11 2¯ 0) 4 H-SiC by organometallic vapor phase epitaxy,” *Phys. Rev. B*, vol. 71, no. 23, p. 235334, 2005.

[46] J. E. Northrup, “Theory of the (12_10) prismatic stacking fault in GaN,” *Appl. Phys. Lett.*, vol. 72, no. 18, pp. 2316–2318, 1998.

[47] S. Y. Karpov, R. A. Talalaev, E. V Yakovlev, and Y. N. Makarov, “GaN and Related Alloys,” in *MRS Symposia Proceedings*, 2001, no. 639, pp. G3-18.

[48] J. E. Northrup, “Impact of hydrogen on indium incorporation at m-plane and c-plane In 0.25 Ga 0.75 N surfaces: First-principles calculations,” *Phys. Rev. B*, vol. 79, no. 4, p. 41306, 2009.

[49] A. Strittmatter *et al.*, “Semi-polar nitride surfaces and heterostructures,” *Phys. status solidi*, vol. 248, no. 3, pp. 561–573, 2011.

[50] M. V Durnev, A. V Omelchenko, E. V Yakovlev, I. Y. Evstratov, and S. Y. Karpov, “Indium incorporation and optical transitions in InGaN bulk materials and quantum wells with arbitrary polarity,” *Appl. Phys. Lett.*, vol. 97, no. 5, p. 51904, 2010.

[51] Y. Zhao *et al.*, “Indium incorporation and emission properties of nonpolar and semipolar InGaN quantum wells,” *Appl. Phys. Lett.*, vol. 100, no. 20, p. 201108, 2012.

[52] S. Guha and N. A. Bojarczuk, “Ultraviolet and violet GaN light emitting diodes on silicon,” *Appl. Phys. Lett.*, vol. 72, no. 4, pp. 415–417, 1998.

[53] H. Lahreche, P. Vennegues, B. Beaumont, and P. Gibart, “Growth of high-quality GaN by low-pressure metal-organic vapour phase epitaxy (LP-MOVPE) from 3D islands and lateral overgrowth,” *J. Cryst. Growth*, vol. 205, no. 3, pp. 245–252, 1999.

[54] S. Raghavan and J. M. Redwing, “Growth stresses and cracking in GaN films on (111)

Si grown by metal-organic chemical-vapor deposition. I. AlN buffer layers," *J. Appl. Phys.*, vol. 98, no. 2, p. 23514, 2005.

[55] S. Raghavan, X. Weng, E. Dickey, and J. M. Redwing, "Correlation of growth stress and structural evolution during metalorganic chemical vapor deposition of GaN on (111) Si," *Appl. Phys. Lett.*, vol. 88, no. 4, p. 41904, 2006.

[56] Y. Honda, Y. Kuroiwa, M. Yamaguchi, and N. Sawaki, "Growth of GaN free from cracks on a (111) Si substrate by selective metalorganic vapor-phase epitaxy," *Appl. Phys. Lett.*, vol. 80, no. 2, pp. 222–224, 2002.

[57] B. Zhang, H. Liang, Y. Wang, Z. Feng, K. W. Ng, and K. M. Lau, "High-performance III-nitride blue LEDs grown and fabricated on patterned Si substrates," *J. Cryst. Growth*, vol. 298, pp. 725–730, 2007.

[58] P. Kung *et al.*, "High quality AIN and GaN epilayers grown on (00 · 1) sapphire,(100), and (111) silicon substrates," *Appl. Phys. Lett.*, vol. 66, no. 22, pp. 2958–2960, 1995.

[59] J. Boo, S. Lee, Y. Kim, J. T. Park, K. Yu, and Y. Kim, "Growth of AlN and GaN thin films on Si (100) using new single molecular precursors by MOCVD method," *Phys. status solidi*, vol. 176, no. 1, pp. 711–717, 1999.

[60] X. Zhang, S.-J. Chua, P. Li, K.-B. Chong, and Z.-C. Feng, "Enhanced optical emission from GaN films grown on a silicon substrate," *Appl. Phys. Lett.*, vol. 74, no. 14, pp. 1984–1986, 1999.

[61] J. Wan, R. Venugopal, M. R. Melloch, H. M. Liaw, and W. J. Rummel, "Growth of crack-free hexagonal GaN films on Si (100)," *Appl. Phys. Lett.*, vol. 79, no. 10, pp. 1459–1461, 2001.

[62] E. Calleja *et al.*, "Growth of III-nitrides on Si (1 1 1) by molecular beam epitaxy Doping, optical, and electrical properties," *J. Cryst. Growth*, vol. 201, pp. 296–317, 1999.

[63] H. Ishikawa, K. Yamamoto, T. Egawa, T. Soga, T. Jimbo, and M. Umeno, "Thermal

stability of GaN on (1 1 1) Si substrate," *J. Cryst. Growth*, vol. 189, pp. 178–182, 1998.

[64] A. Krost and A. Dadgar, "GaN-based optoelectronics on silicon substrates," *Mater. Sci. Eng. B*, vol. 93, no. 1–3, pp. 77–84, 2002.

[65] R. Ravash *et al.*, "Impact of AlN seeding layer growth rate in MOVPE growth of semi-polar gallium nitride structures on high index silicon," *Phys. status solidi*, vol. 248, no. 3, pp. 594–599, 2011.

[66] R. Ravash, J. Blaesing, A. Dadgar, and A. Krost, "Semipolar single component GaN on planar high index Si (11h) substrates," *Appl. Phys. Lett.*, vol. 97, no. 14, p. 142102, 2010.

[67] M. Tilli, M. Paulasto-Kröckel, M. Petzold, H. Theuss, T. Motooka, and V. Lindroos, *Handbook of silicon based MEMS materials and technologies*. Elsevier, 2020.

[68] T. Tanikawa, T. Hikosaka, Y. Honda, M. Yamaguchi, and N. Sawaki, "Growth of semi-polar (11-22) GaN on a (113) Si substrate by selective MOVPE," *Phys. status solidi c*, vol. 5, no. 9, pp. 2966–2968, 2008.

[69] M. Yang, H. S. Ahn, T. Tanikawa, Y. Honda, M. Yamaguchi, and N. Sawaki, "Maskless selective growth of semi-polar $(1\ 1\bar{2}\,2)$ GaN on Si (3 1 1) substrate by metal organic vapor phase epitaxy," *J. Cryst. Growth*, vol. 311, no. 10, pp. 2914–2918, 2009, doi: 10.1016/j.jcrysgro.2009.01.064.

[70] M. Pristovsek *et al.*, "Low defect large area semi-polar (1122) GaN grown on patterned (113) silicon," *Phys. Status Solidi Basic Res.*, vol. 252, no. 5, pp. 1104–1108, 2015, doi: 10.1002/pssb.201451591.

Chapter 3

Equipment

In order to carry out the research project in this thesis, a number of technical equipment are employed throughout template/device fabrication, epitaxial growth and corresponding characterisation. It is essential to fully understand these techniques in an operational and a functional perspective. In this chapter, equipment is divided into three groups and described in detail: template fabrication equipment, epitaxy equipment and characterisation equipment.

3.1 Fabrication Equipment

This section consists of the fabrication equipment which is employed as pattern transferring, etching and deposition approaches to fabricate patterned silicon substrates, including plasma enhance chemical vapour deposition, E-beam physicial vapour deposition, mask aligner and reactive-ion etching.

3.1.1 Dielectric Thin Film Deposition

Plasma Enhanced Chemical Vapour Deposition (PECVD) is an approach to perform a dielectric thin film deposition such as Si_xN_y or SiO_2 at lower temperatures compared with standard chemical vapour deposition (CVD). As shown in Figure 3.1, during the PECVD process, reactant gases are introduced between parallel electrodes, a grounded electrode on the sample stage and a radio frequency (RF) energized electrode on the top, exciting the reactant gases into plasmas via capacitive coupling between the electrodes. Such plasmas contain ionized atoms or molecules bombarded onto the sample surface, which is heated up to 300 ^{o}C, forming required dielectric films by chemical reaction. PECVD technique provides a high-quality dielectric film at a lower temperature (Standard CVD with 800 ^{o}C) and avoids the damages for the devices.

Plasma-Therm 790 series PECVD system is adopted in this work for SiO_2 film deposition. The sample stage and sidewall are heated up to 300 ^{o}C and 60 ^{o}C respectively. SiH_4, NH_3 and

N_2 are employed as reactant gases and flow rates are 160 sccm, 900 sccm and 240 sccm respectively. Under 900mTorr of reactor pressure and 25W RF power, the deposition rate is around 40 nm/min. In this work, a 120nm thick of SiO_2 film is deposited for subsequent patterning fabrication.

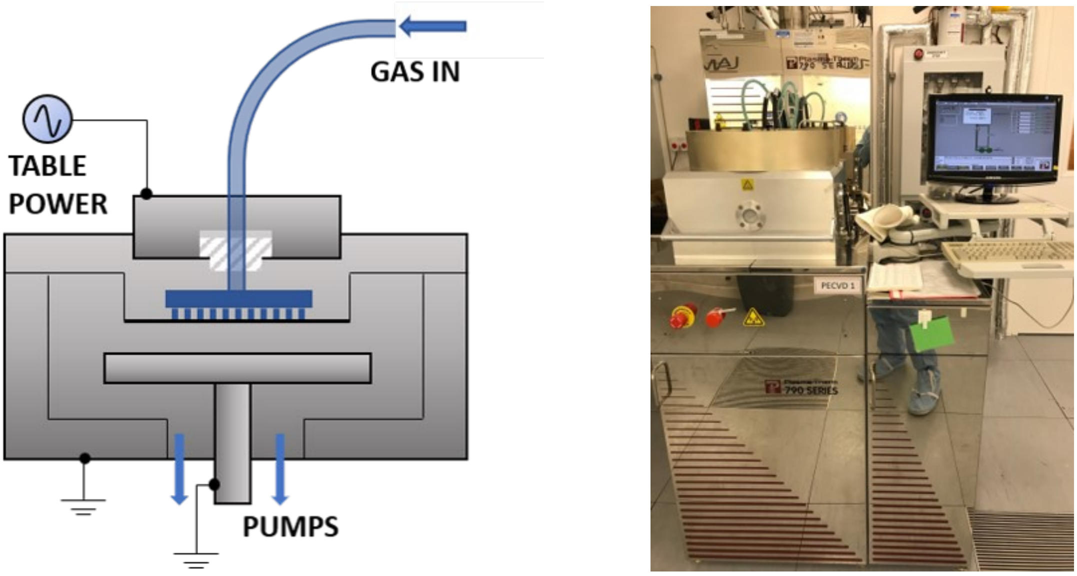

Figure 3.1: Plasma-Therm 790 series PECVD.

3.1.2 E-Beam Physical Vapor Deposition (EBPVD) System

E-beam physical vapour deposition (EBPVD) is one type of physical vapour deposition (PVD) in which to deposit metallic thin films, dielectric materials and optical coatings. As shown in Figure 3.2, during the EBPVD process, a crucible containing the deposition material is placed inside the ingot with a positive potential relative to the tungsten filament. With a high voltage applied between the filament and the ground under a high vacuum condition (at least 7.5×10^{-5} Torr), the liberated electrons from an electron gun are accelerated and steered by a strong magnetic field toward to the crucible. The energy of electron beams is transferred to the material to be deposited, leading to evaporation or sublimation of the material and further depositing onto the sample.

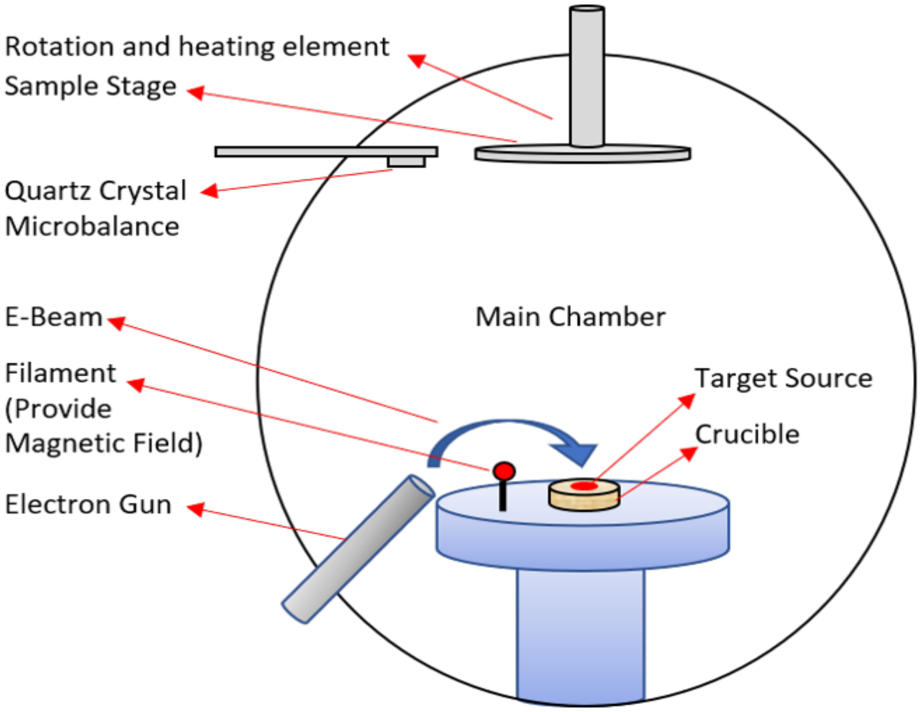

Figure 3.2: Schematics of e-beam deposition.

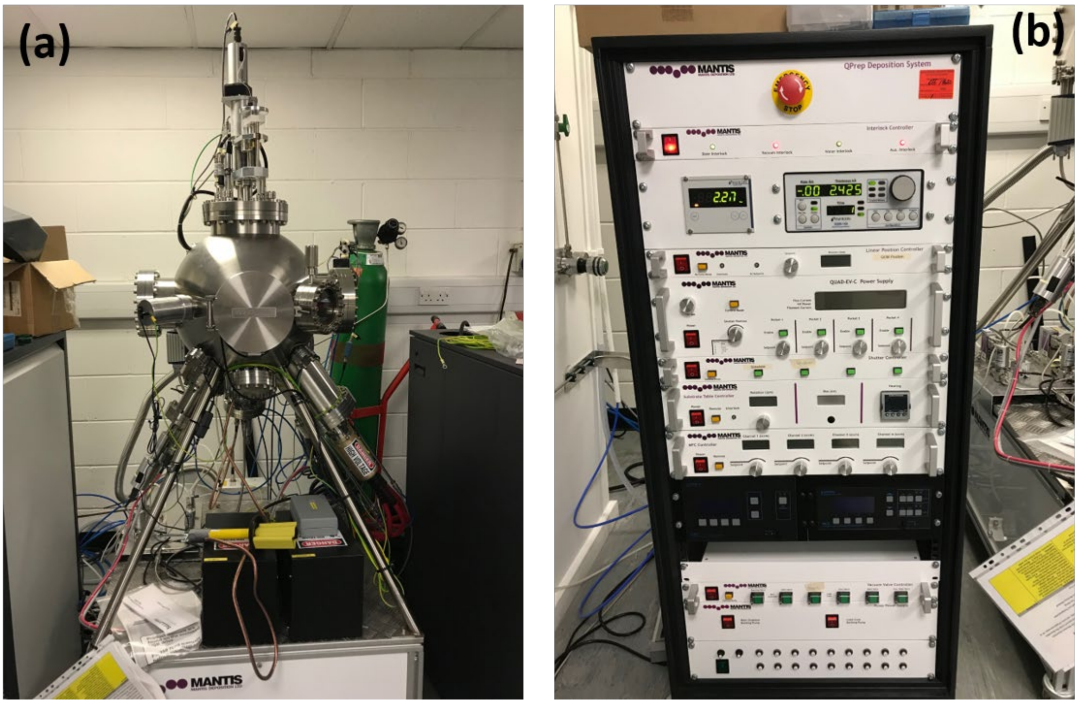

Figure 3.3: Mantis e-beam system (a): main chamber; (b): control panel.

In this work, Mantis EBPVD is employed to form a selective area SiO_2 deposition as shown in Figure 3.3. In order to avoid the growth facet from SiO_2 deposition, a rotation angle of 17° respect to the (113) silicon substrate cut orientation is applied. The deposition is carried out at room temperature, and the high vacuum condition as low as 2×10^{-7} Torr is achieved by a turbopump system including a rotary pump as the pre-pump and a turbopump as the main pump. With a 7 mA filament current and 7.5 KV high voltage, a 10 nm SiO_2 is deposited on the patterned (113) substrate an approximate 0.5 nm/sec deposition rate is achieved and monitored by quartz crystal microbalance (QCM).

3.1.3 Photolithography

Photolithography is a typical technique for transferring geometric pattern from a pre-designed mask onto the surface of the substrate. Such process of photolithography involves wafer cleaning, photoresist coating, exposure and development.

Wafer Cleaning

A standard procedure of wafer cleaning process is carried out to remove any contaminants, dusts or particles on the surface of wafer prior to the photoresist coating. The cleaning steps include:

I. Solvent cleaning: n-butyl acetate (nBA), acetone and isopropyl alcohol (IPA).

II. Rinsing the wafer with deionized water to clean the solvent residual.

III. Blowing the wafer with clean nitrogen to remove water stains and baking process at the hot plate with 100°C is employed to de-moisturization.

Photoresist coating

In this work, a 120 nm SiO_2 layer is deposited on the top surface of (113) Si substrate as mentioned in Section 3.1.1. An adhesion promoter is required prior to the photoresist coating as naturally hydrophilic of SiO_2 will absorb water from ambient humidity. Such water layer will allow the developer to etch the interface of photoresist and SiO_2 layer, leading to undercutting or delamination of the photoresist pattern. Hexamethyldisilazane (HMDS) is employed as an adhesion promoter as shown in Figure 3.4. By applying HMDS, a hydrophilic surface can be converted to a hydrophobic state, preventing photoresist from delamination [1].

SPR-350 photoresist is used for coating by Electronic Micro Systems Spin Coater Model-4000, forming a $\sim 1\,\mu m$ uniform coating layer under 4000 RPM for 30 seconds. Then, solidified photoresist is achieved on the surface of the wafer during the subsequent soft-bake process.

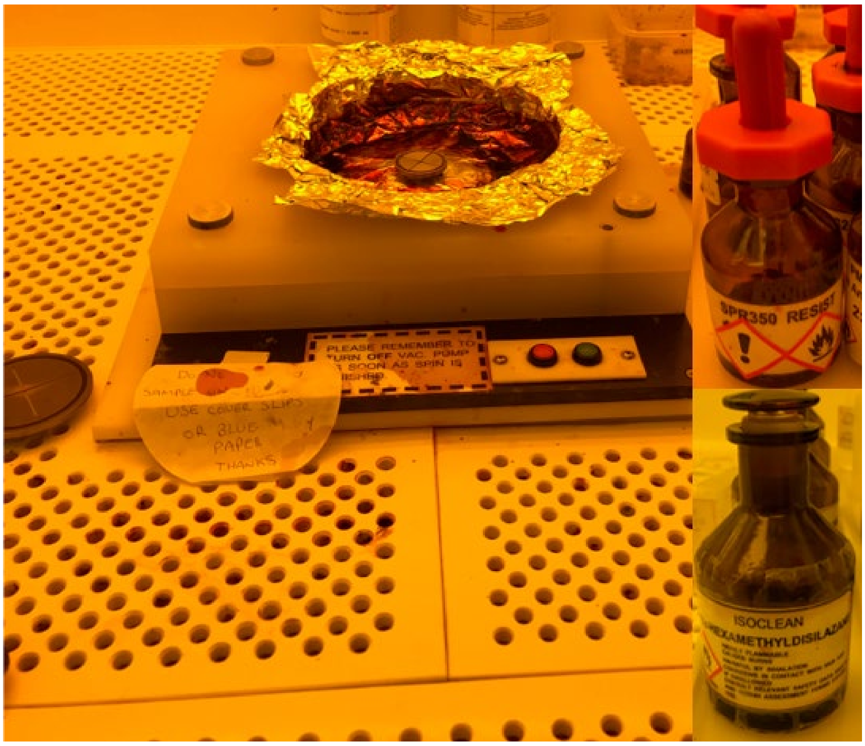

Figure 3.4: Electronic Micro Systems Spin Coater Model-4000 and inserted images are SPR-350 photoresist and Hexamethyldisilazane (HMDS).

Exposure

To prime a patterned structure resist film, Karl Suss MJB3 UV400 Mask Aligner is employed in this work as shown in Figure 3.5. The prepared sample with coated photoresist is loaded on the sample holder of mask aligner. A photomask consists of a glass or quartz plate with patterned chromium coating can contact the sample, allowing ultraviolet (UV) light to pass through the transparent area onto the resist film and block light with the opaque area. Thus, a 1:1 ratio of dimension 4 µm/4 µm stripe structures with photomask pattern is attained on the resist film. SPR-350 Photoresist is a positive type photoresist which consists of light-sensitive polymers or polymer precursors dissolved in an organic solvent. Therefore, the whole process is undertaken in the yellow room with a light filter which can prevent the pre-reaction between photoresist and short-wavelength emission. With the exposure under UV light, the positive type photoresist is decomposed and break down, increasing the solubility in the developer. While the negative type is further polymerized or cross-linked, forming a hardened coating with insolubility in the developer. The UV lamp of Karl Suss MJB3 UV400 Mask aligner is contained with 405 nm as light sources, featuring a print resolution of $0.8\ \mu m$ with optimum condition.

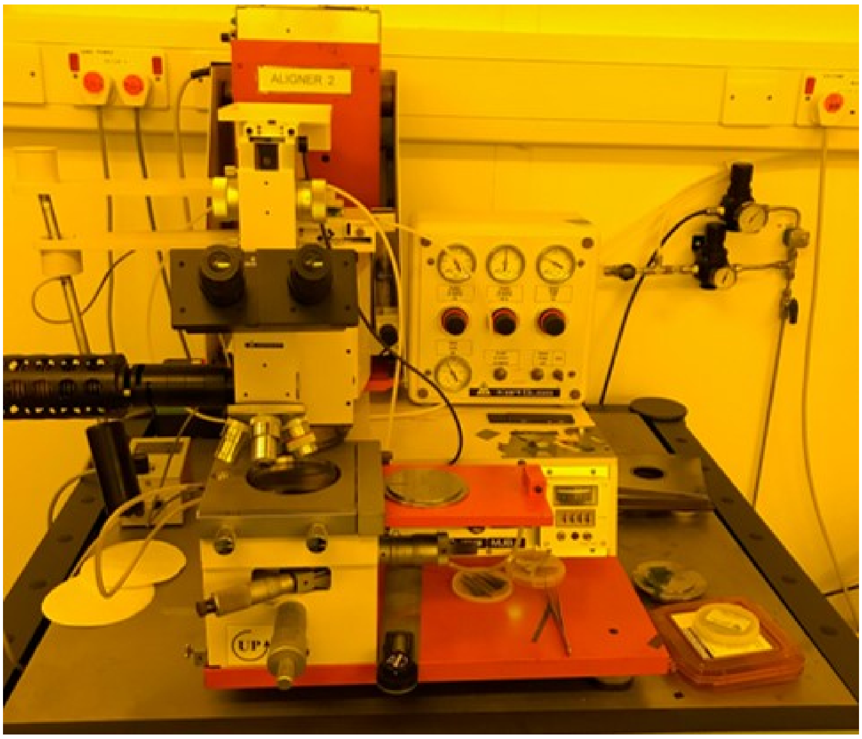

Figure 3.5: Karl Suss MJB3 UV400 mask aligner.

Developing

The developing process is either removing the exposed or unexposed area which depends on the type of employed photoresist. In this work, MF-26A developer is utilised, which is based on an aqueous solution of the metal ion free organic TetraMethylAmmoniumHydroxide (THAH), to remove the exposed area of SPR-350 photoresist [2]. The development rate depends on the temperature and the concentration of the developer. Thus, an optimised developing process performed in this work includes a room-temperature diluted developer with 2:1 ratio of DI water, and the developing time is around 70 seconds. A 4 μm photoresist stripe and 4 μm window patterned is formed on the (113) silicon substrate after the developing process.

3.1.4 Reactive-Ion Etching

Reactive-ion etching is a typical dry etching technique which provides an anisotropic etching process by mean of reactive plasmas. As shown in Figure 3.6, the reactant gases are ionized by two paralleled electrodes with RF, forming the plasmas which consist of radicals and ions and accelerating towards to the sample by the electric field. The reactive species from plasmas react with the material to form a volatile by-product and is then pumped away from the bottom of the chamber.

In this work, a Plasma-Therm Shuttlelock RIE system is employed to perform a selective area etching on SiO_2 mask. CHF_3 is used as reactant gas to generate plasmas with a 13.56 MHz RF power at 150 W. The etching process occurs at a low pressure of 35 mTorr and an estimated etching rate is 40 nm/min. In addition, sidewall passivation can enhance the anisotropy of etching as carbon polymers from reactant gases deposit on the sidewall of SiO_2 and prevents from chemical reaction. However, such sidewall polymeric passivation can lower the etching rate when it excessed a certain amount, forming grass-like oxide residues which result in poor uniformity of etching pattern. Thus, a flow rate of 5 sccm O_2 is added to remove the polymers during the etching process [3]. After RIE etching process, the SiO_2 covered by photoresist is remaining while the exposed area is etching down to silicon substrate, leaving a 4 μm SiO_2 mask and 4 μm Si substrate window patterned formed on the (113) silicon substrate.

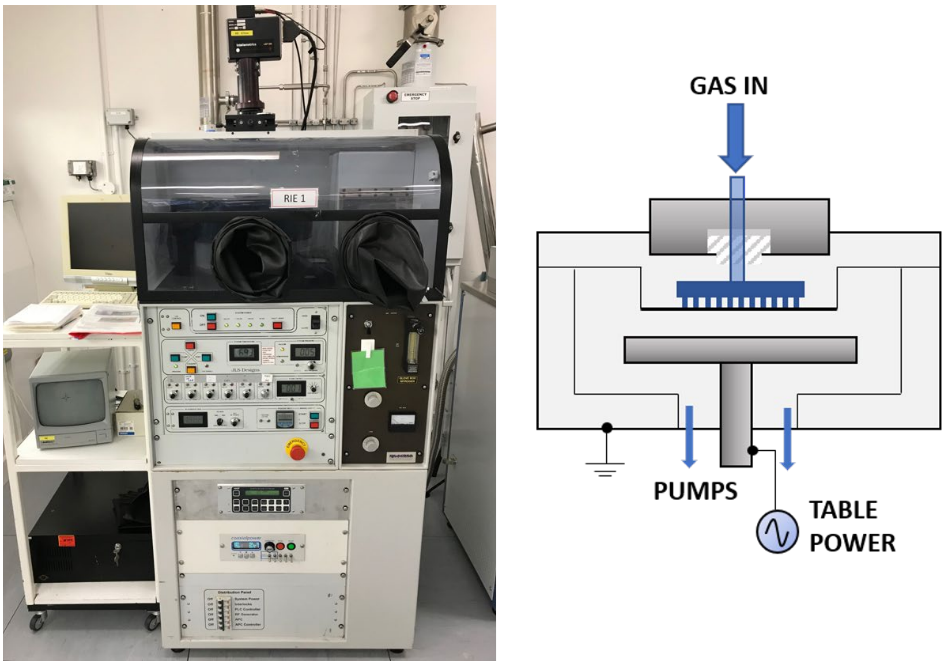

Figure 3.6: Plasma-Therm Shuttlelock Series RIE.

3.1.5 Chemical Wet etching

Potassium hydroxide (KOH) will be employed as etchant to perform the anisotropic wet etching process for patterned (113) silicon substrate. The template is immerse into a KOH solution with 25 wt%. The chemical wet etching process is taking up to 50 to 60 minutes under 30 °C thermal heating and ultrasonic bath in the initial 10 minutes in order to accelerate the etching process. As a result, two (111) Si facets including (1-11) and (-11-1) planes with inclination angle of 58° respect to the silicon substrate are formed into a trench structure.

3.2 Epitaxy Equipment

Metal Organic Vapour Phase Epitaxy (MOVPE) is used as epitaxy equipment in this project. MOVPE has a widespread application in compound semiconductors industry and research due to the ability of growing high-quality epitaxial layer with precise control of thickness and composition as well as reproducibility. MOVPE is also called as Metal Organic Chemical Vapour Deposition (MOCVD) or Organometallic Chemical Vapour Deposition (OMCVD) or Organometallic Vapour Phase Epitaxy (OMVPE). Currently, there are mainly three types of MOVPE system: high-speed rotation vertical reactor [4], planetary rotation horizontal reactor

[5] and close-coupled showerhead (CCS) reactor [6]. Two MOVPE systems are employed in this work as shown in Figure 3.7. An Aixtron $3 \times 2''$ flip-top CCS system is employed for the growth of initial AlN template. A Thomas-Swan $3 \times 2''$ vertical CCS system is used for subsequent growth of GaN and LED structures.

Figure 3.7: Images of MOVPEs (a): Aixtron 3×2” flip-top CCS reactor; (b): Thomas-Swan 3×2” vertical CCS reactor.

3.2.1 Basic Growth Principle of MOVPE

MOVPE epitaxial growth is governed by diffusion processes in which metal organic sources as precursors are transported by carrier gas under near thermodynamic equilibrium conditions [7]. After all carrier gases are introduced into the reactor, the corresponding chemical reactions proceed on the substrate surface with designed temperature. The pressure gauges and mass-flow controllers are responsible for the precise flow rates of all induced gases. A diagram of the chemical reactions involved during the epitaxial growth in MOVPE is shown in Figure 3.8.

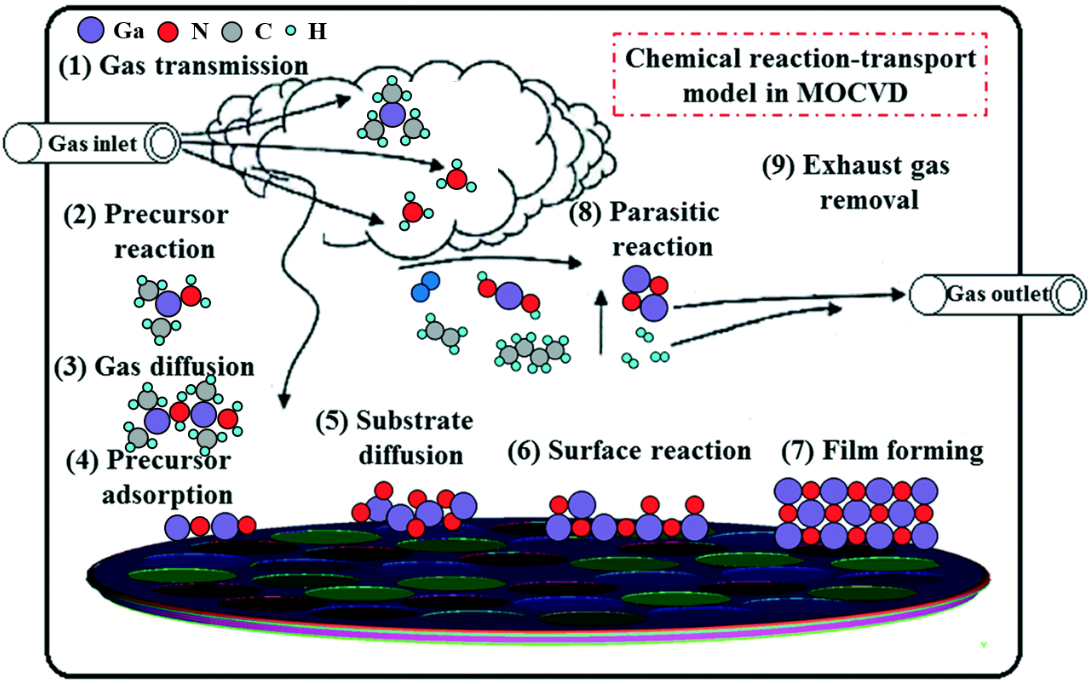

Figure 3.8: Diagram of MOVPE epitaxial growth process [7].

The organic precursor molecules are decomposed with the absence of O_2 or any halogen (pyrolysis) [7], leading to a corresponding diffusion and attachment of species onto the substrate by physisorption. Following chemical reactions with other surface species form a new epilayer by means of bounding tightly at the bottom with a growth step or nucleating at other positions to form islands [7]. Corresponding by-products from the surface reactions are exhausted out of the chamber through carrier gas. However, parasitic reactions can occur between different precursors in gas phase, leading to a reduction of incorporation efficiency. In addition, the presence of particles from the by-products on the substrate surface could impede subsequent epitaxial growth and degrade the crystal quality [7].

In the III-nitrides epitaxial growth by MOVPE technique, three organometallic compounds of group-III metals are used as group III precursors, such as Trimethylgallium (TMGa), Trimethylaluminum (TMAl) and Trimethylindium (TMIn). Ammonia (NH_3) with high-level purity is used as group V precursor. Disilane (Si_2H_6) and Bis(cyclopentadienyl)magnesium (Cp_2Mg) are used as n-type doping and p-type doping for III-nitrides respectively. The global reaction of III-nitrides epitaxial growth can be generalized as below [8]:

$$III\ R_3(gas) + V\ H_3(gas) \overset{\Delta}{\rightarrow} III\ V(solid) + 3RH_4(gas) \tag{3.1}$$

Where III and V denote the group-III and group-V elements respectively, R is the type of organic radical where the group-III element is attached, and H is hydrogen. For instance, the reaction of GaN growth is shown below [8]:

$$Ga(CH_3)_3(gas) + NH_3(gas) \overset{\Delta}{\rightarrow} GaN(solid) + 3CH_4(gas) \tag{3.2}$$

And the growth of $In_xGa_{1-x}N$ requires the additional presence of TMIn or $In(CH_3)_3$ as precursors for the chemical reaction.

3.2.2 Basic Components of an MOVPE System

Reactor

Reactor chamber of MOVPE system, where the epitaxial growth takes place, consists of in-situ monitoring system, showerhead system, susceptor system and heater system. The detailed components in the reactor are shown in Figure 3.9.

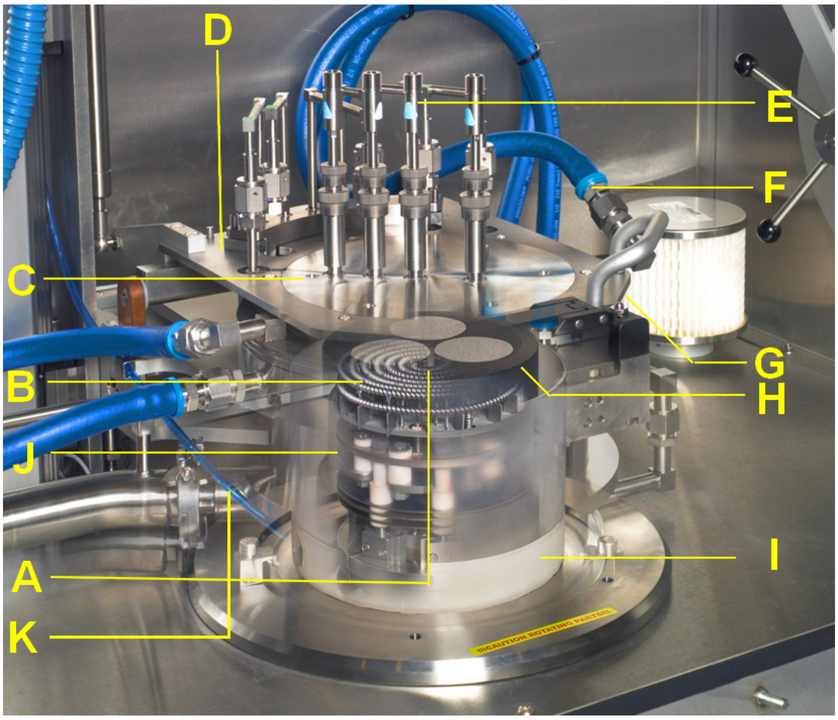

Figure 3.9: Image of elements in the reactor of MOVPE. A: thermocouple; B: tungsten heater; C: showerhead; D: reactor lid; E: optical probe; F: showerhead water cooling; G: double O-ring seal; H: susceptor; I: quartz liner; J: susceptor support; K: exhaust (Taken from [9]*).*

The in-situ monitoring system is set up on the top of reactor lid for monitoring the uniformity of temperature and growth rate of epi-layer during the growth through an Argus temperature monitoring system and a laser reflectometry monitoring system. The growth rate is calculated by the following equation:

$$Growth\ Rate = \frac{\lambda}{2n\Delta t} \tag{3.3}$$

where λ is the wavelength of the in-situ laser, Δt is the interval time between two maxima or two minima of oscillations, n is the refractive index of the epi-layer.

The showerhead is designed intrinsically for uniformity to avoid jetting or turbulence during the gas injection. Moreover, the separated injection of group-III precursors and group-V precursors could minimize the pre-reactions, such as parasitic reaction which deteriorates the crystal quality by introducing by-products [7]. A closed-cycled cooling water system is constantly cooling for the showerhead and chamber walls to avoid the damage from high temperature. A susceptor, where wafers are loaded into, is composed of graphite and coated with a thick SiC layer to prevent from corrosion during the epitaxial growth and form a good temperature uniformity. An ultra-high temperature is achieved by a double coil system with three independently controlled zones as shown in Figure 3.10. Each heating zone is individually controlled by a power supply unit (PSU), achieving a high uniformity of temperature during the growth. The reactor chamber is sealed by a double O-ring system, which maintains a constant evacuation for the intermediate area, preventing any leakage when the reactor chamber is closed.

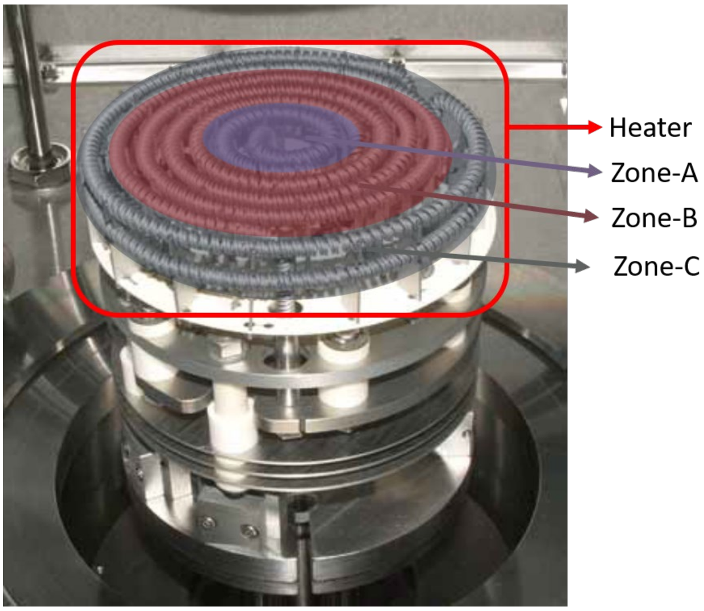

Figure 3.10: Image of heater (Modified from [9]*).*

Metal-Organic (MO) Precursor Input System

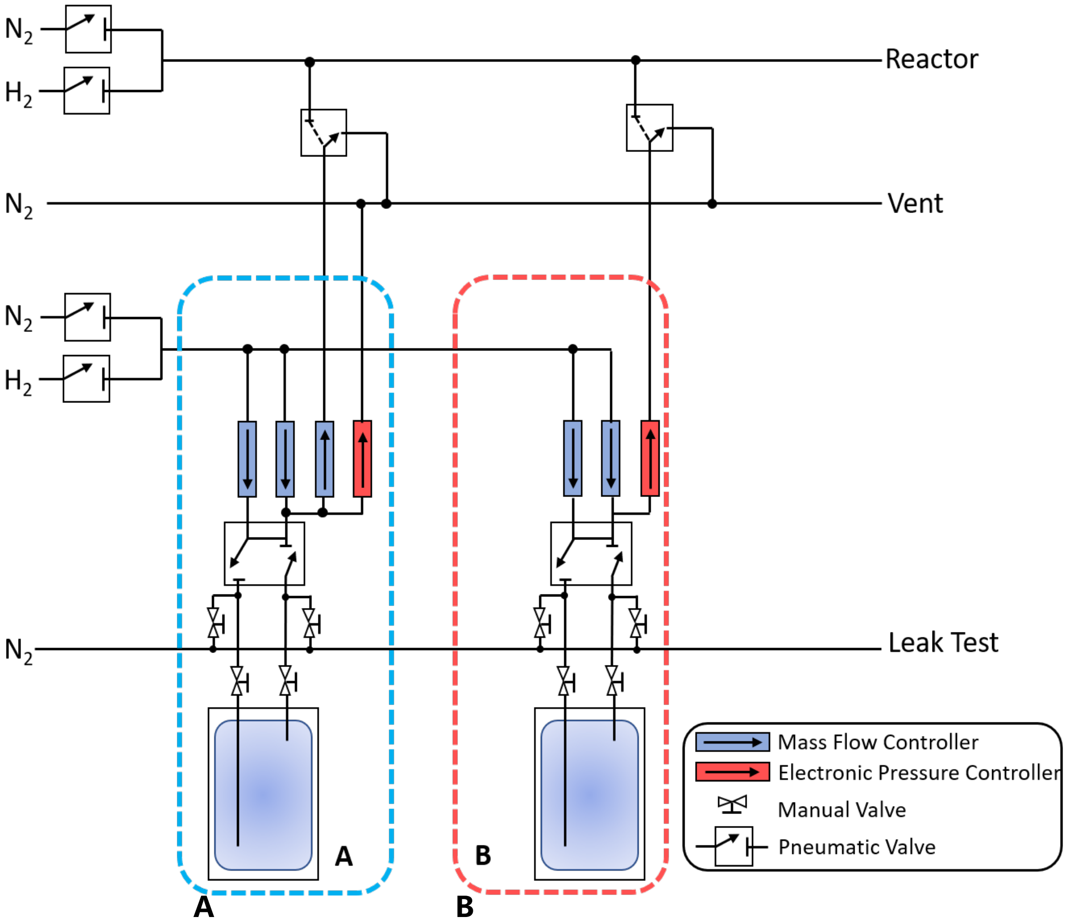

Figure 3.11: Schematics of MO precursor input system of MOVPE with A: dilution precursor line and B: standard precursor line.

A MO precursor input system contains source storage units, gas system and controller units including pressure gauge and mass flow controllers (MFCs) which provide a highly accurate flow rate injection. MO precursors in a form of either liquid or solid are typically stored in a sealed stainless-steel container which referred as “bubbler”. All bubblers are placed in temperature-controlled water or glycol bath to control the liquid-vapour or solid-vapour (TMIn and Cp_2Mg) equilibrium, providing the partial vapour pressure of the precursor in the bubbler. The schematics of MO precursor input system of MOVPE is shown in Figure 3.11.

For the standard MO precursor line, it contains two MFCs in the inlet channels which control the precursor flowrate and pusher flowrate respectively. The pusher line is responsible for balancing the upper and lower main carrier channels during the whole period when using the precursor and an electronic pressure controller (PC) to control the pressure of the bubbler. When a low flowrate is required such as TMGa for QW structure growth, a MO precursor line with a dilution gas is employed. A third MFC provides an extra carrier gas into the outlet line to dilute the precursor, obtaining a low flowrate. The actual MO precursor flowrate can be calculated by the equation below:

$$f(MO) = f_{injection} \times \frac{f_{precursor}}{f_{precursor} + f_{dilution}} \tag{3.4}$$

Where $f(MO)$ is the actual MO precursor flowrate, $f_{injection}$, $f_{precursor}$ and f_{dilute} are the flowrate of injection line, precursor line and dilution line, respectively.

The actual mole flowrate of MO precursor depends on the temperature and the pressure of bubbler which is placed in the water tank with a designed temperature. And the pressure of the bubbler is controlled by PC. Thus, an actual mole flowrate can be expressed by the equation below:

$$n(MO) = \frac{f_{MO} \times P_{partial}}{V_m \times (P_{bubbler} - P_{partial})} \tag{3.5}$$

Where $n(MO)$ is the MO mole flux with the unit of mol/min, f_{MO} is carrier gas flow rate of MO precursor, $P_{partial}$ is vapour partial pressure of the MO source, V_m is constant with a value of 22414 cm^3/mol and $P_{bubbler}$ is the pressure inside the bubbler. Vapour partial pressure of trimethyl precursor (Such as TMGa, TMAl and TMIn) is obtained following the equation below:

$$P_{partial} = 10^{a-\left(\frac{b}{T}\right)} \tag{3.6}$$

Where a and b are constants, T is the temperature of bubbler in Kelvin. However, the vapour partial pressure of bis cyclopentadienyl precursor (Cp_2Mg) is different from trimethyl precursor, and can be expressed by the equarion below:

$$P_{partial} = 10^{a-\left(\frac{b}{T}\right)-2.18\ln T} \tag{3.7}$$

Table 3-1 shows the main parameters of commonly used MO bubblers in this work[10]–[13].

Table 3-1: Parameters of MO bubblers.

Precursor	a	b	Bubbler Temperature (K)	Melting Point (˚C)
TMGa	8.07	1703	273	-15
TMAl	8.22	2134	291	15
TMIn	11.00	3204	303	88
Cp_2Mg	25.14	4198	303	176

Gas Delivery System

A typical gas delivery system of MOVPE consists of carrier gas supply system, hydride supply system and MO precursor supply system as shown in Figure 3.12. In order to prevent pre-reactions between group-V precursors and group-III precursors, hydride supply line is mixed into upper carrier line while keeping a full separation with MO precursor line until injected into the reactor chamber. Nitrogen (N_2) and hydrogen (H_2) are employed as carrier gas, and an ultra-purity is required to avoid any impurity contamination during the epitaxial growth. Thus, purifier is introduced to the MOVPE system.

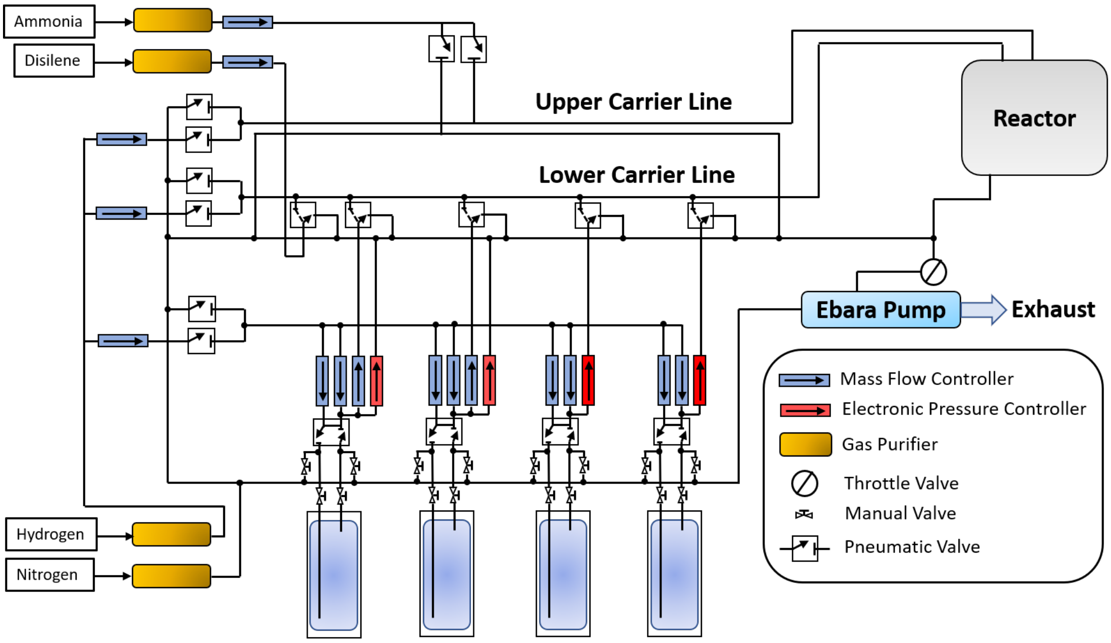

Figure 3.12: Schematics of gas delivery system of MOVPE.

Gas Purifiers

There are two kinds of gas purifiers in our MOVPE system to perform purification of carrier gas. Palladium membrane purifier and Nano-chem purifier are shown in Figure 3.13 and Figure 3.14 respectively.

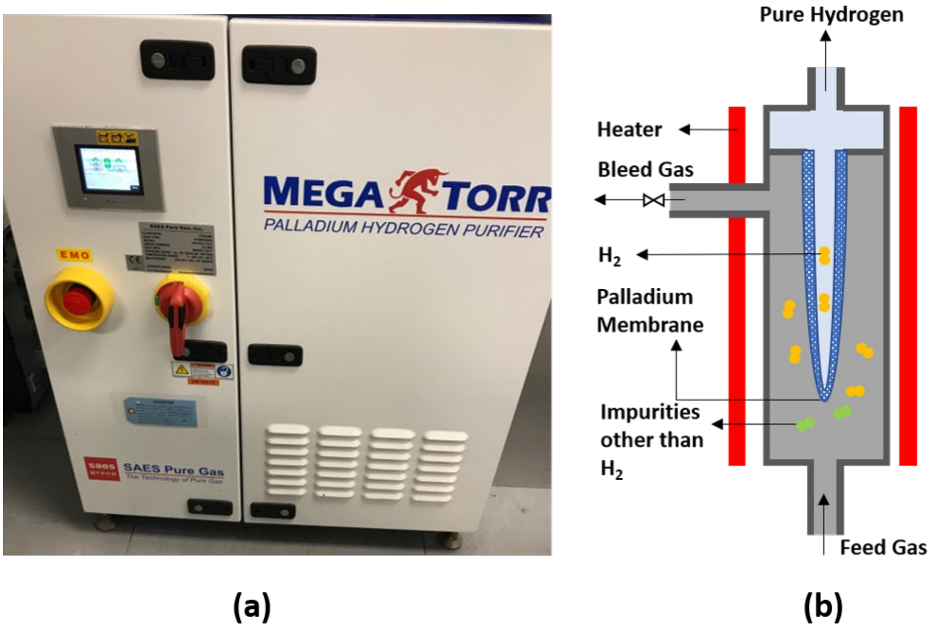

Figure 3.13: (a): image of Palladium Membrane Purifier, (b): schematics of purifier cell.

A palladium membrane purifier is used for H_2 purification. The mechanism is shown in Figure 3.13. Heating a palladium diffusion cell to around 300 °C can create a filter which only allows H_2 to pass through, leaving impurities being exhaust by bleed gas.

Figure 3.14: The image of Gate Keeper Purifier.

The Gate Keeper purifier is used to purify nitrogen or ammonia in our MOVPE system. Compare with the efficiency of H_2 purifier above, the nano-chem purifier has a lower purification rate which only partially removes water (H_2O), oxygen (O_2) or carbon dioxide (CO_2) residual by chemical reactions [14][15]. Thus, H_2 is mostly employed as the carrier gas during epitaxial growth as its high purity. Moreover, The excellent thermal conductivity of H_2 enables a fast diffusivity of precursor and excellent carbon-radical furbishing properties. However, for the QW structure growth, N_2 is used as the H_2 can enhance the indium desorption. A so-called "white ammonia" with an ultra-high impurity of 99.99999% [16] is utilized. Thus, there is no demand for purification of ammonia in this work.

3.3 Characterization Equipment

3.3.1 Nomarski Microscope

The Nomarski microscope, also called differential interference contrast (DIC) microscope or Nomarski interference contrast (NIC) microscope, is widely used to analyse the surface condition of planar semiconductor processing due to the featured function of interferometry, gaining more invisible information in form of shadowed-like and three-dimensional appearance. The basic structure and the image of Nomarski microscope are shown in Figure 3.15.

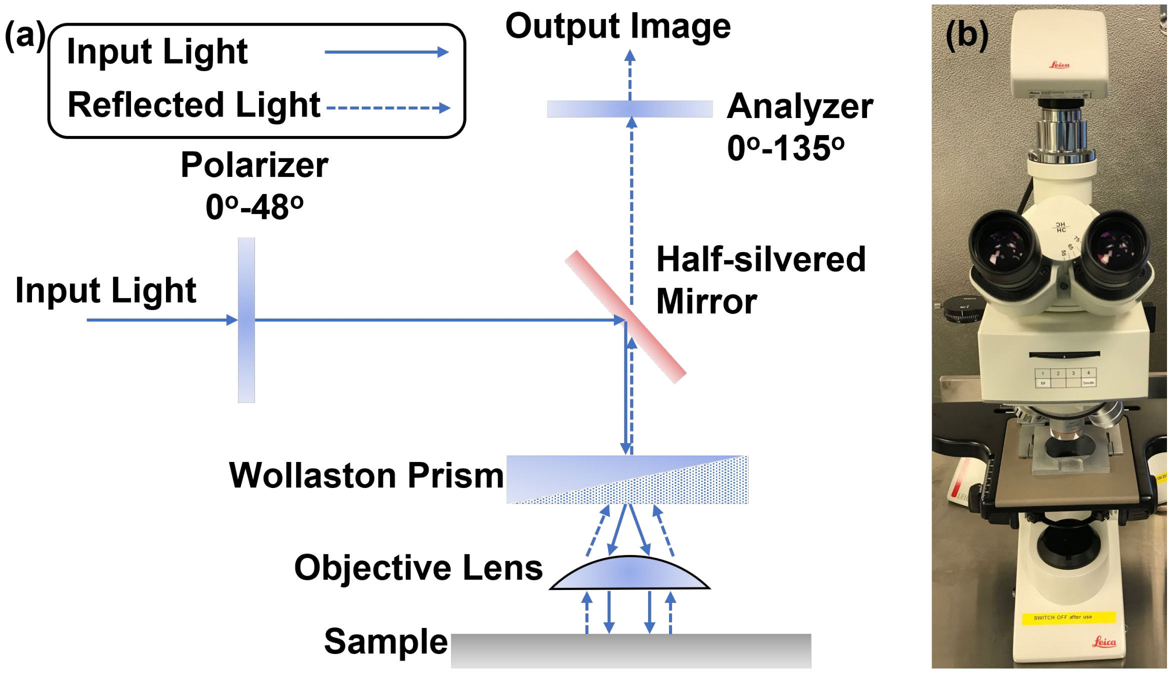

Figure 3.15: The (a): schematics of light route, (b): image of Leica DMC4500 microscope.

A rotating polarizer is inserted after a white light source to produce the polarized beam. After the polarized beam being reflected into Wollaston prism by a semi-transparent mirror, two orthogonally polarized beams which are sheared with respect to one another are generated and projected onto the sample surface. Then two beams are reflected from the sample surface and recombined by Wollaston prism. As a result, two coherent beams with different polarization directions are interfering with each other, forming a different brightness as the variation of the thickness or refractive index results in different optical path lengths [17].

3.3.2 Scanning Electron Microscope-Cathodoluminescence (SEM-CL)

Scanning electron microscope (SEM) is an indispensable kit for the characterization of nano- or micro-structures involved in this work. Compared with the conventional optical microscope, the visible light source limits the development whereas electron beam has much shorter wavelengths, enabling better resolution of the image. The diagram and the photo of the SEM are shown in Figure 3.16. The SEM measurement operates under a high vacuum condition (typically under 5×10^{-5} mbar) to minimize the electron scattering. Electrons are produced by a field emission gun (FEG) and accelerated under a high voltage level up to 30kV. Then electron beams pass through a combination of magnetic condensers and apertures, forming a focused electron beam onto the sample surface. The scan coils control the position of the electron beam and allow the beam to scan over the sample surface, collecting information from the signals of electron-sample interaction by appropriate detectors. A Raith 150 electron-beam lithography (EBL) with reconfiguration is employed in this work.

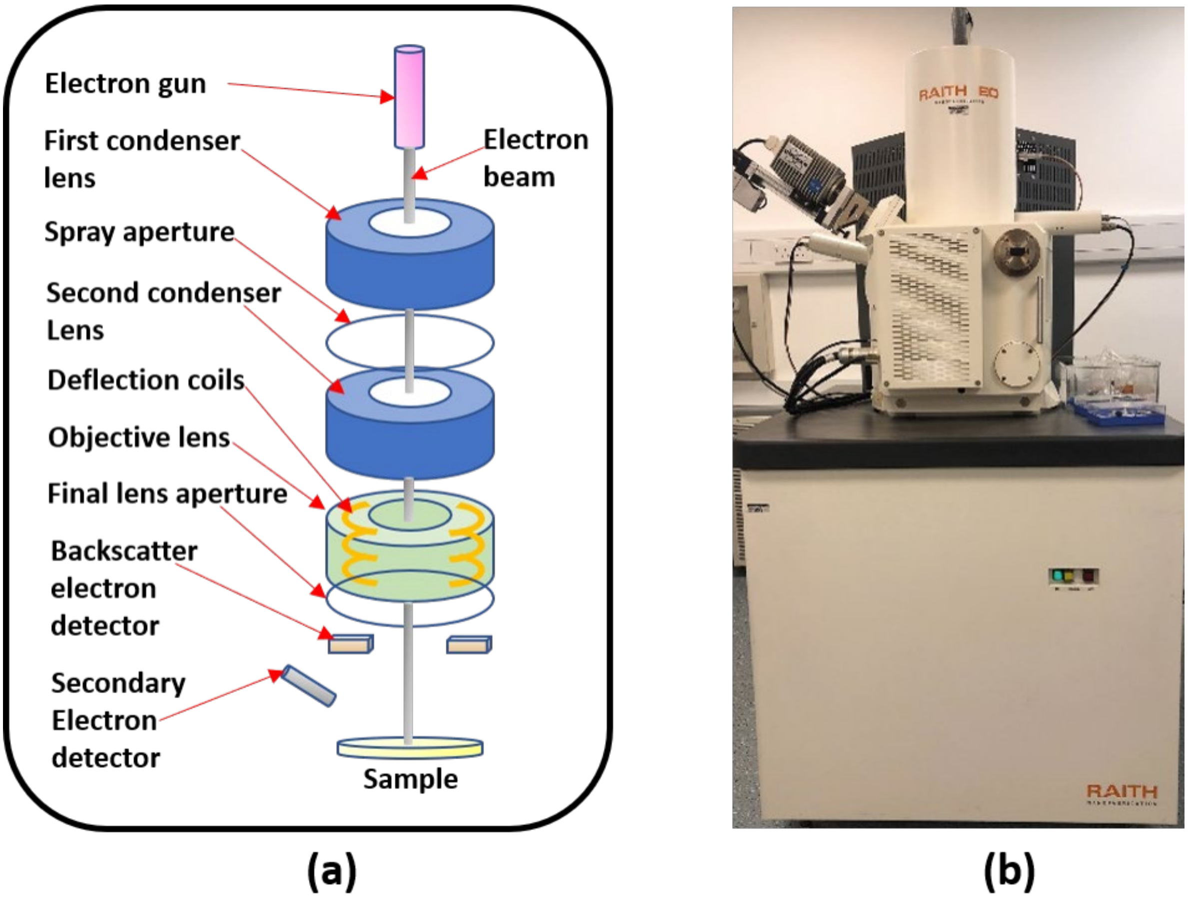

Figure 3.16: The (a): Diagram of Raith SEM, (b): photo of Raith SEM.

Figure 3.17 shows the signals produced from sample-electron interaction. When the high-energy beam of electrons interacts with the sample, a series of signals are produced by electron converting with different mechanisms. Among those signals, secondary electrons, backscattered electrons, characteristic X-rays and cathodoluminescence are commonly collected as information elements for characterisation [18]. Secondary electrons (SE) are the primary signals for revealing the surface topography and morphology of the sample as the low energy with highly localized impact point, leading to a high resolution down to 1 nm. Backscattered electrons (BSE) are used to illustrate contrasts in composition of multiphase samples as the scattering is typically dictated by the size of the nucleus. Characteristic X-ray is normally generated by the inelastic collisions between the incident electrons with electrons from the inner shell of atoms which excites electrons to high energy outer shell. When the excited electrons return to the low energy state, X-rays are outputted with a fixed wavelength corresponds to individual element. Thus, the elemental composition can be identified by energy-dispersive X-ray (EDX) through corresponding characteristic X-rays.

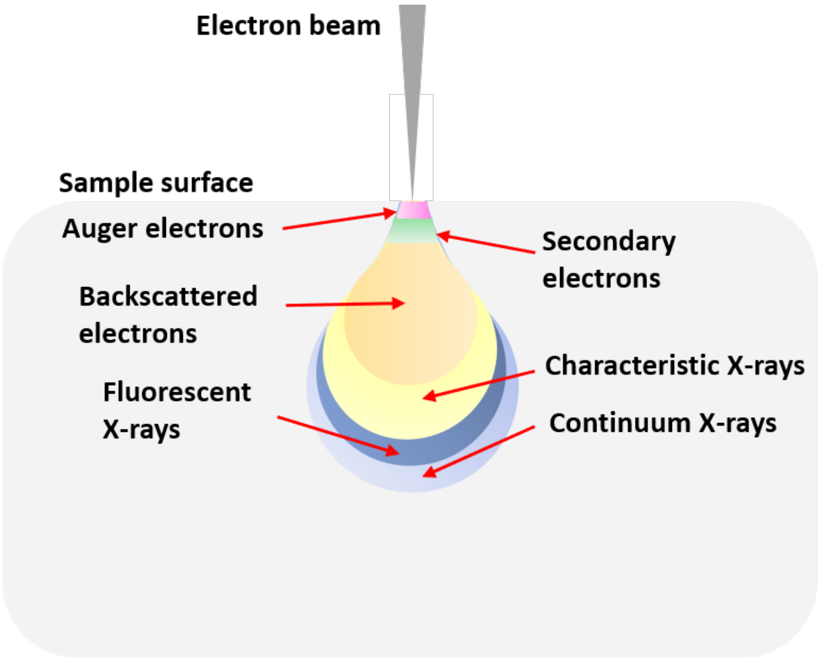

Figure 3.17: Schematic of electron beam interaction.

Cathodoluminescence is produced in a form of light emission which can be employed as a primary signal in CL measurement. The mechanism is similar with PL measurement but using a high-energy electron beam as excitation source, which has much larger energies compared to the excitation sources in any laser-based PL system. Thus, CL measurement can cover the characterization with a wide range of spectrum emission. The CL system in this work is attached to an FEI Quanta 250 SEM system and the detector is a 1600-channel electron multiplying charge-coupled device. The CL measurement is a collaboration work with the University of Strathclyde.

3.3.3 High-Resolution X-Ray Diffraction

High-resolution X-ray diffraction (HR-XRD) is a non-destructive analysis technique for crystalline structured materials. The structural parameters of semiconductor films can be revealed and quantified in terms of crystal quality, alloy composition, layer thickness and strain state.

The mechanism of XRD can be described by Bragg's law as shown in Figure 3.18. Atoms in a crystalline material exhibit in a periodic array of coherent scatters which can be considered as a 3D diffraction grating. Thus, incident X-ray would be scattered by the electron cloud surrounding atoms in each lattice planes. Due to that the wavelength of X-rays is similar to the distance of crystal interplanar (~1 Å), constructive interference occur at specific angles when they are satisfied with Bragg's law:

$$2d\sin\theta = n\lambda \tag{3.8}$$

Where d is the interplanar distance, θ is the incident angle of X-rays, n is diffraction order and λ is the wavelength of X-ray [19].

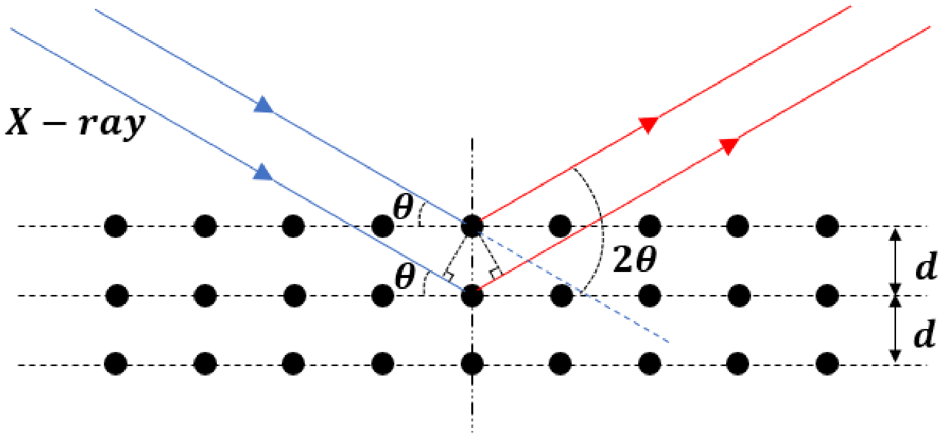

Figure 3.18: Schematics of Bragg's law applied in X-ray diffraction.

The HR-XRD equipment used in this work is Bruker D8 Discover HR-XRD which is shown in Figure 3.19. The main components of the HR-XRD system include an X-ray tube, primary optics unit, motorized sample stage, secondary optics unit and signal detector. A wavelength of 1.5418 Å X-ray is conducted by an X-ray tube with copper (Cu) anode, filtering and collimating by a primary optics unit which contains a Goebel mirror, a divergence slit, a monochromator and a Soller slit. Thus, a symmetrical X-ray electron beam with narrow wavelength distribution is produced. When X-ray is incident onto a sample which is loaded on a motorized sample stage, scattered beams will be collected by a secondary optics unit sharing the same function with primary optics unit and recorded by the detector.

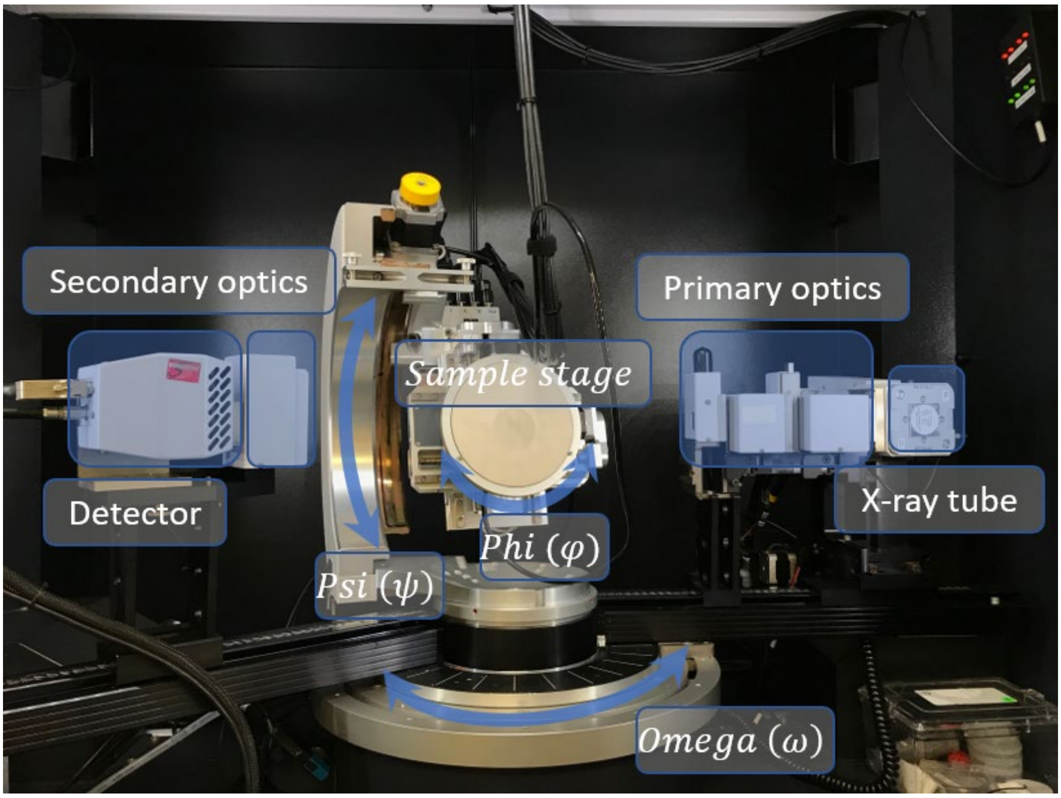

Figure 3.19: Bruker D8 XRD image with illustration of components and parameters.

Two modes of scans are applied for characterization in this work, which are $\omega - scan$ and $\omega - 2\theta$ scan.

$\omega - scan$, also referred as X-ray rocking curve (XRC), is used to investigate defects in crystal films in terms of dislocation density, misorientation, curvature and inhomogeneity. The diffraction intensity is measured as a function of ω angle, conducting a single peak broaden curve. The full width at half maximum (FWHM) of the curve demonstrates the crystal quality of the characterized film as defects cause broadening in reciprocal space [20].

$\omega - 2\theta$ scan is used to measure the alloy composition and crystal orientation of a layered structure crystal film. The diffraction intensity is plotted as a function of 2θ, while ω also changes in 2 times of θ. Therefore, multiple peaks can be conducted, where the angle of each diffraction peak corresponds to a specific material or alloy with a certain composition [20].

3.3.4 Photoluminescence Spectroscopy

Photoluminescence (PL) spectroscopy is widely used for optical characterization of semiconductor materials. In this work, a home-made PL spectroscopy system is set up as shown in Figure 3.20. A 375 nm diode laser is used to study InGaN/GaN QW structures, while a 325 nm He-Cd laser is applied to investigate GaN films as its energy is higher than GaN bandgap. After an aluminium (Al) coated reflector and focusing lens, a laser spot with diametre of around 200 nm is incident on the sample. A helium closed-cycle cryostat is employed to perform temperature-dependent PL measurements from room temperature (300K) to 10K. With the guidance of condenser lenses, the PL emission is collected and focused into a Horiba SPEX 500M spectrometer which consists of a blazed holographic grating for dispersion. Finally, the emission is detected by a Horiba Syncerity thermoelectrically cooled charge-coupled device (CCD).

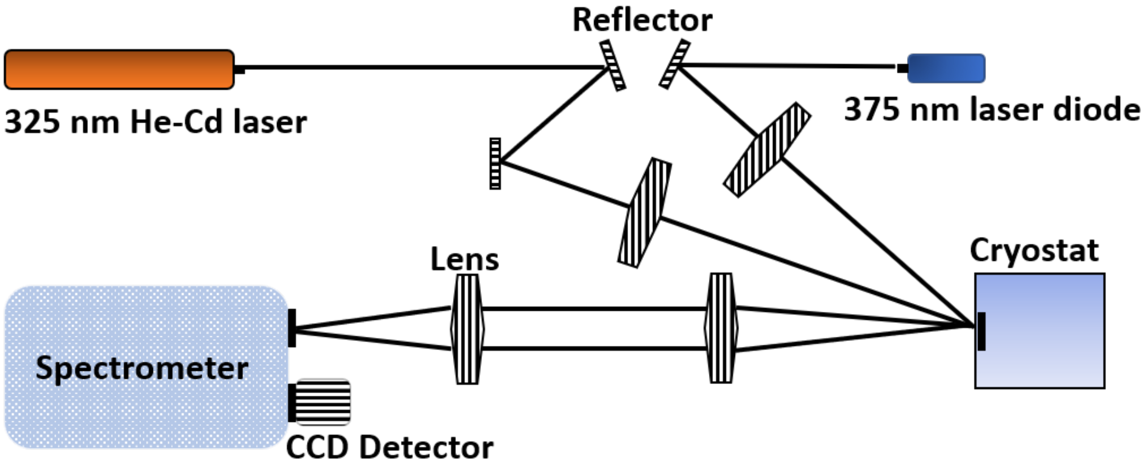

Figure 3.20: Schematics of the PL system.

3.3.5 Time-resolved Photoluminescence

Time-resolved photoluminescence spectroscopy (TR-PL) is a powerful tool for investigating the fast-electronic deactivation process which results in the emission of photons. The excited state dynamics can be analysed in a form of decay profile which describes the emission intensity as a function of time after excitation. A schematic diagram of typical decay profile is shown in Figure 3.21. The whole recombination process consists of a number of photons (A_n) emitted within a certain time interval (t_n). When the recombination process is excited by a short-pulsed laser with repetition rates down to picoseconds, a decay profile can be obtained with the information regarding carrier lifetime.

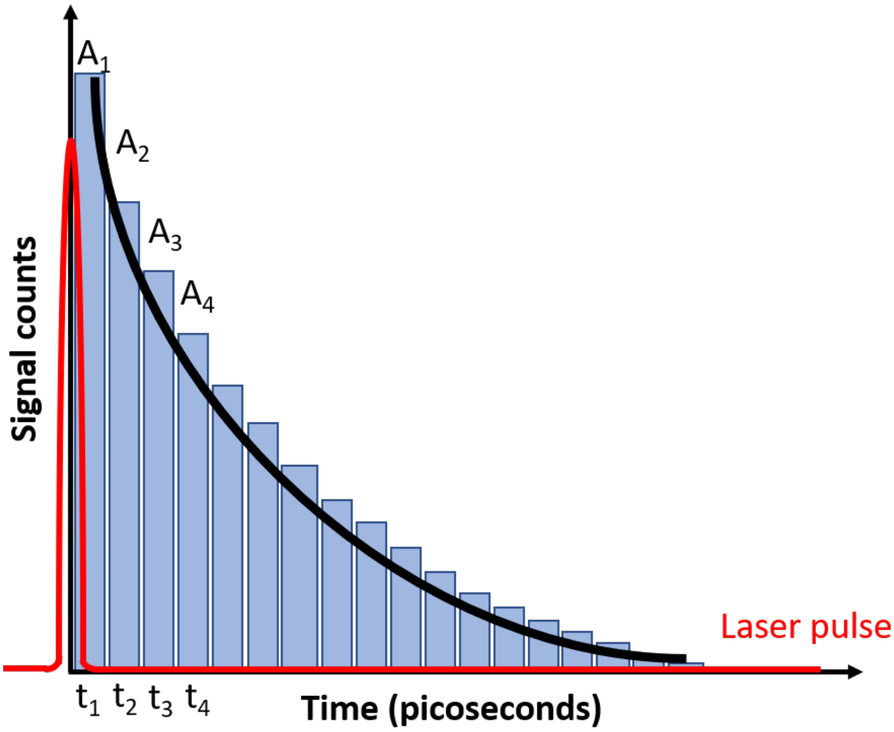

Figure 3.21: Schematic diagram of a typical decay profile.

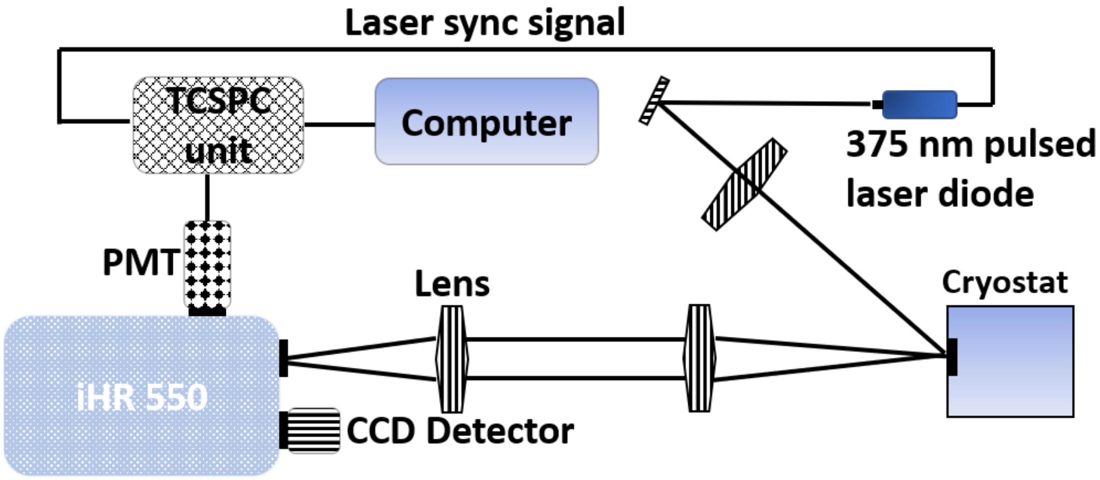

Figure 3.22: A schematic diagram of TR-PL system.

Figure 3.22 shows a diagram of the TR-PL system which is employed in this work. A PicoQuant PDL 800-B 375 nm pulsed diode laser with a 50 picoseconds pulse width and average output power of 0.1 mW at a range of repetition rate from 2.5-40 MHz is used as an excitation source. A helium closed-cycle cryostat enables temperature-dependent characterisation from 7 K to 300 K. Horiba Jobin Yvon IhR550 spectrometer is responsible for dispersing the emission into monochromatic light, and then being detected by a Becker & Hickl HPM-100-40 hybrid photomultiplier tube (PMT) detector with a timing resolution down to 120 picoseconds. The control of both detector and pulsed diode laser are synchronised by a time-correlated single-photon counting system card (TCSPC) with an FWHM of 6.5 picoseconds. The emission of photon signal is recorded as a function of time after multiple pulsed excitation cycles, forming a decay profile based on the average results of recorded signals and transferring to a computer for subsequent data analysis. The measured decay profile is a unity of actual decay time of the sample and instrument response function (IRF) of the system. In our TR-PL system, the IRF is around 150 picoseconds and quantified by the equation below:

$$e_{IRF\ system}=\sqrt{e_{Laser}^2+e_{Detector}^2+e_{TCSPC}^2} \tag{3.9}$$

The final time decay profile is conducted on the computer by using FluoFit software to execute a deconvolution process.

Reference

[1] INTEGRATED MICRO MATERIALS, "Photoresist Adhesion and HMDS (hexamethyldisilazane) Processing." [Online]. Available: http://www.imicromaterials.com/technical/hmds.

[2] Dow, "MEGAPOSIT MF-26A DEVELOPER." [Online]. Available: http://micromaterialstech.com/wp-content/dow_electronic_materials/msds/MSDS_Megaposit_MF-26A Developer.pdf. [Accessed: 16-Sep-2020].

[3] K. Takahashi, M. Hori, and T. Goto, "Fluorocarbon radicals and surface reactions in fluorocarbon high density etching plasma. I. O2 addition to electron cyclotron resonance plasma employing CHF3," *J. Vac. Sci. Technol. A Vacuum, Surfaces, Film.*, vol. 14, no. 4, pp. 2004–2010, 1996.

[4] R. C. Walker, A. G. Thompson, G. S. Tompa, P. A. Zawadzki, and A. Gurary, "Vertical high-speed rotating disk reactors for production scale MOVPE of compound semiconductors," in *Second International Conference on Thin Film Physics and Applications*, 1994, vol. 2364, pp. 484–489.

[5] AIXTRON, "Planetary principle (MOCVD)." [Online]. Available: https://www.aixtron.com/en/innovation/technologies/planetary-principle. [Accessed: 16-Sep-2020].

[6] AIXTRON, "Showerhead principle (MOCVD)." [Online]. Available: https://www.aixtron.com/en/innovation/technologies/showerhead-principle.

[7] G. B. Stringfellow, *Organometallic vapor-phase epitaxy: theory and practice*. Elsevier, 1999.

[8] G. S. Solomon, D. J. Miller, M. Ramsteiner, A. Trampert, O. Brandt, and K. H. Ploog, "Combined hydride and metal organic vapor-phase epitaxy of GaN on sapphire," *Appl.*

Phys. Lett., vol. 87, no. 18, p. 181912, 2005.

[9] Aixtron, *EpiLab 3x2FT system user manual*. Herzogenrath, 2009.

[10] Nouryon, “Gallium precursor (Select Semiconductor Grade) for the deposition of III/V semiconductors.” .

[11] Nouryon, “Aluminum precursor (Select Semiconductor Grade) for deposition technologies used in the semiconductors industry.” .

[12] Nouryon, “Solid indium precursor (Select Semiconductor Grade) for the deposition of compound semiconductors.” .

[13] Nouryon, “Magnesium precursor (Select Semiconductor Grade) for the deposition of compound semiconductors and commonly applied as dopant in GaN-based material systems.” .

[14] C. Ma, A. M. Haider, and F. Shadman, “Atmospheric pressure ionization mass spectroscopy for the study of permeation in polymeric tubing,” *IEEE Trans. Semicond. Manuf.*, vol. 6, no. 4, pp. 361–366, 1993.

[15] Entegris, “GateKeeper HX series Gas Purifiers.” [Online]. Available: https://www.entegris.com/content/dam/product-assets/gatekeeperhxseriesgaspurifiers/datasheet-gatekeeper-hx-7511.pdf. [Accessed: 16-Sep-2020].

[16] AIR PRODUCTS, “Ammonia (NH3),” 2015. [Online]. Available: http://www.airproducts.com/~/media/downloads/a/ammonia-nh3/data-sheets/en-led-ammonia-white-datasheet.pdf?productType=Gases&productLevel1=Specialty-Gases&productLevel2=Silicon-Semiconductors&productLevel3=Ammonia-NH3. [Accessed: 16-Sep-2020].

[17] J. S. Hartman, R. L. Gordon, and D. L. Lessor, “Quantitative surface topography determination by Nomarski reflection microscopy. 2: Microscope modification,

calibration, and planar sample experiments,” *Appl. Opt.*, vol. 19, no. 17, pp. 2998–3009, 1980.

[18] D. Henry, “Electron-Sample Interactions.” [Online]. Available: https://serc.carleton.edu/research_education/geochemsheets/electroninteractions.html. [Accessed: 16-Sep-2020].

[19] I. S. Grant and W. R. Phillips, *Electromagnetism*. John Wiley & Sons, 2013.

[20] M. A. Moram and M. E. Vickers, “X-ray diffraction of III-nitrides,” *Reports Prog. Phys.*, vol. 72, no. 3, p. 36502, 2009.

Chapter 4

Overgrowth and characterization of (11-22) semi-polar GaN on (113) silicon with a two-step method

4.1 Introduction

III-nitride based semiconductor devices have a trend to dominate extensive area in optoelectronic applications with the merit of excellent physical and chemical stability and direct bandgap properties, for instance visible light wireless communication (VCL), general lighting [1] and from deep ultraviolet (DUV) to visible light active detection systems [2], [3]. But the majority of current achievements of III-nitride based optoelectronic devices to date have been limited to conventional polar GaN which suffers from polarization effects. This polarization effects are combined with intrinsic piezoelectric and spontaneous polarization, also referred as quantum confined Stark effects, leading to a series of fundamental problems, including efficiency droop, emission instability in high injection current and high carrier recombination lifetime, etc. In addition, this conventional c-plane orientation has a difficulty to obtain high indium composition InGaN film with good crystal quality, leading to a so called 'green/yellow gap' which is a major obstacle for obtaining phosphor-free while light emitting diode (LED), full-colour LED display and VLC with high bandwidth.

One of a promising approach has been proposed to overcome these issues is to grow on semi-polar GaN buffer. III-nitride optoelectronic devices on semi-polar GaN buffer supply with markedly decreased polarization [4], [5], stable emission wavelength [6], enhanced indium corporation efficiency [7], reduced carrier recombination lifetimes [8], [9] and enhanced internal quantum efficiency [10], [11]. With the help of these advantages, optoelectronic devices with long wavelength emission can be achieved with enhanced optical property [12], increased response speed [13], [14] and improved emission wavelength stability [15].

For predominant advantages of substrate aspect, Semi-polar GaN on silicon substrate could benefit many merits of mature silicon technologies, low-cost compare with sapphire, SiC and GaN substrate, high scalability and good thermal conductivity. Furthermore, silicon complementary Metal-Oxide-Semiconductor Transistor (Si CMOS) is still playing a dominate role in semiconductor industry as the high device integration. And III-V based optoelectronic devices have developed many approaches to integrate with Si CMOS in a wafer-scale, such as monolithic integration technology [16], 3-D stacking [17] and dielet technology [18] which could enable III-V & CMOS applications for µLED, power conversion and communications.

The current impediments for achieving semi-polar GaN on silicon substrate are lacking planar silicon substrate and melt-back etching issue which have been introduced in Chapter II section. In order to obtain semi-polar GaN on silicon, a high index silicon substrate need to be adopted. However, the GaN film is difficult to grow on high index silicon which tends to form pseudo-crystalline state due to lack of crystalline orientation relationship. Thus, current achievements are only obtained on patterned (113) silicon substrate but still endure with strong melt-back etching issue. The details of fabricate patterned (113) silicon substrate are presented in Chapter III section. The trench morphology with 58^{o} inclination angle makes the AlN buffer layer cannot separate the GaN and Si substrate very well [19]–[22]. Thus, Ga precursor could react with silicon under high temperature and form Ga-Si alloy, leading to a degradation of GaN film with destroyed morphology [19].

In some studies, an approach of introducing mixed H_2 and N_2 as carrier gas could eliminate the melt-back etching occur due to N_2 could suppress the etching caused by carrier gas which decrease the chance of reaction between Ga and Si substrate [20]. However, the crystal quality GaN film will be deteriorated by the impurity from N_2 and also introduced excessive polycrystalline GaN deposition [20]. Another alternative approach is growing GaN below 900 °C to minimize decomposition and increase growth rate of GaN, leading to a fast coalescence of GaN film. However, the temperature is far from optimised temperature for GaN growth and introducing high carbon profile for the GaN film [23]. This will be fatal reason for $Al_xGa_{1-x}N$ based structures such as DUV LEDs and HEMTs which require high temperature growth typically above 1100 °C [3].

In this chapter, a two-step growth approach is developed to eliminate the melt-back etching and grow semi-polar (11-22) GaN film with high crystal quality under high growth temperature by introducing a thick AlN layer to fully cover the (113) patterned silicon substrate and achieving selective area growth with selectively depositing dielectric mask on non-growth facet silicon stripe. The finalised growth condition and silicon temple configuration are presented in detail. The optimisation for the growth condition and surface treatment prior to the growth are also discussed as it is critical for achieving selective area growth for GaN. Followed by corresponding metrology data for the high crystal quality semi-polar (11-22) GaN film. A brief conclusion is summarized at the end of the chapter.

4.2 Experiment

The two-step growth approach of semi-polar (11-22) GaN consist of two separate parts in which the fabrication of patterned template and the later on semi-polar GaN overgrowth.

The details of patterned (113) silicon substrate fabrication are shown in Chapter 3. The narrow width of stripe pattern could decrease the coalescence time to form a smooth GaN surface which could be more applicable for potential production. The resolution of mask aligner in our cleanroom is down to 1.5 µm. However, the actual resolution is down to 3 µm due to the degradation of stage stability and pressure uniformity. And 4 µm is well optimised condition with good uniformity (pattern width from centre to edge) cross the 2-inch wafer and very low defect density (pattern peel off issue). Thus, the 4 µm / 4 µm stripe pattern is adopted in this template fabrication.

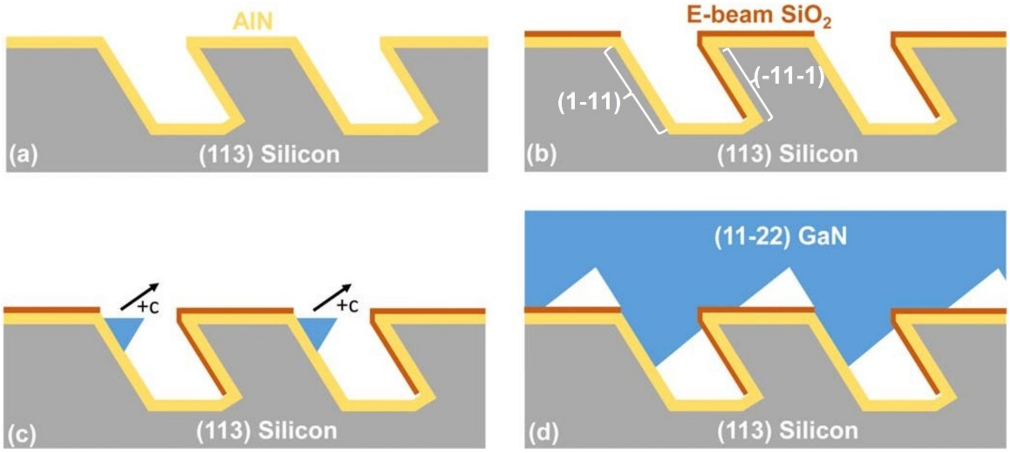

Figure 4.1: Schematics of semi-polar (11–22) GaN grown on our patterned (113) Si.

After patterning substrate, following the removal of dielectric mask by using standard 10% buffered HF solution. The subsequent work is a 400 nm AlN epitaxy growth on the patterned (113) Si template by means of MOCVD reactor as shown in Figure 4.1 (a). The AlN buffer layer is consist of three parts, Al-predose, Low-temperature (LT) AlN and High-temperature (HT) AlN layer. The growth condition of AlN buffer layer as shown in Table 4-1 below.

Table 4-1: The growth condition of AlN buffer layer.

Structure	Temperature (°C)	**MO**/NH_3 (sccm)	Time (sec)
HT-AlN	1297	**120**/500	1500
LT-AlN	1000	**20**/120	500
Al-predose	650	**20**	15

With the growth of AlN buffer layer on patterned (113) Si substrate, a well coverage for all Si stripe facets with subsequent GaN growth could effectively eliminate the occurrence of melt-back etching.

In order to perform subsequent GaN growth only within (1-11) Si facets, selective area SiO_2 masks will be deposited ex-situ by means of placing the template in electron beam deposition chamber with an oblique angle. Thus, a 10 nm SiO_2 mask is deposited on the top (113) facets and (-11-1) facets, leaving the (1-11) facets to be exposed as shown in Figure 4.1 (b).

Following 1.5 µm semi-polar (11-22) GaN overgrowth with condition of 1247 °C, 2900 sccm NH_3, 68.3 sccm TMGa which is well optimised for semi-polar (11-22) GaN on sapphire substrate and down to 320 arcsec of 002 GaN rocking curve has been achieved. [24]. As Figure 4.2 (c) shown, the selective area growth of GaN started from the exposed (1-11) facets and grew with 58° inclination angle respect to the substrate surface. Figure 4.3 shows that the coalescence happened when the GaN grows extends over to the next stripe, leading to a smooth surface of semi-polar (11-22) GaN film.

With the two-steps approach to grow semi-polar (11-22) GaN on silicon, successfully eliminate the concern of the thickness of AlN buffer layer which cannot exceed the certain thickness in order to avoid the GaN growth on the top of (113) facets [25]. In the meantime, it shows a great potential for the subsequent active layer (AlGaN based HEMT) can grow under high temperature without any melt-back etching occur.

4.3 Results and discussion

Surface treatment prior to growth

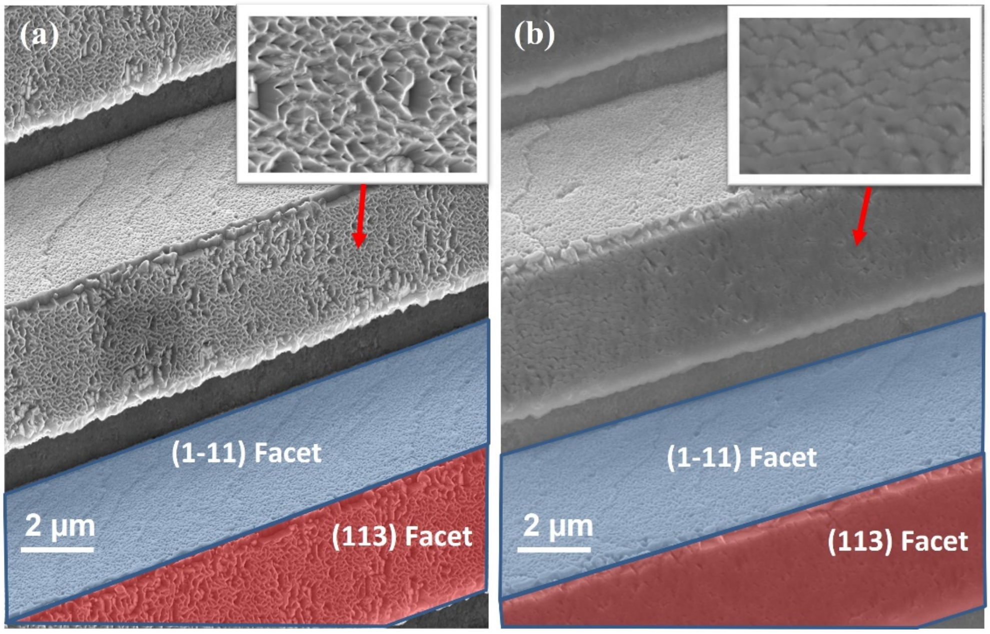

Figure 4.2: (a) SEM image of the (113) patterned Si after AlN growth (b) SEM image of the template after 10 nm SiO_x deposition by E-beam.

Figure 4.2 (a) shows the surface morphology of (113) facet is trend to form a rough surface due to (113) Si has no matched epitaxy relationship with hexagonal shape materials. After E-beam induced SiO_x deposition, the (113) facet is covered by 10 nm thick SiO_x layer to serve as dielectric mask as show in Figure 4.2 (b). However, the E-beam deposition with inclination angle will cause scattering effect during the process in which (1-11) facet is contaminated by the electron beam induced SiO_x or other impurities, leading to extremely difficult epitaxial growth for subsequent GaN overgrown.

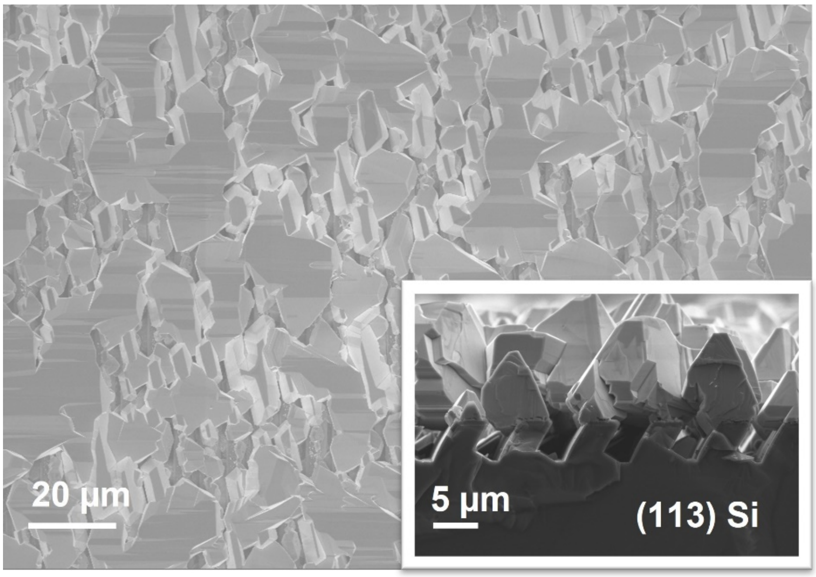

Figure 4.3: The top -view SEM image of no treatment prior to GaN growth and the cross-section SEM image of (113) Si.

Figure 4.3 shows the pseudocrystalline state of GaN is observed from the either top-view or cross-section SEM images due to the induced SiO_x on (1-11) facet or impurities from E-beam chamber which impede the GaN growth. Thus, extra surface treatment prior to the growth is needed for the template.

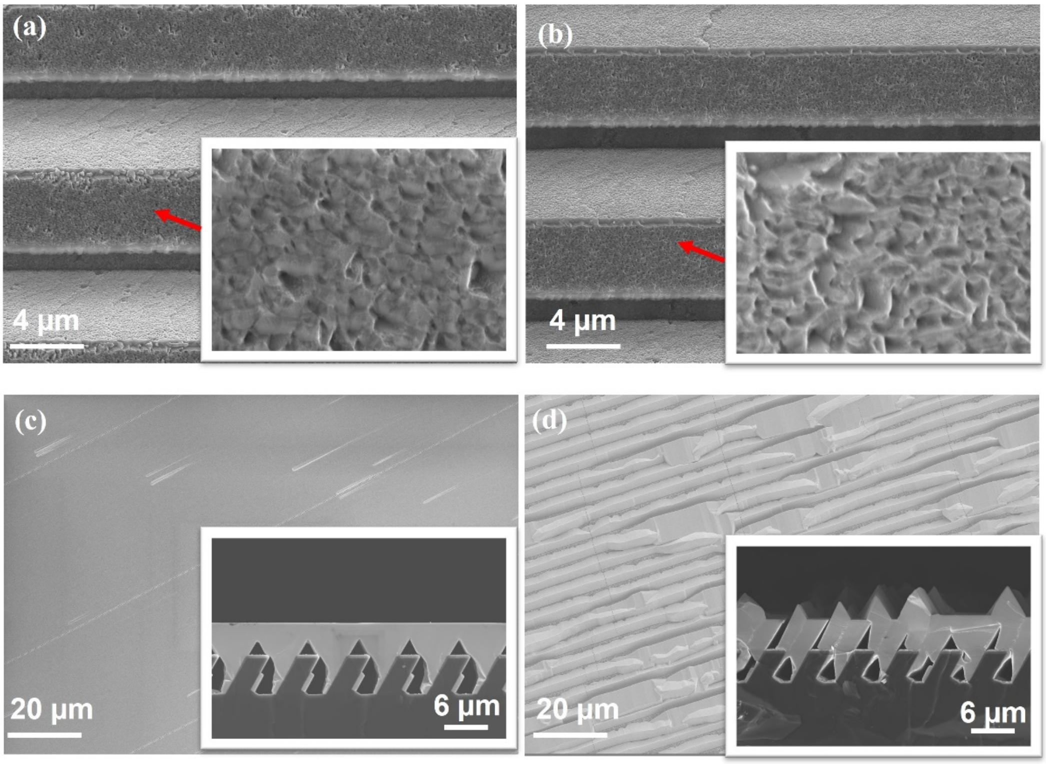

Figure 4.4: SEM images of AlN template after 1% HF treatment for 1 min (a) and 2 min (b), SEM images of GaN overgrown after 1 min HF treatment (c) and 2 min HF treatment (d).

Hydrofluoric (HF) acid is typical solvent for removing SiO_x related dielectric materials. However, the reaction speed between HF acid and SiO_x material is instant. And the SiO_x on the (113) stripe needs to be preserved in order to perform selective area growth (SAG). In this case, a diluted (1%) HF solvent will be adopted to remove the SiO_x residual on the (1-11) facet while keep the SiO_x remain on the (113) facet. There are two templates with different HF treatment time to investigate the impact of HF surface treatment. As Figure 4.4 (a) and (b) show the surface morphology of (113) stripe after 1 minute and 2 minutes HF treatment respectively. From Figure 4.4 (a), it still can see the remaining SiO_x mask on the top surface while Figure 4.4 (b) has observed some pit-related grooves revealing. After surface treatment, two templates were loaded into MOCVD reactor to perform subsequent GaN growth with identical condition. Figure 4.4 (c) and (d) show the top view and cross section SEM images for morphology investigation of the sample with 1 minute HF treatment and 2 minutes HF treatment respectively. The sample with 1 minute HF treatment shows a smooth GaN surface while the other sample shows two detached GaN with different growth orientation. From the Figure 4.4 (d) cross section SEM image, GaN starts to grow from the (113) stripe due to the removal of SiO_x mask, leading to formation of a triangle shape GaN growth along the stripe.

Optimising of Al-predose

Predosing the silicon substrate with TMAl as aluminium nucleation layer prior to the growth of AlN is the most common way to enhance the surface roughness and decrease the dislocation density of the epitaxial film by inducing lateral growth of AlN [26], [27]. However, the Al-predose in pattered silicon substrate will be more difficult to cover the silicon surface compare with the conventional planar silicon substrate as complex morphologies of silicon stripe with large inclination angle and deep groove are involved. Thus, the impact of Al-predose will be investigated with three different Al-predose times and same condition of subsequent AlN growth. And the surface morphology and defect density will be characterised by SEM and XRD respectively.

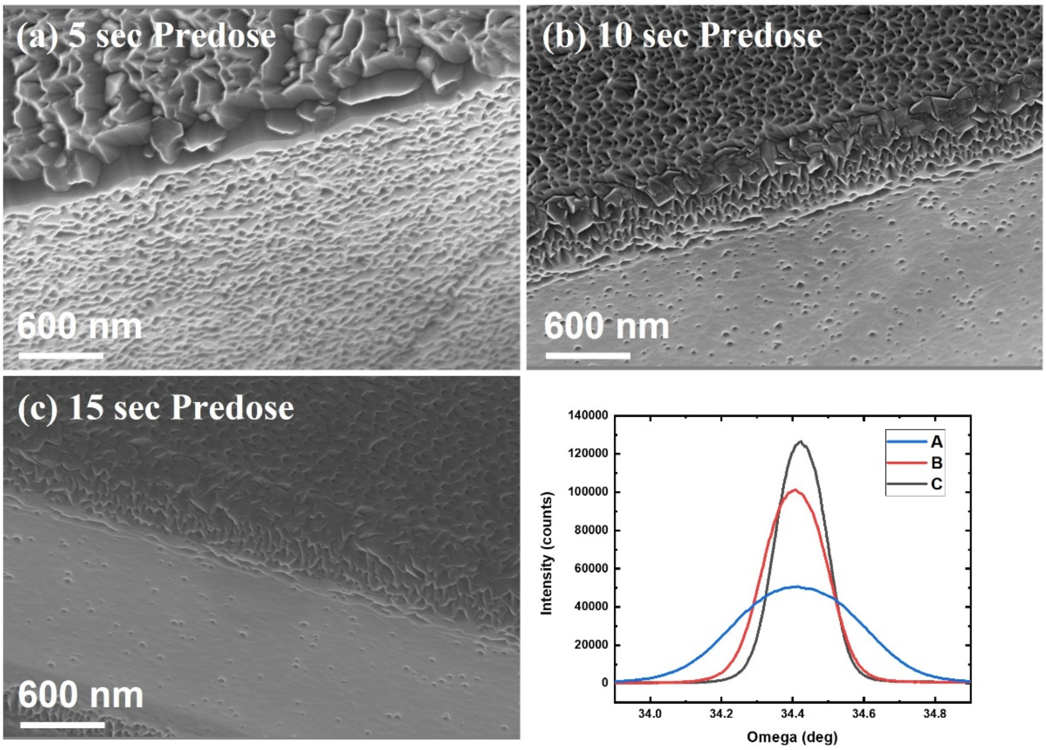

Figure 4.5: Top view SEM images of AlN template with Al-predose time of 5 seconds (a), 10 seconds (b) and 15 seconds (c), (002) XRD rocking curve of GaN overgrown film with 5 seconds, 10 seconds and 15 seconds Al-predose time labelled as A, B and C respectively.

As Figure 4.5 shown, AlN template with 5 seconds Al-predose time has the worst surface roughness in both (113) stripe and (1-11) facet while with the increased time to 10 and 15 seconds, the surface morphology has significant improvement in (1-11) facet as the improved coverage of Al nucleation layer for subsequent AlN lateral growth. In addition, the defect density of GaN overgrown film is also enhanced by the improvement of AlN template crystal quality which can be confirmed by the FWHM of (002) GaN XRD rocking curve as shown in Figure 4.5 (d). The FWHM of sample A, sample B and sample C are 1358 arcsec, 687 arcsec and 530 arcsec respectively which show consistent agreement with the Al nucleation layer for improving the defect density of epitaxial film and surface morphology of AlN layer.

Final results with optimised condition

The final growth condition of semi-polar (11-22) GaN grows on patterned (113) silicon substrate is shown in Table 4-2 after the optimisation of surface treatment and AlN buffer growth.

Table 4-2: The growth condition of semi-polar (11-22) GaN on patterned (113) silicon substrate

Structure	Temperature (°C)	Pressure (mBar)	**MO**/NH_3 (sccm)	Time (sec)
HT-GaN	1247	400	**68.3**/2900	8000
HT-AlN	1297	86	**120**/500	1500
LT-AlN	1000	86	**20**/120	500
Al-predose	650	86	**20**	15
In-situ Clean	1330	86	**-**	900

Figure 4.6 (a) shows a cross-section SEM image of (11-22) GaN overgrown film in which the aforementioned SAG process initiates on the exposed (1-11) facet only without any impedances from contamination induced by E-beam deposition and followed by GaN growth extends over the (113) stripe and coalescence with adjacent GaN.

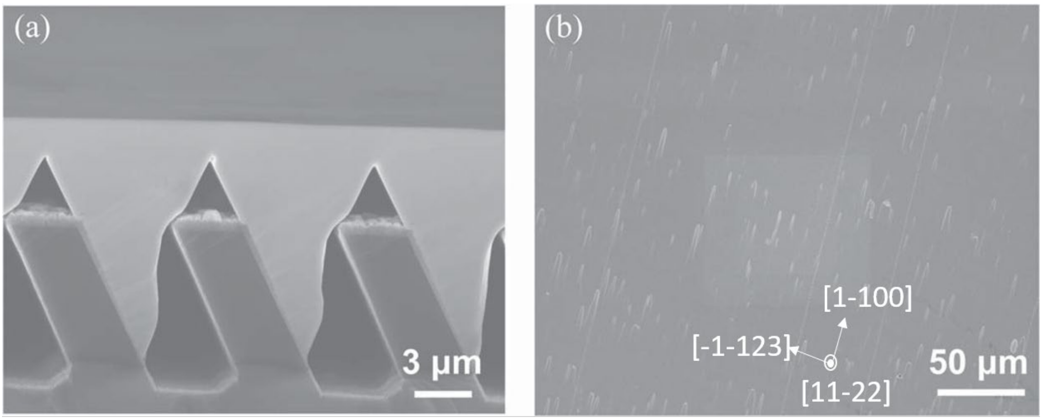

Figure 4.6: (a) Cross-sectional and (b) top-view SEM images of the semi-polar (11–22) GaN grown on our patterned (113) Si.

Figure 4.6 (b) shows a top-view SEM image of the (11-22) GaN, confirming a smooth surface despite some typical features along the [1-100] direction which is commonly caused by intrinsically anisotropic lateral growth rate of semi-polar (11-22) GaN. There is no melt-back etching observed after 8000 seconds high temperature GaN growth which indicates that the thick AlN could effectively eliminate the melt-back etching occur by introducing an enhanced separation between silicon substrate and GaN and endure the high temperature of 1247 °C for over 8000 second growth.

XRD measurement is performed to characterise the crystal quality of GaN film by measuring the (full widths at half maximum) FWHM of the rocking curves scan. For semi-polar (11-22) GaN, due to the nature of anisotropic, it is essential to measure the FWHM of XRD rocking curves as a function of azimuth angle to assess the crystal quality. Typically defining the azimuth angle of 0° as the projection of incident X-ray beam where along the [1-100] direction while 90° project along [11-23] direction. Normally, the FWHM of the XRD rocking curve will shows the largest value at [1-100] direction while the smallest value at [11-23] direction. The crystal quality of semi-polar (11-22) GaN can be roughly estimated by assessing these two values.

The best results of FWHM of the XRD rocking curves in our semi-polar (11-22) GaN film with 1.8-1.9 μm thickness are showing 580 and 511 arcsec along the [1-100] and [11-23] direction respectively in which representing a comparable good crystal quality compares with the previous reports [28] demonstrated on a porous SiN_x layer on 5 μm GaN overgrown film with around 512 arcsec at [1-100] direction.

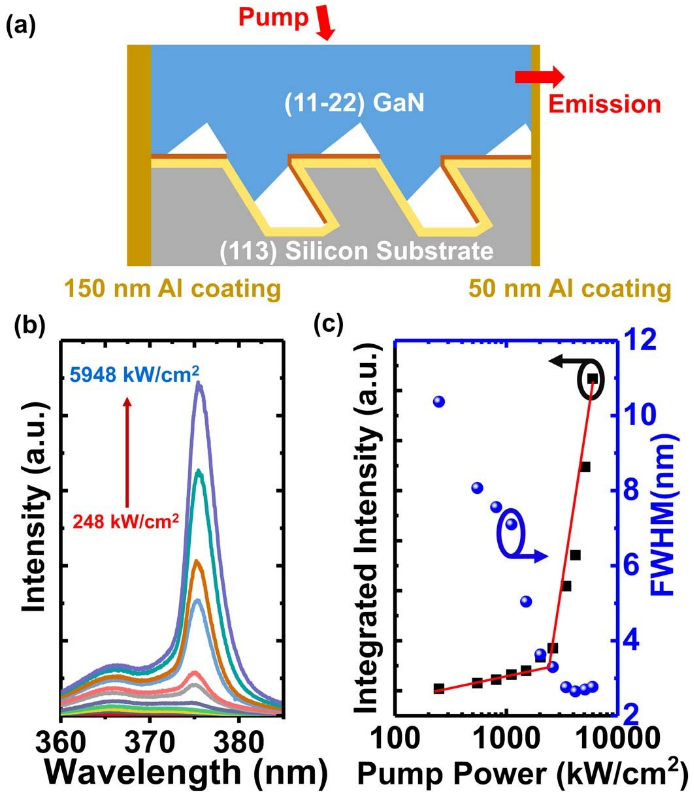

Figure 4.7: Stimulated emission spectrum measurement: (a) schematic of an edge emission configuration used for the measurement; (b) emission spectra measured as a function of excitation-power density; (c) emission

intensity and FWHM of the stimulated emission as a function of pump power.

The optical properties of our GaN overgrown film is examined by stimulated emission measurements at room temperature in which a 266 nm diode pumped Nd:YAG laser with a pulse width of 9 ns and a repetition rate of 850 Hz is adopted as an optical pumping source. The laser beam is focused by cylindrical lenses into a size of 0.2 mm x 1mm rectangular beam on the prepared sample surface in which a 5 mm length bar-shaped (11-22) GaN sample is mounted in an edge-emission geometry as shown in Figure 4.7 (a). The sample is deposited by mean of thermal evaporator with 150 nm and 50 nm thick aluminium on the side wall. The simulated emission is emitted from the edge side wall with 50 nm Al coating, passed through the monochromator and collected by a charge-couple device (CCD) array detector.

As the Figure 4.7 (b) shown, the emission spectra of (11-22) GaN sample are measured as a function of excitation power density. A broaden emission is centred at 365 nm which is from band edge emission with initial low optical pumping power density while another emission centred at 374 nm starts to be observed with increasing excitation power density and the intensity and bandwidth of the emission quickly trend to be higher and narrower. This is a typical stimulated emission process which will be happened within a decent cavity.

The emission spectra are processed by means of Gaussian function in order to fit correspondingly, conducting the integrated emission intensity and the FWHM of the stimulated emission centred at 374 nm as function of optical pumping power density respectively as shown in Figure 4.7 (c). The stimulated emission centred at 374 nm is further confirmed by the sizeable optical gain and substantial decrement of spectrum width in which superlinearly increases in integrated emission intensity starts from 1140 KW/cm2 and the FWHM of the emission decreases dramatically from 11 nm to 2.8 nm. These results are further approved the excellent optical properties and improved high crystal quality in the (11-22) semi-polar GaN overgrown film on silicon substrate.

In order to further characterise the crystal quality of our GaN film, low-temperature photoluminescence (LT-PL) is conducted to investigate the basal stacking faults (BSFs) density [15].

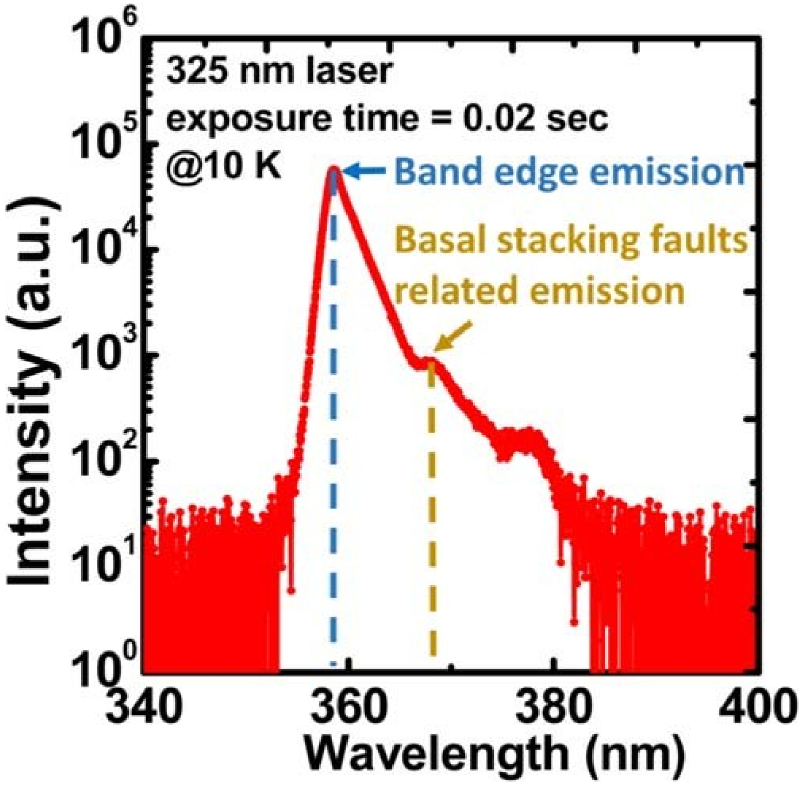

Figure 4.8: Photoluminescence spectra of the semi-polar (11–22) GaN grown on our patterned (113), measured at 10 K.

Figure 4.8 shows a typical LT-PL which is performed at 10K with 325 nm He-Cd laser as an excitation source. A log scale is applied in emission intensity which could effectively identify the weak emission peaks from defect related recombination. A typical GaN band edge emission is observed at 357 nm (3.47 eV) and two stacking fault related emissions are allocated at 368 nm (3.36 eV) and 378 nm (3.28 eV) respectively. Based on many previous reports, these two stacking fault related emissions at 3.36 eV and 3.41 eV could identified as prismatic stacking faults (PSFs) and basal stacking faults (BSFs) which are repeatedly confirmed by the combination of TEM and CL measurements [29]–[31]. A ratio of the band edge emission intensity to the BSFs-related emission intensity is approximately 66 in which could confirm the low BSF density compare with the reported results from semi-polar (11-22) GaN on sapphire substrate [28].

4.4 Conclusion

The demonstration of semi-polar (11-22) GaN on patterned (113) silicon substrate by means of a two-step approach growth method has been approved the elimination of Ga melt-back etching at high temperature for over 8000-second-long period growth. In addition, by using this approach, the condition windows for subsequent GaN optimisation and fabrication of the patterned (113) silicon are significantly eased. As a result, a high crystal quality and excellent optical performance of GaN film has been achieved, confirmed by the high near band emission and BSFs intensity ratio and observation of low threshold stimulated emission at room temperature. Also, it potentially shows a promising way to overcome the concern of high temperature for the AlGaN based HEMTs structure on silicon which typically demand high temperature.

References

[1] S. Nakamura and M. R. Krames, “History of gallium–nitride-based light-emitting diodes for illumination,” *Proc. IEEE*, vol. 101, no. 10, pp. 2211–2220, 2013.

[2] I. Akasaki and H. Amano, “Crystal growth and conductivity control of group III nitride semiconductors and their application to short wavelength light emitters,” *Jpn. J. Appl. Phys.*, vol. 36, no. 9R, p. 5393, 1997.

[3] E. Monroy, F. Omn~s, and F. Calle, “Wide-bandgap semiconductor ultraviolet photodetectors,” *Semicond. Sci. Technol.*, vol. 18, no. 4, pp. R33--R51, 2003, doi: 10.1088/0268-1242/18/4/201.

[4] T. Takeuchi, H. Amano, and I. Akasaki, “Theoretical study of orientation dependence of piezoelectric effects in wurtzite strained GaInN/GaN heterostructures and quantum wells,” *Jpn. J. Appl. Phys.*, vol. 39, no. 2R, p. 413, 2000.

[5] T. Wang, “Topical Review : Development of overgrown semi- polar GaN for high efficiency green / yellow Topical Review : Development of overgrown semi-polar GaN for high efficiency green / yellow emission,” no. 0001.

[6] Y. Zhao *et al.*, “Green Semipolar (20$\bar{2}\bar{1}$) InGaN Light-Emitting Diodes with Small Wavelength Shift and Narrow Spectral Linewidth,” *Appl. Phys. Express*, vol. 6, no. 6, p. 62102, 2013, doi: 10.7567/apex.6.062102.

[7] Y. Zhao *et al.*, “Indium incorporation and emission properties of nonpolar and semipolar InGaN quantum wells,” *Appl. Phys. Lett.*, vol. 100, no. 20, p. 201108, 2012.

[8] Y. Ji *et al.*, “Comparative study of field-dependent carrier dynamics and emission kinetics of InGaN/GaN light-emitting diodes grown on (112¯2) semipolar versus (0001) polar planes,” *Appl. Phys. Lett.*, vol. 104, no. 14, p. 143506, Apr. 2014, doi: 10.1063/1.4870840.

[9] M. Ueda, K. Kojima, M. Funato, Y. Kawakami, Y. Narukawa, and T. Mukai, “Epitaxial growth and optical properties of semipolar (112¯2) GaN and InGaN/GaN quantum

wells on GaN bulk substrates," *Appl. Phys. Lett.*, vol. 89, no. 21, p. 211907, Nov. 2006, doi: 10.1063/1.2397029.

[10] A. Strittmatter *et al.*, "Semi-polar nitride surfaces and heterostructures," *Phys. status solidi*, vol. 248, no. 3, pp. 561–573, 2011.

[11] C.-H. Chiu *et al.*, "Reduction of Efficiency Droop in Semipolar (1\bar101) InGaN/GaN Light Emitting Diodes Grown on Patterned Silicon Substrates," *Appl. Phys. Express*, vol. 4, no. 1, p. 12105, 2010, doi: 10.1143/apex.4.012105.

[12] J. Bai *et al.*, "(11-22) semipolar InGaN emitters from green to amber on overgrown GaN on micro-rod templates," *Appl. Phys. Lett.*, vol. 107, no. 26, p. 261103, 2015.

[13] H. Fu *et al.*, "Study of Low-Efficiency Droop in Semipolar ($20\bar{2}\bar{1}$) InGaN Light-Emitting Diodes by Time-Resolved Photoluminescence," *J. Disp. Technol.*, vol. 12, no. 7, pp. 736–741, 2016, doi: 10.1109/JDT.2016.2521618.

[14] A. Rashidi, M. Monavarian, A. Aragon, A. Rishinaramangalam, and D. Feezell, "Nonpolar ${m}$ -Plane InGaN/GaN Micro-Scale Light-Emitting Diode With 1.5 GHz Modulation Bandwidth," *IEEE Electron Device Lett.*, vol. 39, no. 4, pp. 520–523, 2018, doi: 10.1109/LED.2018.2803082.

[15] Y. Zhang *et al.*, "Stokes shift in semi-polar (112¯2) InGaN/GaN multiple quantum wells," *Appl. Phys. Lett.*, vol. 108, no. 3, p. 31108, Jan. 2016, doi: 10.1063/1.4940396.

[16] E. A. Fitzgerald *et al.*, "SiGe and III-V materials and devices: New HEMT and LED elements in 0.18-micron CMOS process and design," *ECS Trans.*, vol. 75, no. 8, p. 439, 2016.

[17] S. Tayal *et al.*, "A comprehensive investigation of vertically stacked silicon nanosheet field effect transistors: an analog/rf perspective," *Silicon*, pp. 1–8, 2021.

[18] S. Jangam, *Heterogeneous Integration on Silicon-Interconnect Fabric Using Fine-Pitch Interconnects (≤ 10 μm)*. University of California, Los Angeles, 2020.

[19] A. Dadgar *et al.*, "MOVPE growth of GaN on Si(111) substrates," *J. Cryst. Growth*,

vol. 248, pp. 556–562, 2003, doi: https://doi.org/10.1016/S0022-0248(02)01894-8.

[20] M. Khoury, O. Tottereau, G. Feuillet, P. Vennéguès, and J. Zúñiga-Pérez, “Evolution and prevention of meltback etching: Case study of semipolar GaN growth on patterned silicon substrates,” *J. Appl. Phys.*, vol. 122, no. 10, 2017, doi: 10.1063/1.5001914.

[21] M. Khoury, M. Leroux, M. Nemoz, G. Feuillet, J. Zúñiga-Pérez, and P. Vennéguès, “Growth of semipolar (20$\bar{2}$1) GaN layers on patterned silicon (114) 1° off by Metal Organic Vapor Phase Epitaxy,” *J. Cryst. Growth*, vol. 419, pp. 88–93, 2015, doi: https://doi.org/10.1016/j.jcrysgro.2015.02.098.

[22] Y. Honda, M. Okano, M. Yamaguchi, and N. Sawaki, “Uniform growth of GaN on AlN templated (111)Si substrate by HVPE,” *Phys. status solidi*, vol. 2, no. 7, pp. 2125–2128, May 2005, doi: 10.1002/pssc.200461575.

[23] N. Suzuki *et al.*, “HVPE growth of semi-polar (112¯2)GaN on GaN template (113)Si substrate,” *J. Cryst. Growth*, vol. 311, no. 10, pp. 2875–2878, 2009, doi: https://doi.org/10.1016/j.jcrysgro.2009.01.033.

[24] K. Xing, Y. Gong, X. Yu, J. Bai, and T. Wang, “Improved Crystal Quality of (11$\bar{2}$2) Semi-Polar GaN Grown on A Nanorod Template,” *Jpn. J. Appl. Phys.*, vol. 52, no. 8S, p. 08JC03, 2013.

[25] M. Yang, H. S. Ahn, T. Tanikawa, Y. Honda, M. Yamaguchi, and N. Sawaki, “Maskless selective growth of semi-polar (1 12¯ 2) GaN on Si (3 1 1) substrate by metal organic vapor phase epitaxy,” *J. Cryst. Growth*, vol. 311, no. 10, pp. 2914–2918, 2009.

[26] K. Y. Zang, L. S. Wang, S.-J. Chua, and C. V Thompson, “Structural analysis of metalorganic chemical vapor deposited AIN nucleation layers on Si (1 1 1),” *J. Cryst. Growth*, vol. 268, no. 3–4, pp. 515–520, 2004.

[27] X. Wang, H. Li, J. Wang, and L. Xiao, “The effect of Al interlayers on the growth of AlN on Si substrates by metal organic chemical vapor deposition,” *Electron. Mater. Lett.*, vol. 10, no. 6, pp. 1069–1073, 2014.

[28] M. Monavarian *et al.*, “Enhancement of optical and structural quality of semipolar (11-22) GaN by introducing nanoporous SiNx interlayers,” in *Proc.SPIE*, 2015, vol. 9363, doi: 10.1117/12.2079180.

[29] Y. Zhang *et al.*, “Stokes shift in semi-polar (11 2 ¯ 2) InGaN/GaN multiple quantum wells,” *Appl. Phys. Lett.*, vol. 108, no. 3, 2016, doi: 10.1063/1.4940396.

[30] J. Mei, S. Srinivasan, R. Liu, F. A. Ponce, Y. Narukawa, and T. Mukai, “Prismatic stacking faults in epitaxially laterally overgrown GaN,” *Appl. Phys. Lett.*, vol. 88, no. 14, p. 141912, 2006.

[31] M. A. Reshchikov and H. Morkoç, “Luminescence properties of defects in GaN,” *J. Appl. Phys.*, vol. 97, no. 6, pp. 5–19, 2005.

Chapter 5

Semi-polar InGaN-Based Green Light-Emitting Diodes Grown on Silicon

5.1 Introduction

During the last two decades, a significant demand from applications in III-nitrides semiconductors on silicon substrate has occurred due to the direct band structure and mature silicon technologies. While the conventional c-plane GaN on silicon [1]–[3] has shown an intrinsic limitation in terms of strong polarization in active region [4] and low indium corporation efficiency [5] which leads to the difficulty of obtaining optoelectronic devices with long wavelength and high efficiency. Thus, semi-polar (11-22) GaN has drawn a great attention in the last decade due to the significant reduced polarization [6], [7] and high indium corporation efficiency [8], [9]. After the research characterizations performed in the Chapter 4, the mechanism of Ga melt-back etching was properly investigated, and corresponding measures were introduced in order to achieve a smooth semi-polar (11-22) GaN film on patterned (113) silicon. However, due to the complexity of extra steps are involved in order to perform the dielectric masks and thicker AlN buffer layer, the outcomes are low yield, and the wafer uniformity is far from satisfaction. In addition, for the photonic devices such as InGaN based LEDs will not require high-temperature growth in the active region. Thus, in this chapter, we offered a further optimization with a special design patterned (113) silicon substrate in which stripy grooves and extra periodic gaps perpendicular to the trenches are introduced, leading to a high-quality semi-polar (11-22) GaN film with on-axis X-ray rocking curve linewidth down to 339 arcsec. Followed by InGaN/GaN based LEDs structure grown on the high-quality GaN film, green LEDs with 530nm wavelength are achieved with excellent optical performance, supported by excitation power-dependent PL measurements which confirmed a significant reduction in polarization-induced piezoelectric fields by showing almost no shift in wavelength. Furthermore, the green LEDs device performance are characterized by electroluminescence (EL) measurements which exhibit a linearly increase of output power with increasing injection current. The worth emphasizing part is the overgrowth technique on the designed graphic (113) silicon is a potential method for manufacturing high-performance semi-polar gallium nitride transmitters on silicon substrates in the long wavelength region.

5.2 Experimental

A (113) silicon substrate was patterned with periodic stripe trenches along the [21-1] direction of the substrate where the periodicity of the trenches is 4 μm window and 4 μm spacing. The details of the substrate fabrication are demonstrated in Chapter 3. In order to further release the strain between the silicon substrate and the GaN epilayer, extra 10 μm gaps are introduced which perpendicular to the trenches and section the wafer in every 3 mm. Compare with the two-step method approach proposed in Chapter 4, the patterned silicon substrate with optimized patterned parameters in terms of the stripe width and trench depth, is directly loaded into the MOCVD reactor to perform the full structure epitaxy growth including the active region, avoiding the complexity of the dielectric mask removal before AlN buffer layer growth and selective area deposition steps.

The control of the trench depth is based on the stripe bottom width and their relationship is plotted in Figure 5.1. The stripe width can only be limited within the standard deviation of ± 0.2 μm due to the factor of the human error and the resolution the mask aligner. The trench has inclination angle of 58°C aspect with the (113) silicon substrate surface. Thus, the trench depth can be calculated by the combination of stripe width and the stripe bottom width parameters. In addition, the stripe bottom width needs to be down to none in order to eliminate the GaN footprint which has been confirmed as one of the causes for the Ga melt-back etching issue.

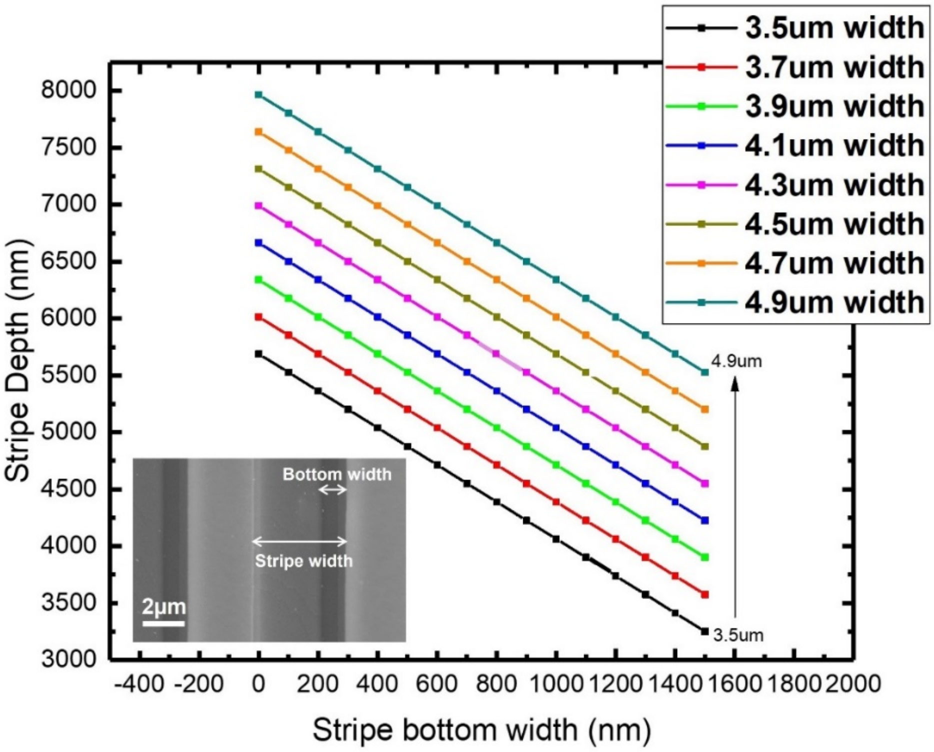

Figure 5.1: The stripe depth with different stripe width as function of stripe bottom width.

The patterned (113) Si substrate was loaded into MOCVD reactor to perform epitaxial growth and the details of growth condition as shown in Table 5-1. Initially, the Si substrate will be performed with in-situ clean at 1300 ºC in order to remove the surface oxidation. Followed by Al predose prior to AlN buffer to avoid the formation of SiN_x. The growth process of semi-polar (11-22) LED structure is shown in Figure 5.2. A well optimized AlN buffer growth condition is adopted in this structure in which can form a high crystal quality AlN buffer layer with good coverage on silicon substrate to eliminate the Ga melt-back etching occur [10]. Subsequent GaN was consist of three steps with different growth temperature. Firstly, high temperature (HT) GaN was performed at 1100 ºC to achieve good selective area growth for 1700 seconds. Then, temperature decreased to 1080 °C for further medium temperature (MT) GaN growth. After around 5000 seconds, GaN extended above the silicon stripe and complete coalescence process. The temperature further reduced to 1025 °C for low temperature (LT) GaN growth in order to form a smooth surface. The LED structure was consisted of a 1.2 μm

Si-doped n-GaN layer, 3 periods of InGaN/GaN MQWs (3 nm for quantum well and 9 nm for barrier) and end up with a 150 nm Mg-doped p-GaN.

Table 5-1: The growth condition of semi-polar (11-22) InGaN based green LED on silicon substrate.

Structure	Temperature (°C)	**MO**/NH$_3$ (sccm)	Time (sec)
p-GaN	880	Mg:420/**47**/5840	300
Barrier: GaN	880	**2.5**/8000	270
Well: InGaN	790	In:300/**1.5**/8000	57
Barrier: GaN	880	**2.5**/8000	270
n-GaN	1025	Si:4.5/**65**/2400	1500
LT-GaN	1025	**65**/2400	1300
MT-GaN	1080	**65**/2400	5000
HT-GaN	1100	**65**/2400	1700
HT-AlN	1291	**120**/500	300
LT-AlN	1000	**20**/120	800
Al-predose	650	**20**	15
In-situ Clean	1300	**-**	900

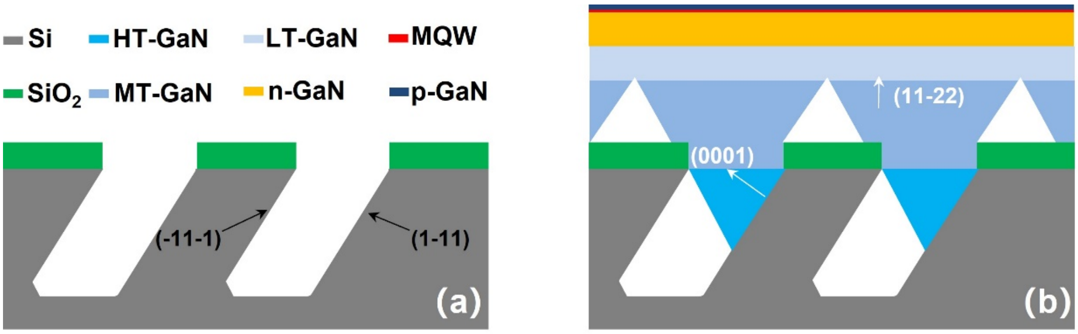

Figure 5.2: The schematic of semi-polar (11-22) LED structure growth process on patterned (113) silicon.

The grown wafer is fabricated into lateral LEDs by means of standard photolithography method. The structure of the lateral LEDs is shown in Figure 5.3 in which Ni/Au layer was deposited on p-GaN by thermal evaporator as p-contact and Ti/Al/Ti/Au was employed as n-contact on n-GaN. Finally, a Ti/Au layer was deposited on both p-contact and n-contact as pad electrode.

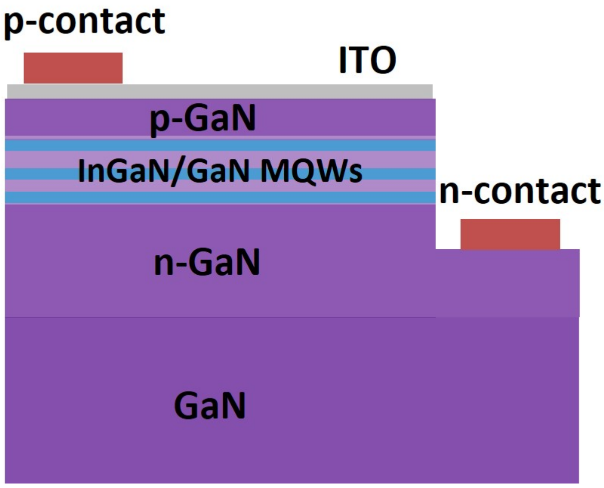

Figure 5.3: The structure of lateral LED device.

HR-SEM and HR-X-ray diffraction (XRD) are employed as metrology equipment to perform the epiwafer characterisation. The optical performance was investigated by means of standard PL measurements with a 375 nm diode laser and EL measurements

5.2 Results and discussion

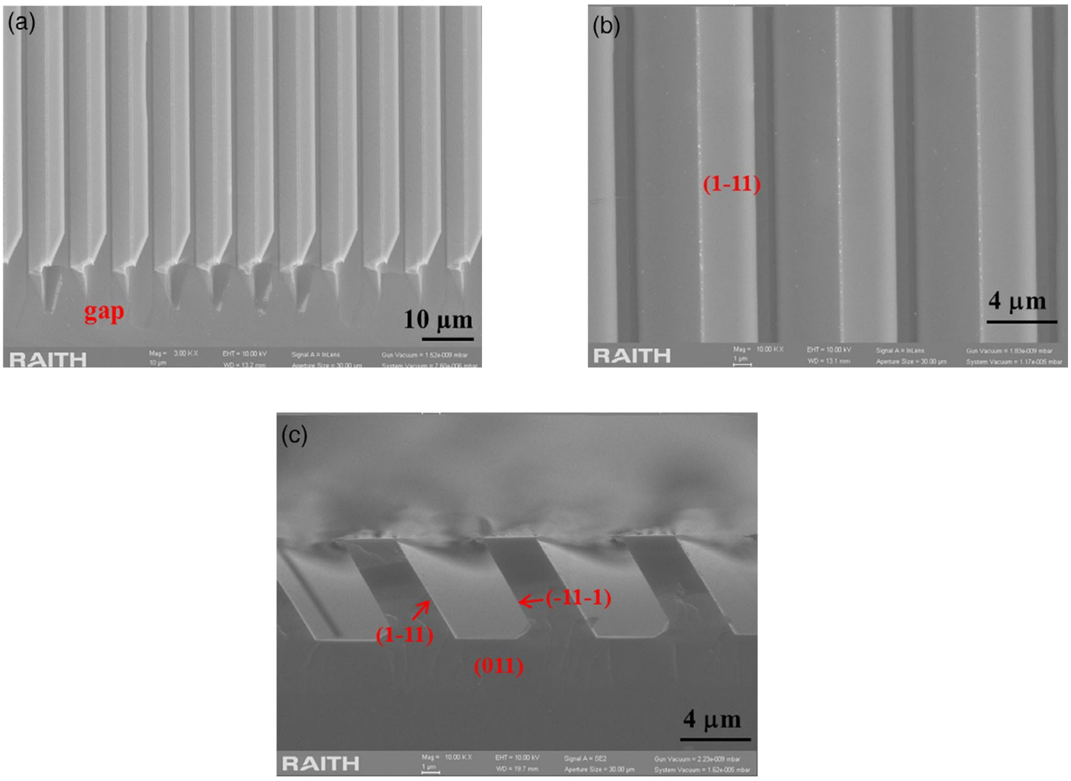

Figure 5.4: (a,b)The plan-view SEM images and (c) a cross-sectional SEM image of patterned Si substrates after the anisotropic chemical etching.

The patterned (113) Si substrate is shown in Figure 5.1 (b) and (c) after the anisotropic chemical etching. The trenches are formed by two parallel facets with an inclination angle of 58° respect to the substrate surface and one (011) facet at the bottom of the trench. The optimization for the etching depth and the growth condition are carried out in order to achieve the selective area growth for semi-polar (11-22) GaN only grown on (1-11) facet. The melt-back etching still can occur even with a 100 nm AlN buffer to separate the Si substrate with GaN as the voids generated in the trench during the growth and leads to high chance of reaction between GaN and Si substrate. Ammonia can prevent the melt-back etching as it can suppress the GaN decompose to Ga metal droplet and nitrogen complex which can easily result to melt-back etching in high temperature [11]. Thus, a 10 μm gap is introduced in the patterned substrate and sectioned in every 3 mm as shown in Figure 5.1 (a). As a result, ammonia can flow into the trench even after the GaN coalescence which can effectively eliminate the melt-back etching and also manage the strain along the [-1-123] direction to avoid the cracking generation.

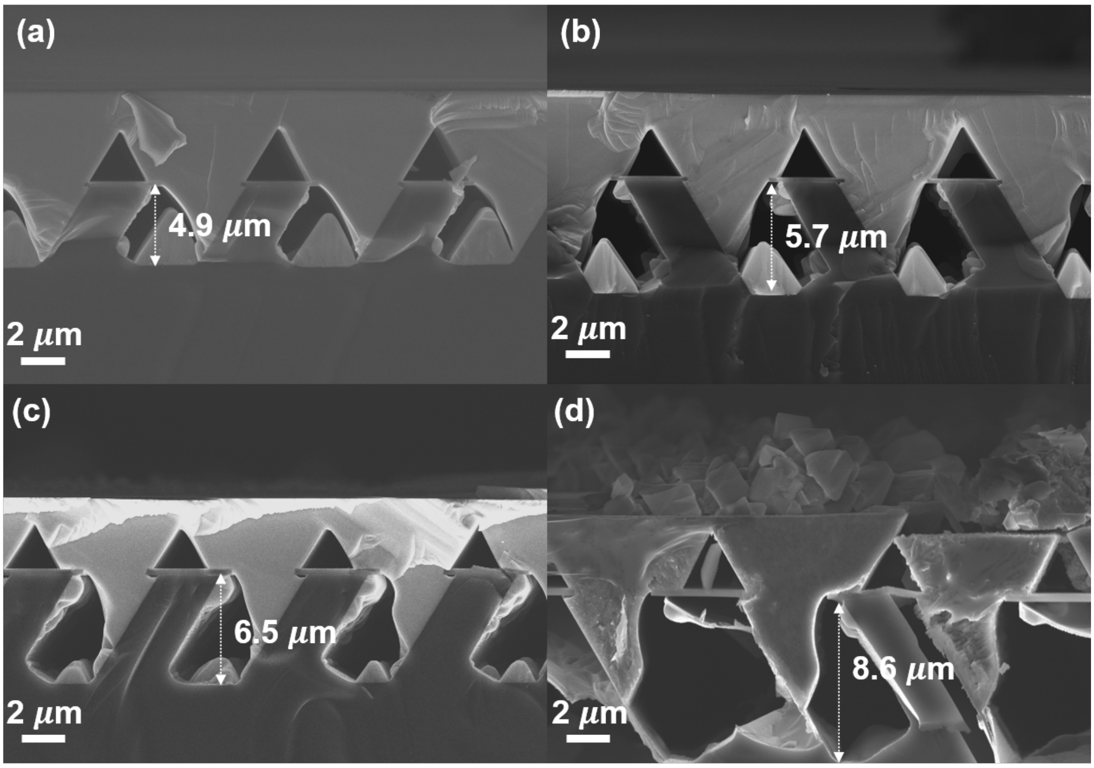

Figure 5.5: cross-sectional SEM images with different trench depth (a): 4.9μm. (b): 5.7 μm. (c): 6.5 μm. (d): 8.6 μm respectively.

Figure 5.5 shows the cross-sectional SEM images with 4.9 μm, 5.7 μm, 6.5 μm and 8.6 μm trench depth. The occurrence of GaN footprint on the bottom of the trench is mitigated with the increase of trench depth. A huge reduction of GaN footprint is observed in the trench with 6.5 μm and 8.6 μm depth. However, a strong Ga melt-back is observed when the trench depth increases to 8.6 μm due to poor coverage of AlN buffer on the bottom of the trench. Thus, the optimized trench depth is approximately in a range of 6.5 μm to 7.5 μm.

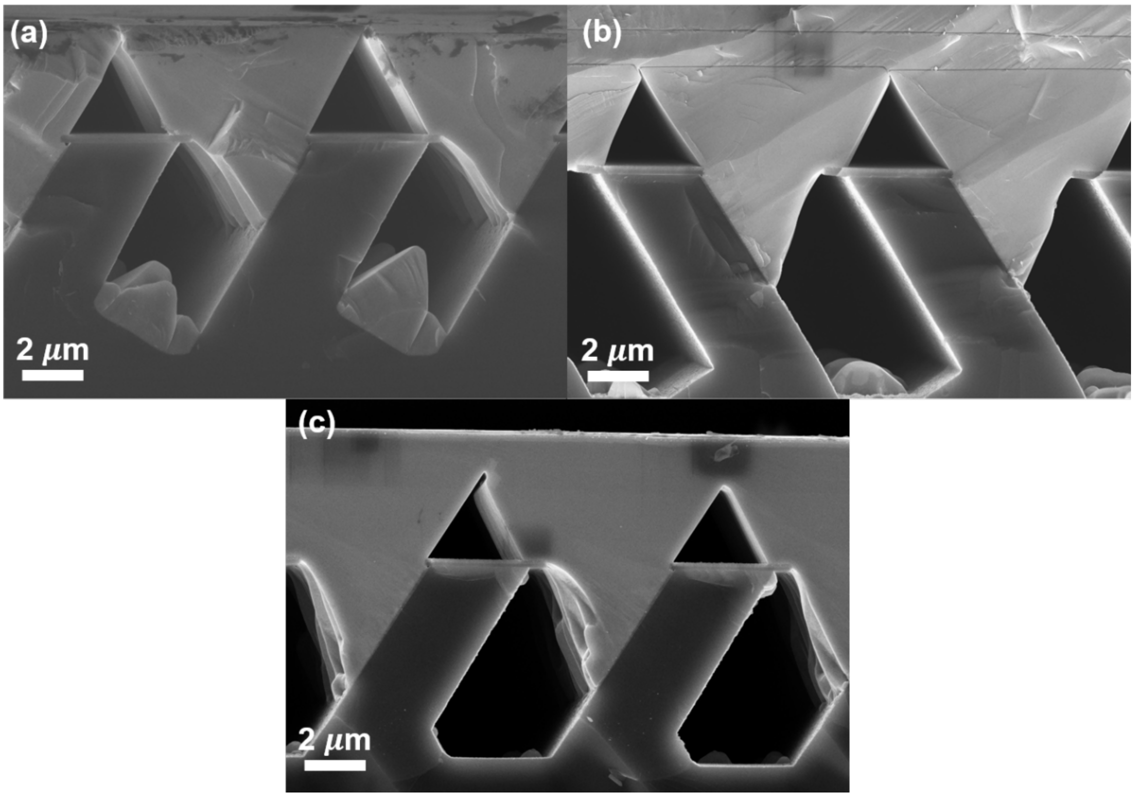

Figure 5.6: cross-sectional SEM images of different initial growth temperature of GaN and fixed trench depth (7 μm). (a): 1080 °C initial temperature. (b): 1090 °C initial temperature. (c): 1100 °C initial temperature.

A further optimization is conducting with the aspect of initial growth temperature to eliminate the GaN footprint on the bottom trench, leading to an excellent selective area growth of GaN. As shown in Figure 5.6, the cross-sectional morphology of the bottom trench with 7 μm depth is presented in three different initial growth temperatures. The bottom crystalline is a combination of (113) and (1-10) Si as the thermal dynamic equilibrium of wet etching process. And both two facets are less favorable for GaN growth compare with (111) Si facet. The free path of gallium precursor is increased with the temperature, forming a selective area growth only on (1-11) Si facet. No GaN footprint is observed at the bottom of the trench with an initial growth temperature of 1100 °C.

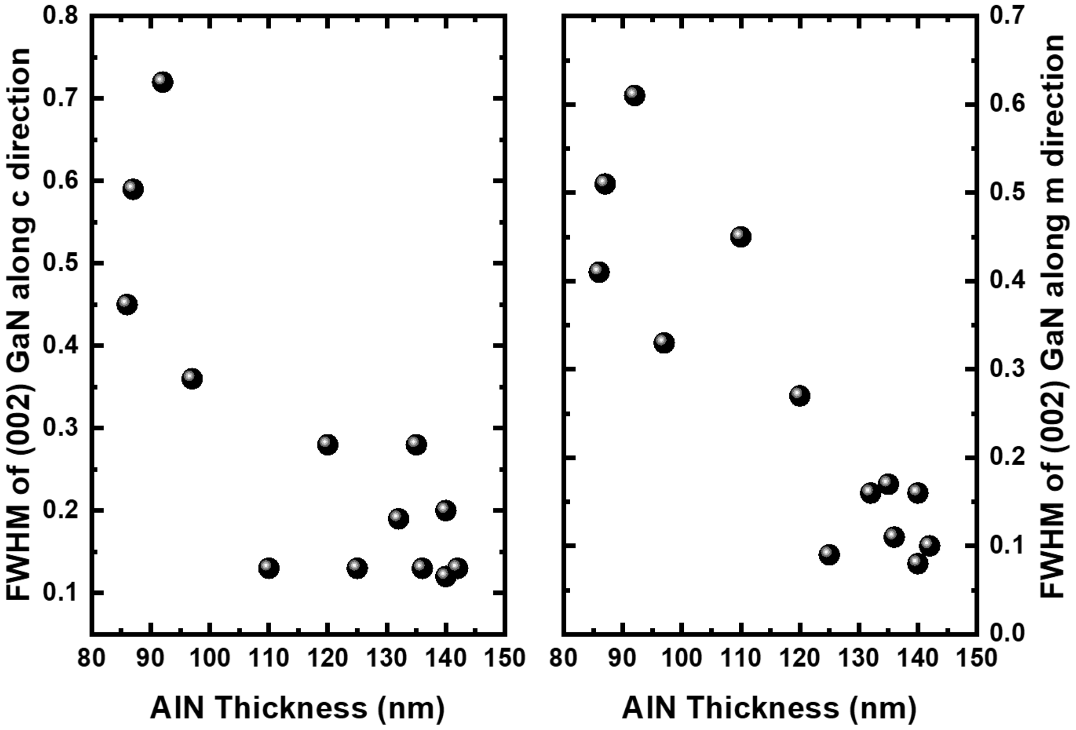

Figure 5.7: (a): GaN XRD along c-direction as a function AlN buffer thickness. (b): GaN XRD along m-direction as a function AlN buffer thickness.

Moreover, the impact of AlN buffer layer thickness on the crystal quality of GaN is investigated. The GaN XRD FWHMs along c-direction and m-direction are measured as a function of AlN buffer layer thickness as shown in Figure 5.7. The general trend of increasing AlN thickness will lead to a small value of XRD FWHM, resulting in superior crystal quality of GaN film.

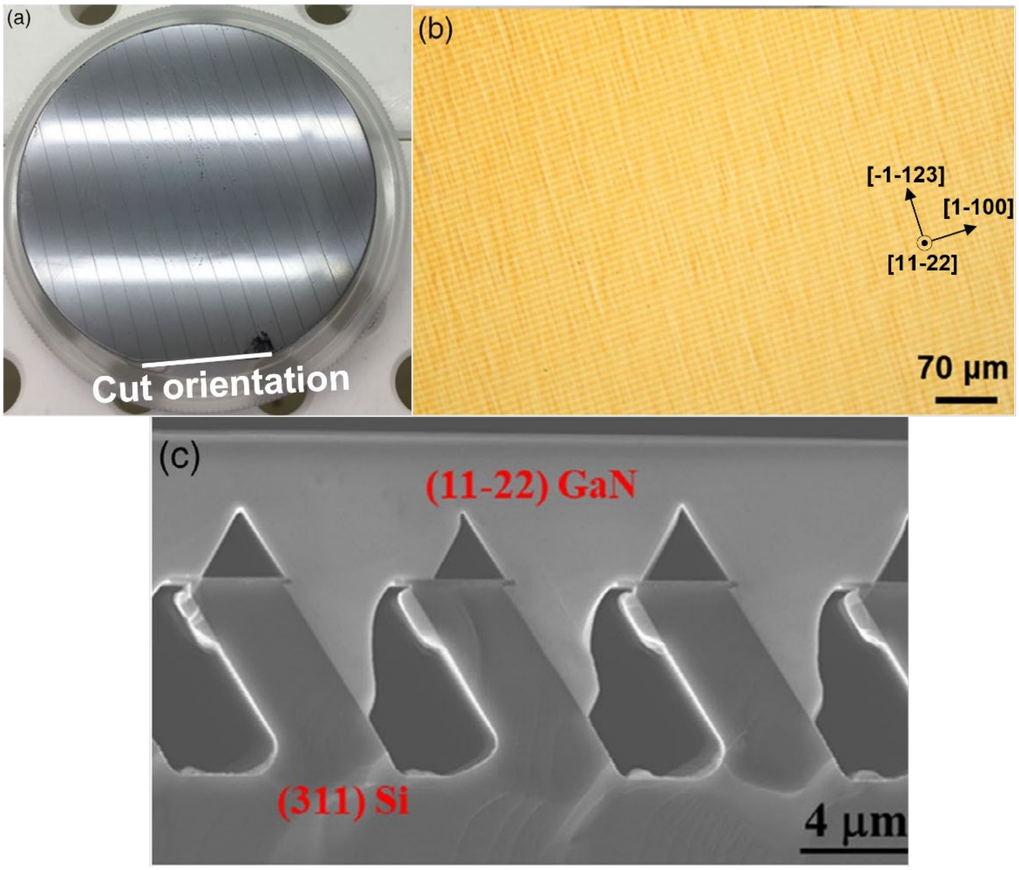

Figure 5.8: (a) Photo of 2" wafer, (b) a plan-view microscope images for (11-22) GaN on patterned Si, and (c) a cross-sectional SEM image

A photo of 2" (11-22) GaN on silicon without any melt-back etching is shown in Figure 5.8 (a). The black lines with 73° inclination angle aspect to the wafer cut orientation are the 1 mm gap which are introduced for strain relaxation. The surface morphology and cross-sectional images are further characterised by optical microscope and SEM as shown in Figure 5.8 (b) and (c) respectively in order to confirm the results. Mild stripes feature along [-1-123] direction is observed in Figure 5.8 (b) and the black lines along [1-100] direction are the trenches underneath the GaN film. The morphology of Ga melt-back etching was showed in Chapter 2 in which an extremely rough surface of GaN film and a deep hollow in Si substrate normally will occur. From Figure 5.8 (b) and (c), smooth GaN surface and complete Si substrate structure remained are observed across the whole wafer which further support the special design Si patented is completely eliminate the melt-back etching during the GaN growth. The full width at half maximum (FWHM) of on-axis XRD rocking curves of GaN film are characterised as a function of azimuth angle as shown in Figure 5.9 due to the anisotropic of semi-polar GaN growth. Normally, the azimuth angle of 0° is defined as the projection of X-ray beam onto the sample surface in which parallel to (10-10) direction of GaN film, whilst the projection of incident beam is perpendicular to the (10-10) direction as 90°. The (113) silicon substrate can be used as reference to align the (10-10) direction of GaN film as the (1-11) facet of Si stripe is parallel to (10-10) direction of GaN. Thus, the 90° of azimuth angle can be found with the (1-11) Si with 58° inclination angle. Based on the data of Figure 5.9, the FWHM values of (11-22) GaN on (113) silicon substrate are in a range of 339 and 406 arcsec in which the results are showing a significant improvement compare with the results of 626 and 1360 arcsec from the reference (11-22) GaN directly grow on m-plane sapphire.

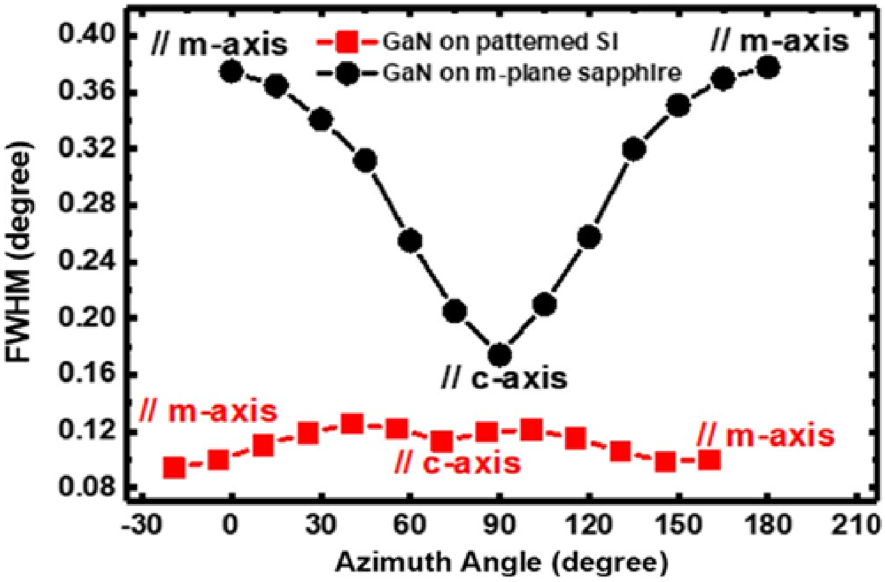

Figure 5.9: On-axis XRD FWHMs as a function of azimuth angle for the semi-polar (11-22) GaN on patterned Si.

The high crystal quality of our semi-polar GaN is further confirmed by optical characterization. Figure 5.10 shows the PL spectrum of our (11-22) GaN measured at 10 K, where the spectrum of standard (11-22) GaN directly grown on sapphire is also shown for comparison. For standard (11-22) GaN on sapphire, due to a high density of extended defects such as SFs with a typical density of $5 \times 10^5\ cm^{-1}$, low-temperature emission is dominated by basal plane stacking fault (BSF)-related peak (around 3.42 eV) and prismatic stacking fault (PSF)-related peak [12], which are much stronger than the band-edge emission at 3.48 eV. However, for our (11-22) GaN on patterned Si, the main emission peak is the band-edge emission at 3.48 eV, with a low shoulder peak that could be ascribed to the BSF-related emission. It means that the density of BSF-related emission is low. Compared with the (11-22) GaN directly grown on sapphire, the intensity of the band-edge emission is around 500 times higher, also confirming the high crystal quality of the (11-22) GaN on patterned Si. The redshift of 9 meV for the band emission of (11-22) GaN on Si compared with that on sapphire can be ascribed to the tensile strain induced by larger mismatch between the thermal expansion coefficients of GaN and Si [13].

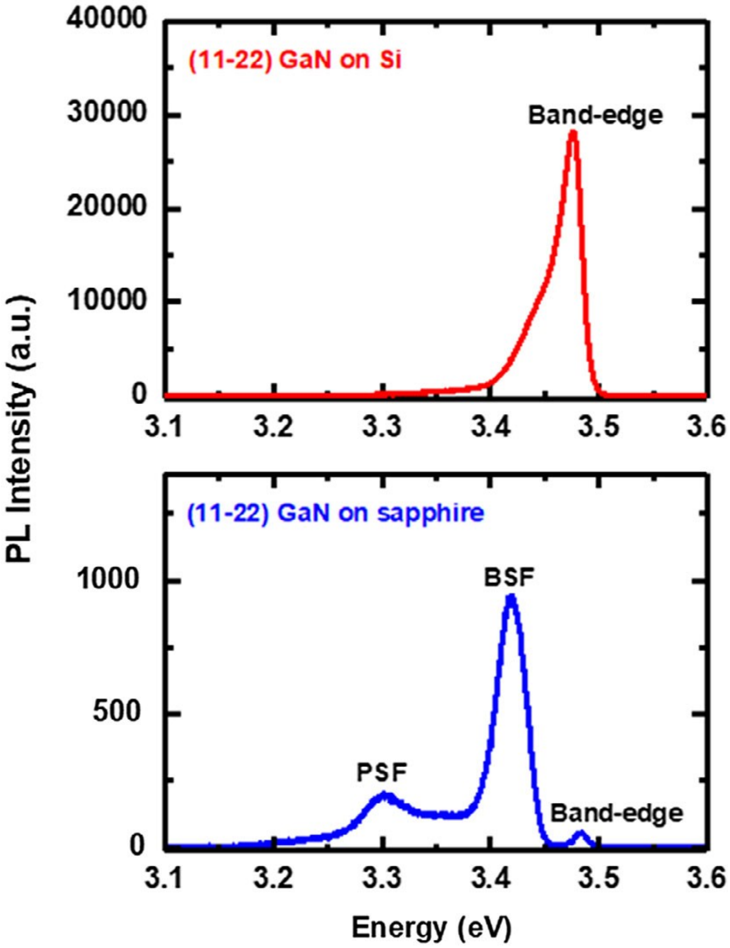

Figure 5.10: PL spectra at 10 K of (11-22) GaN on patterned Si and (11-22) GaN directly grow on sapphire.

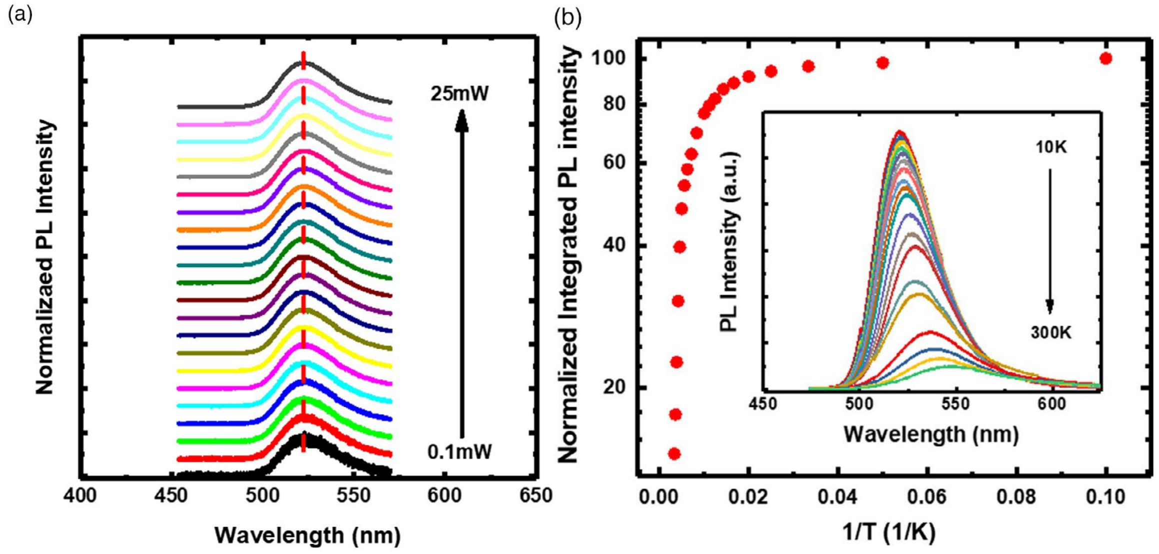

Figure 5.11: (a) Power-dependent PL spectra measured at room temperature. (b) Normalized integrated PL intensity versus 1/T. The inset is the PL spectra measured at different temperatures.

The optical property has been investigated by power-dependent and temperature-dependent PL measurements to characterize the InGaN/GaN MQW LED structure as shown in Figure 5.11 (a) and (b) respectively. The power-dependent PL spectra is performed at room temperature which has around 522 nm emission wavelength with 25 mW excitation power. With the decreasing of the excitation power down to 0.1 mW, there is almost no shift from the emission wavelength observed which indicates the polarization-induced quantum confined Stark effect (QCSE) has been effectively suppressed as the band profile would be flatten with increasing injection carriers, leading to a blue shift for emission wavelength. Temperature-dependent PL is a typical way to estimate the IQE as the IQE can be assumed as unity at low temperature (typically 3-15 K). As Figure 5.11 (b) shown, the PL measurements have carrier out from low temperature (10K) to room temperature (300K) and the integrated PL intensity is plotted as function of 1/T. The IQE of our (11-22) InGaN green LED on patterned (113) silicon is estimated around 15% which has significant improvement compare with the (11-22) InGaN LED directly grown on sapphire (~3%) and also comparable to the result (~15%) from our (11-22) counterpart on sapphire with patterned template [14].

The optical metrology of the fabricated LED device is characterized by EL measurement in which measured at injection currents from 5 mA to 100 mA and conducted light power-current-voltage (L-I-V) plot respectively as shown in Figure 12 (a). A 550 nm emission wavelength is observed with 5 mA injection current which indicates a high indium composition of InGaN QWs. And it is attributed by the In-rich regions in the QWs which form low-energy states filled at low currents. The higher energy states will be occupied by the injected carriers with the increasing of injection current, leading to a blue shift for the emission wavelength in which mainly ascribed to the band-filling effect [15].

Figure 5.12 (b) shows the forward voltage is around 2.7 V which is a typical value for green LEDs as the emission wavelength determines the bandgap voltage and reflects in the forward voltage of device performance. In addition, the metal contact and the sample surface are also critical for the electrical properties of the device performance as the rough surface will affect the current injection from metal contact to the active region and the high defect density increase sheet resistance in which degrade the efficiency of the device as more electrical power transforms into thermal energy [16]. The output power shows a linear increase with the increasing injection current in which indicates excellent performance of LED device. This could be also reflected in the external quantum efficiency (EQE) which has been assessed as a function of current density in the Figure 5.12 (c). A c-plane LED on sapphire with identical structure has been carried out the same measurement as reference. The EQE of (11-22) LED increases with the increasing injection current density and reached a maximum EQE of ~2% at $15\,A\,cm^{-2}$, followed by a mild creep down with further increasing current density and ended with 84% of the maximum EQE at $140\,A\,cm^{-2}$. As comparison, the counterpart sample shows a maximum EQE of 3.7% at a very low current density which is around $4\,A\,cm^{-2}$. And followed by a steep reduction ended with 35% of maximum EQE at $140\,A\,cm^{-2}$. Even though the peak EQE of c-plane LED on sapphire is slightly higher than (11-22) LED on silicon, but (11-22) LED on silicon shows a stable efficiency with the increasing of current density which further indicates the great potential for LED on (11-22) orientation to achieve high performance optoelectronic device.

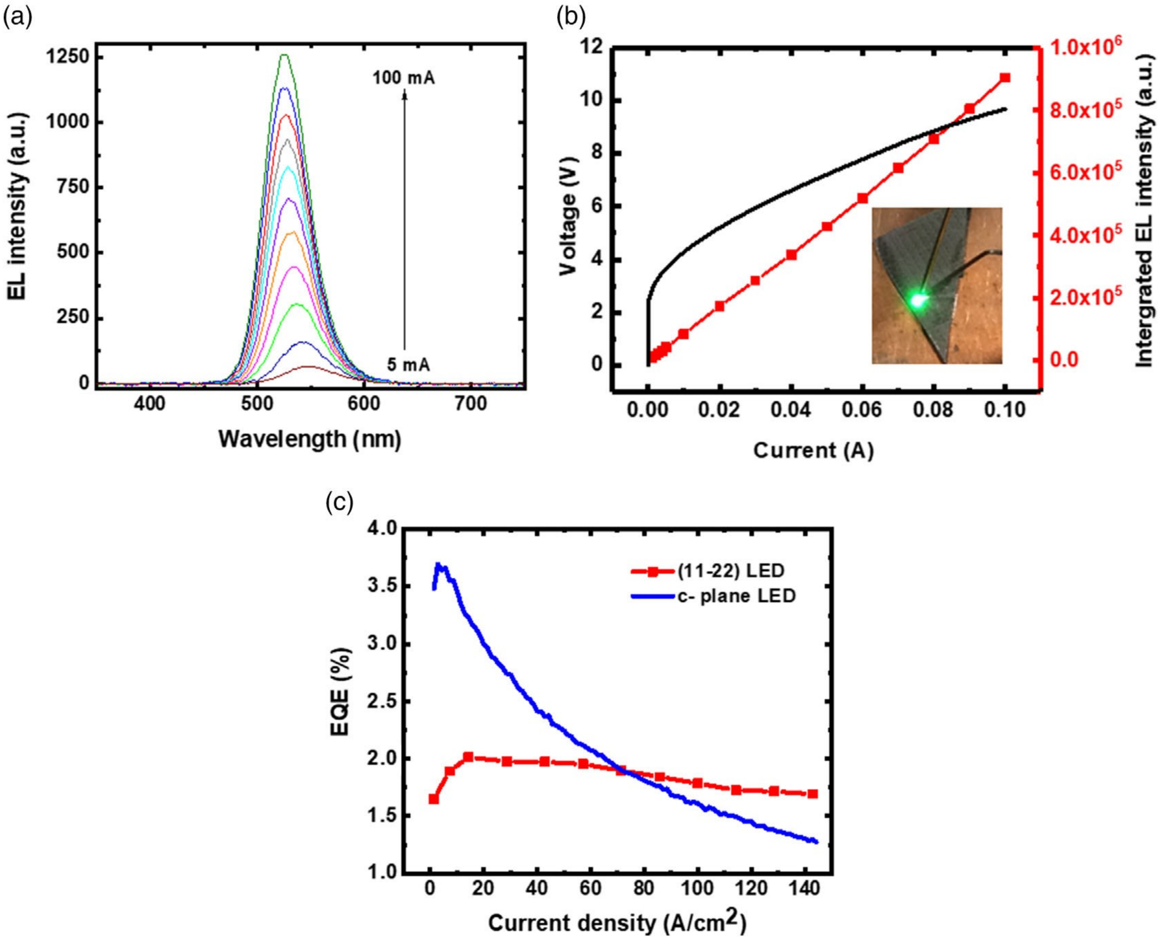

Figure 5.12: (a) EL spectra measured at a function of injection current. (b) L–I–V characteristic of the semi-polar LED. The inset is a photo of EL emission at 20 mA. (c) EQE as a function of injection current from 1 mA to 100 mA. A c-plane LED is measured as a reference.

5.4 Conclusion

A high performance (11-22) InGaN based green LED has achieved on patterned (113) silicon substrate with our designed specification for patterning and well optimized growth condition. The Ga melt-back etching has been resolved cross the whole 2” wafer by the special design. The crystal quality of GaN buffer has been characterized by XRD and LT-PL in which shows superior results compare with the sapphire counterpart. The high efficiency LED device performance has been confirmed by PL and EL measurements respectively. An IQE of 15% has been achieved and significant reduction for polarization-induced QCSE has been observed in PD-PL, leading to a stable EQE with increasing injection current density. In the meantime, the simplified template fabrication and high yield show a great potential to manufacturing semi-polar GaN based optoelectronic device on silicon substrates.

Reference

[1] S.-J. Lee, K. H. Kim, J.-W. Ju, T. Jeong, C.-R. Lee, and J. H. Baek, “High-brightness GaN-based light-emitting diodes on Si using wafer bonding technology,” *Appl. Phys. Express*, vol. 4, no. 6, p. 66501, 2011.

[2] K. J. Lee *et al.*, “Enhanced optical output power of InGaN/GaN light-emitting diodes grown on a silicon (111) substrate with a nanoporous GaN layer,” *Opt. Express*, vol. 24, no. 5, pp. 4391–4398, 2016.

[3] M. Lee, M. Yang, K. M. Song, and S. Park, “InGaN/GaN blue light emitting diodes using freestanding GaN extracted from a Si substrate,” *ACS Photonics*, vol. 5, no. 4, pp. 1453–1459, 2018.

[4] F. Bernardini, V. Fiorentini, and D. Vanderbilt, “Spontaneous polarization and piezoelectric constants of III-V nitrides,” *Phys. Rev. B*, vol. 56, no. 16, p. R10024, 1997.

[5] P. Waltereit *et al.*, “Nitride semiconductors free of electrostatic fields for efficient white light-emitting diodes,” *Nature*, vol. 406, no. 6798, pp. 865–868, 2000.

[6] T. Takeuchi, H. Amano, and I. Akasaki, “Theoretical study of orientation dependence of piezoelectric effects in wurtzite strained GaInN/GaN heterostructures and quantum wells,” *Jpn. J. Appl. Phys.*, vol. 39, no. 2R, p. 413, 2000.

[7] T. Wang, “Topical Review: Development of overgrown semi-polar GaN for high efficiency green/yellow emission,” *Semicond. Sci. Technol.*, vol. 31, no. 9, p. 93003, 2016.

[8] A. Strittmatter *et al.*, “Semi-polar nitride surfaces and heterostructures,” *Phys. status solidi*, vol. 248, no. 3, pp. 561–573, 2011.

[9] Y. Zhao *et al.*, “Indium incorporation and emission properties of nonpolar and semipolar InGaN quantum wells,” *Appl. Phys. Lett.*, vol. 100, no. 20, p. 201108, 2012.

[10] T. Wang, J. Bai, P. J. Parbrook, and A. G. Cullis, “Air-bridged lateral growth of an Al 0.98 Ga 0.02 N layer by introduction of porosity in an AlN buffer,” *Appl. Phys. Lett.*, vol. 87, no. 15, p. 151906, 2005.

[11] S. Porowski *et al.*, “The challenge of decomposition and melting of gallium nitride under high pressure and high temperature,” *J. Phys. Chem. Solids*, vol. 85, pp. 138–143, 2015.

[12] R. Liu, A. Bell, F. A. Ponce, C. Q. Chen, J. W. Yang, and M. A. Khan, “Luminescence from stacking faults in gallium nitride,” *Appl. Phys. Lett.*, vol. 86, no. 2, p. 21908, 2005.

[13] J. Bai, X. Yu, Y. Gong, Y. N. Hou, Y. Zhang, and T. Wang, “Growth and characterization of semi-polar (11-22) GaN on patterned (113) Si substrates,” *Semicond. Sci. Technol.*, vol. 30, no. 6, p. 65012, 2015, doi: 10.1088/0268-1242/30/6/065012.

[14] J. Bai *et al.*, “(11-22) semipolar InGaN emitters from green to amber on overgrown GaN on micro-rod templates,” *Appl. Phys. Lett.*, vol. 107, no. 26, p. 261103, 2015.

[15] B. Arnaudov, D. S. Domanevskii, S. Evtimova, C. Ivanov, and R. Kakanakov, “Band-filling effect on the light emission spectra of InGaN/GaN quantum wells with highly doped barriers,” *Microelectronics J.*, vol. 40, no. 2, pp. 346–348, 2009.

[16] Q. Z. Liu and S. S. Lau, “A review of the metal–GaN contact technology,” *Solid. State. Electron.*, vol. 42, no. 5, pp. 677–691, 1998.

Chapter 6

Investigation of the Influence of an InGaN Superlattice Prelayer on the Performance of Semi-polar (11-22) Green LEDs Grown on Silicon (113) Substrates

6.1 Introduction

A green semi-polar (11-22) GaN based LED was achieved on patterned (113) silicon substrate on last chapter. However, the device performance still has big margin for improvement compare with the progress on short emission wavelength in terms of blue region. The last two decades have seen an unprecedented success in developing III-nitride optoelectronics on foreign substrates, such as sapphire, which exhibit large lattice-mismatches with GaN. This has led to great success in commercialising III-nitride based emitters (light emitting diodes (LEDs) and laser diodes (LDs)), in particular blue LEDs. However, it is worth highlighting that a number of fundamental issues are still yet to be fully understood. Dislocations have been proven as non-radiative recombination centres (NRCs) [1], and thus considerable efforts have been devoted to the development of high quality GaN on widely used sapphire or silicon substrates.

For the sequence of inserting superlattice structure (SLS), very few reported that p-type InGaN/GaN SLS inserted after InGaN/GaN multiple quantum wells (MQWs) as an emitting region in an LED in order to improve the electrical properties of the device performance in terms of improving current spreading ,hole concentration and reducing turn on voltage due to the reduced contact resistance and more uniform carrier injection [2], [3]. However, it has very limited improvement on optical properties when the SLS structure was inserted after MQWs. It is also well-known that it is crucial to insert a single InGaN underlayer or an InGaN/GaN superlattice structure (SLS) as a prelayer prior to the growth of InGaN/GaN multiple quantum wells (MQWs) as an emitting region in an LED. The performance of the III-nitride LEDs are then dramatically improved [4]–[12] although the prelayer is typically grown at a low temperature which generates extra defects. Furthermore, even for growth on GaN substrates (where the dislocation density is significantly low) III-nitride LEDs without any prelayer exhibit much worse performance than those with a prelayer but grown on sapphire [10]–[12]. It suggests factor of SLS prelayer for decreasing dislocation density also play a vital role in determining the performance of III-nitride LEDs.

In order to address this issue, a number of models have been proposed to provide a mechanism for the enhanced performance of III-nitride LEDs grown with a prelayer [4]–[12]. So far, the most convincing model identifies point defects induced by vacancies as an important additional source of NRCs [10]–[12]. Furthermore, it has been demonstrated that the density of point defects in InGaN/GaN MQWs in the active region of an LED is significantly reduced if a prelayer is prepared prior to the growth of the active region [11]. Comparative experiments based on LEDs grown on sapphire and GaN substrates with or without an InGaN underlayer as a prelayer provide solid evidence to support this model [11]. The enhanced LED performance is due to a significant reduction in the density of point defects as a result of the insertion of such a prelayer grown at a low temperature, while the experiment has also ruled out any other possibilities, such as enhanced performance due to a change in surface morphology [6] or in strain state [9] or a reduction in internal electric fields [8]. However, so far, all the research on this issue is restricted to III-nitride LEDs on c-plane substrates.

Very recently, semi-polar III-nitride LEDs, in particular III-nitride LEDs grown on the (11-22) semi-polar GaN surface, have drawn increasing attention due to a growing demand for developing LEDs emitting at longer wavelengths, such as green, yellow or even red [13], [14]. Semi-polar LEDs exhibit intrinsic advantages compared with their c-plane counterparts, such as significant reduction in polarization [14], [15] and enhanced InN incorporation efficiency in InGaN [16], [17], both of which are critically important for developing long wavelength LEDs. So far, impressive results on semi-polar LEDs have been obtained on extremely expensive and size limited GaN substrates [18], [19]. Although the performance of semi-polar LEDs is still far from that of blue LEDs on c-plane substrate, it has also been recognized that the major advantage of semi-polar LEDs, in particular semi-polar (11-22) LEDs, is due to the development of LEDs emitting at longer wavelengths, such as yellow region emission [13], [14].

A careful literature review shows that all semi-polar LEDs reported so far do not utilize growth schemes involving either an InGaN underlayer or InGaN SLS as a prelayer. Therefore, it is worth investigating whether the prelayer plays a similar role in semi-polar LED to their c-plane counterparts. Of course, it is more attractive to investigate the issue on semi-polar LEDs grown on industry-compatible substrates, such as sapphire or silicon, in particular the latter due to an increasing demand for developing an integration of III-nitride optoelectronics and silicon technologies. In this chapter, the proposed growth structure and corresponding optical measurement setup. Followed by result discussion. Finally, a brief conclusion is given in the end of the chapter.

6.2 Experimental

Two semi-polar (11-22) green LEDs with a similar structure have been grown on our semi-polar (11-22) GaN templates with high crystal quality obtained on patterned (113) Si substrates. For the detail of the patterned (113) silicon and the material characterization of the semi-polar (11-22) GaN templates, please refer to our recently published paper [20]. The LED structure with a SLS prelayer has a 1.2 µm n-type GaN layer and then 15 pairs of $In_{0.03}Ga_{0.97}N$/GaN SLS (3 nm/6 nm), followed by a threefold InGaN/GaN MQW as an active region, with 3 nm quantum wells and 9 nm barriers (the InN content in the InGaN quantum well is estimated to be 25%) and a final 150 nm p-type GaN layer, while the LED without any prelayer has an identical structure except for the 15 pairs of SLS. Figure 6.1 schematically illustrates these two LED structures with and without the SLS prelayer.

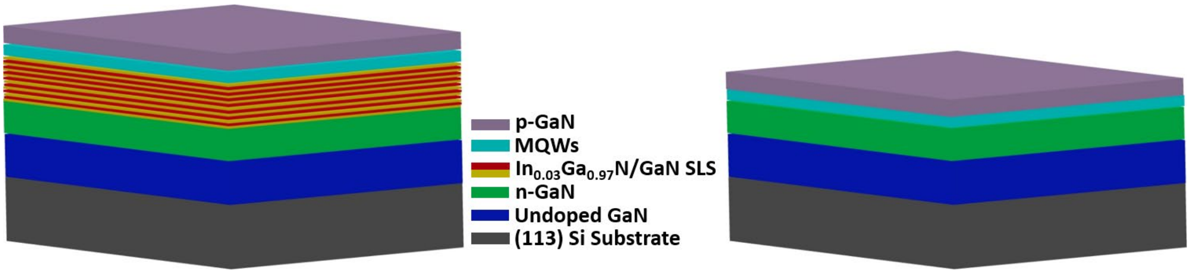

Figure 6.1: Schematic of the semi-polar (11-22) LEDs with and without the SLS prelayer grown on (113) patterned Si substrates.

Photoluminescence measurements have been conducted as a function of temperature. The samples are held in a helium closed-circuit cryostat in a temperature range from 10 K to 300 K. A 375 nm diode laser is used as an excitation source. The luminescence is dispersed by a 0.55 m monochromator and then detected by a Jobin Yvon CCD.

Time resolved PL measurements have been carried out as a function of temperature by using a time-correlated single photon counting (TCSPC) system, where a 375 nm pulsed diode laser with a pulse width of 83 ps and a pulse period of 50 ns is used as excitation source, and the emission is detected by a Hamamatsu hybrid photon counting PMT. The response time of the system is 150 ps. The samples are held in a helium closed-circuit cryostat.

Device fabrication was performed on both semi-polar green LED epi-wafers in a same batch for detailed comparison by means of standard photolithography technique. Lateral LED mesas with a typical size of 330 × 330 μm^2 were formed using dry etching. A highly transparent Ni/Au layer and a Ti/Al/Ti/Au alloy have been deposited by a thermal evaporator and then annealed by rapid thermal annealing in order to form p-contact and n-contact, respectively. A Ti/Au alloy has been finally deposited as pad electrodes for both p-type and n-type contacts.

Electroluminescence measurements have been performed on the bare chip LEDs as a function of injection current at room temperature in a continuous current injection mode using a

Keithley 2400 source meter.

Cathodoluminescence (CL) measurements have been carried out at room temperature using a field emission gun scanning electron microscope (SEM). Samples are placed in the SEM chamber and are tilted by 45°. The emission is collected by a Schwarzschild reflecting objective with its optical axis perpendicular to the direction of the electron beam, and then dispersed with a 1/8 m focal length spectrometer, and finally detected by a 1600-channel electron multiplying charge-coupled device.

6.3 Results and discussion

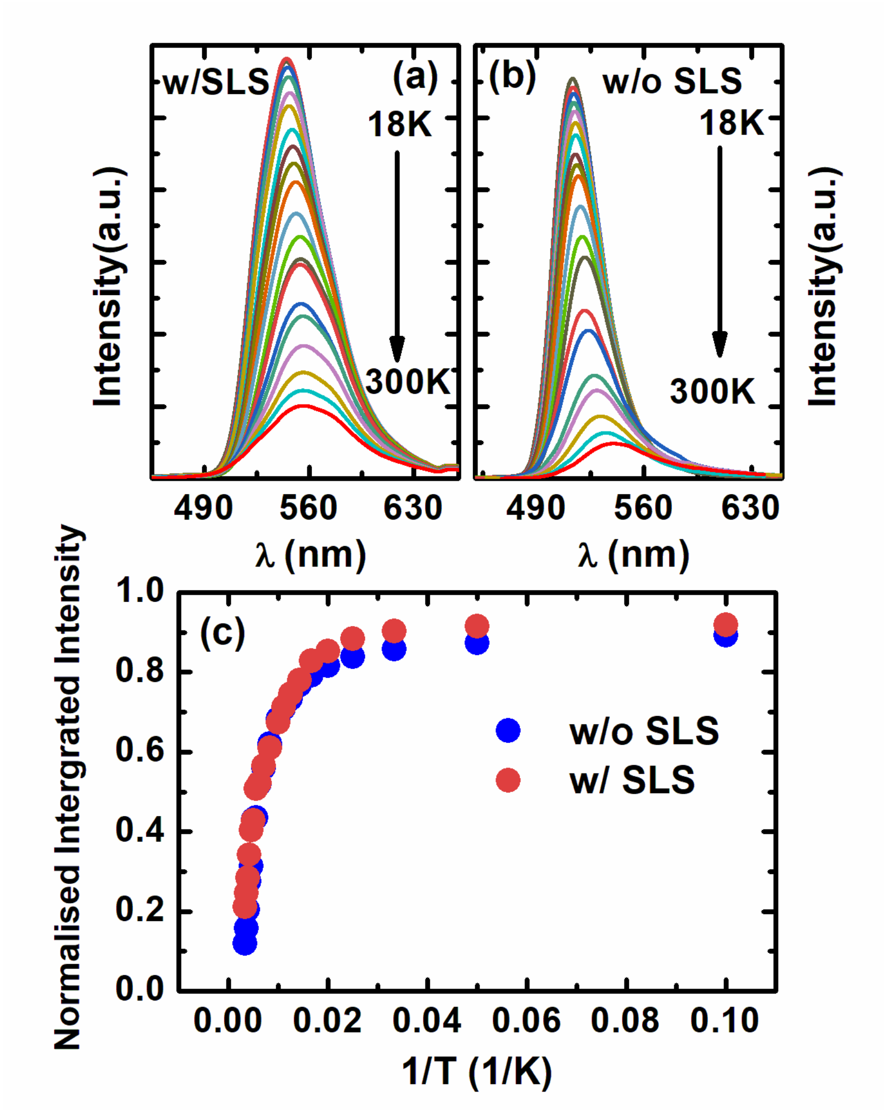

Figure 6.2: Temperature dependent PL spectra of the semi-polar LEDs with (a) and without (b) the SLS prelayer; Integrated PL intensity of the semi-polar (11-22) LEDs with and without the SLS prelayer as a function of temperature (c).

Figures 6.2 (a) and (b) show the photoluminescence (PL) spectra of the semi-polar LED samples with and without the SLS prelayer as a function of temperature ranging from 18 to 300 K. Both samples show a strong emission peak at around 550 nm. Figure 6.2 (c) shows the normalized integrated PL intensities of the two samples as a function of temperature, from which the room temperature IQE can be estimated. This is a standard, widely used method, which assumes 100% IQE at low temperature. The sample with the SLS prelayer exhibits a 23% IQE at room temperature, which is considerably higher than the 13% IQE of the sample without a prelayer. This demonstrates that the insertion of the SLS prelayer indeed enhances the IQE of the semi-polar LED by a factor of 1.8. However, compared to its c-plane counterpart, this enhancement is significantly lower. For example, it has been reported that the quantum efficiency can be enhanced by a factor of 3.5 for c-plane LEDs featuring a SLS prelayer [11].

Figure 6.3 (a) and 6.3 (b) show the EL spectra of these two LEDs (with and without the SLS prelayer) in a bare-chip form (i.e., without any packaging) as a function of injection current measured under identical conditions. In both cases, the EL intensity increases with increasing injection current. Figure 6.3 (c) provides more details of the light output (i.e., integrated EL intensity) of both LEDs as a function of injection current, clearly demonstrating that the light output of the LED with the SLS prelayer is higher than that of the LED without a prelayer. These results are in a good agreement with the IQE measurements as shown in Figure 6.2 (c). For example, the light output of the LED with the SLS prelayer is enhanced by 30% compared with the LED without a prelayer at a 20 mA injection current. This further proves the enhancement in light output as a result of utilizing a SLS prelayer. Figure 6.3 (d) shows the current-voltage characteristics of the samples with and without the SLS prelayer, which are fairly similar below 6V. After 6V, the LED with SLS showed a steeper slope for current profile. This indicates that the insertion of the SLS prelayer can slightly facilitate the current injection of the LED device.

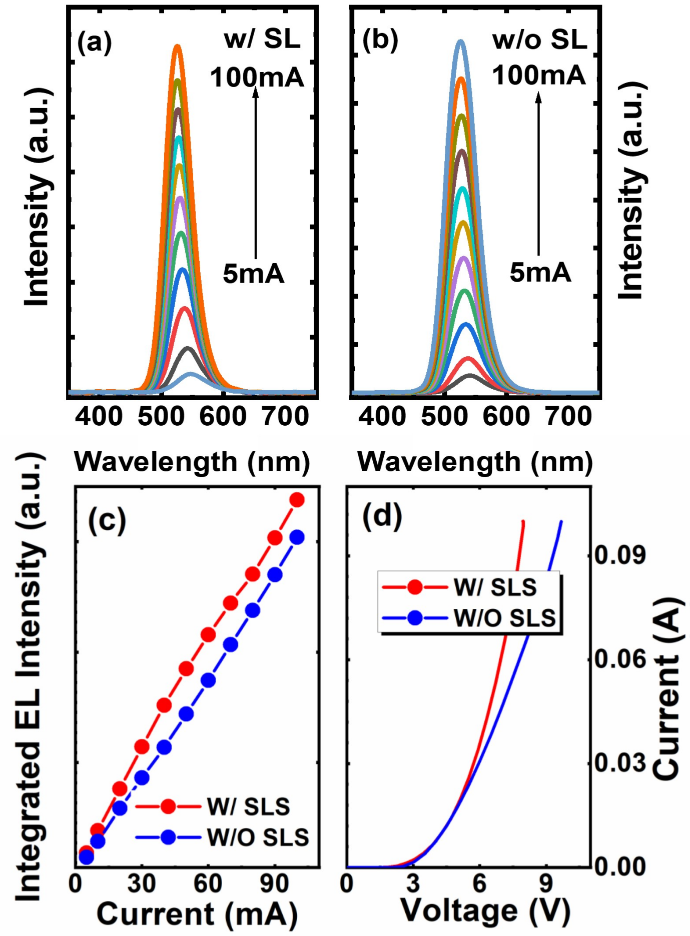

Figure 6.3: Electroluminescence spectra of the semi-polar (11-22) LEDs with (a) and without (b) the SLS prelayer as a function of injection current; Light output powers (i.e., integrated EL spectra) of the two semi-polar LEDs as a function of injection current (c).

To further investigate the influence of the SLS prelayer on the performance of semi-polar LEDs, time resolved PL (TRPL) measurements have been conducted on both samples at a low temperature (10 K). Figure 6.4 (a) and (b) show the TRPL traces of the two samples measured under identical conditions at 10 K. A standard bi-exponential model is used, and thus TRPL traces I(t) can be described by [21]–[23]

$$I(t) = A_1 \exp\left(\frac{-t}{\tau_1}\right) + A_2 \exp\left(\frac{-t}{\tau_2}\right) \tag{6.1}$$

Where A_1 and τ_1 (A_2 and τ_2) are for the fast (slow) amplitude ratio and the fast (slow) decay components respectively. The fast decay τ_1 is represented as the radiative carrier lifetime and low decay is normally as non-radiative carrier lifetime [23].

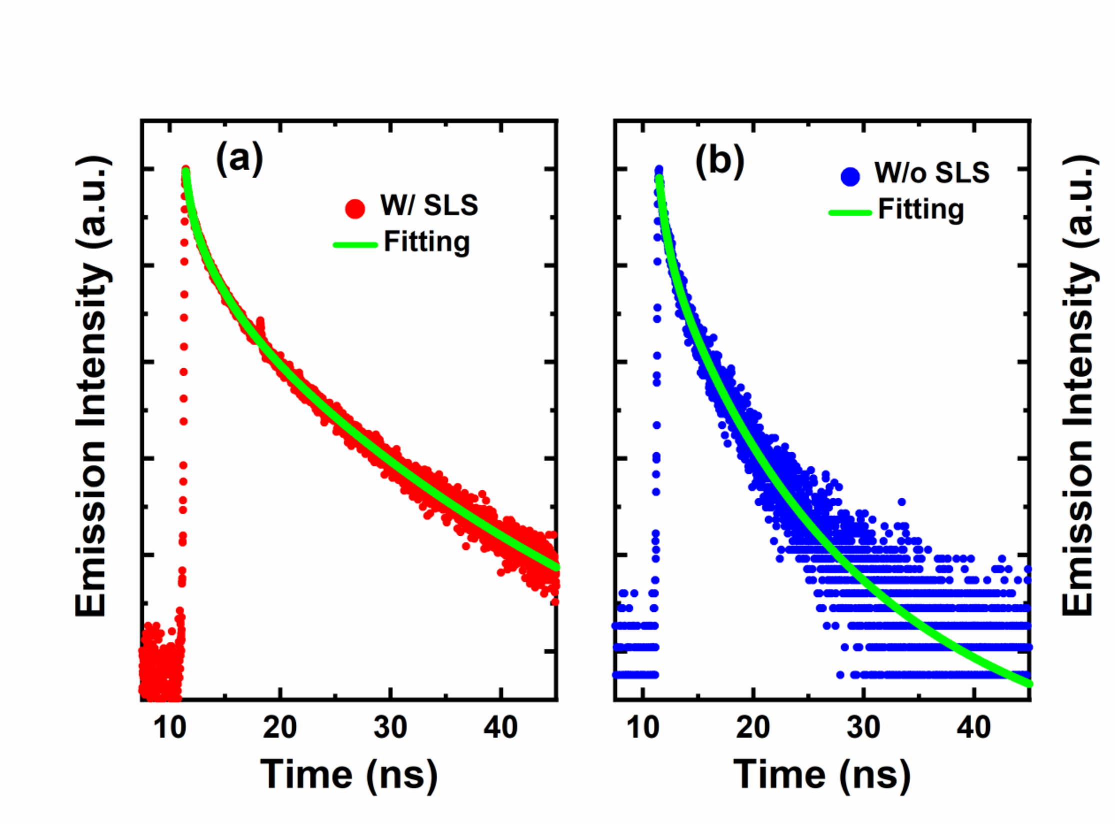

Figure 6.4: Time-resolved PL spectra of the semi-polar LEDs with (a) and without (b) the SLS prelayer, measured at a low temperature.

The fitting results have been plotted as dashed lines. From the bi-exponential fitting, the decay rates for the fast component and the slow component of the sample with the SLS prelayer have been obtained as 0.91 ns and 10.53 ns, respectively, while the sample without a prelayer shows a fast decay rate of 0.89 ns and a slow decay component of 7.56 ns, respectively. It can be seen that the fast decay rates for the two samples are very similar, indicating that the inserted SLS prelayer does not change the polarization-induced QCSE as the polarization in the InGaN/GaN MQWs in both (11-22) semi-polar LEDs is relatively weak due to the nature of semi-polar LEDs [13]. However, the sample without a prelayer exhibits a considerably faster decay rate for the slow component than the sample with the SLS prelayer, implying that the sample with the SLS prelayer exhibits a higher defect density in the MQW region than the sample without a prelayer.

In order to investigate the impact of the insertion of the SLS prelayer on the spatial dependence of the luminescence properties, cathodoluminescence (CL) measurements have been performed at room temperature. This provides a further insight on defect recombination on a micro/nano meter length scale [24].

Figures 6.5 (a) and (c) show plan-view integrated CL intensity images of the InGaN/GaN MQW peak and the near band edge (NBE) emission peak of the sample without a prelayer, respectively. Figures 6.5 (b) and (d) display the integrated CL intensity image of the InGaN/GaN MQW peak and the InGaN/GaN SLS emission peak of the sample with the SLS prelayer, respectively. Both are measured using an electron beam energy of 5 keV. In the case of the sample without the prelayer the electron beam penetrated the MQW structure and also excited the n-doped GaN underneath. Whereas for the sample with the prelayer, the electron beam did not reach the GaN, only penetrating into the SLS prelayer, and only the emission from the InGaN/GaN SLS is presented in addition to the MQW emission for this sample. Figure 6.5 (e) shows normalized mean CL spectra of both samples. The emission peak from the InGaN/GaN SLS is centred around 3.23 eV (383 nm) compared with the GaN NBE peak at 3.39 eV (366 nm) due to the low InN content InGaN layer (around 3%) in the SLS. The MQW peak also appears at a slightly different position, which is most likely due to the presence of the SLS prelayer having an effect on In incorporation by releasing the strain for of the QW, leading to a higher In content for QW with SLS structure under the same growth condition.

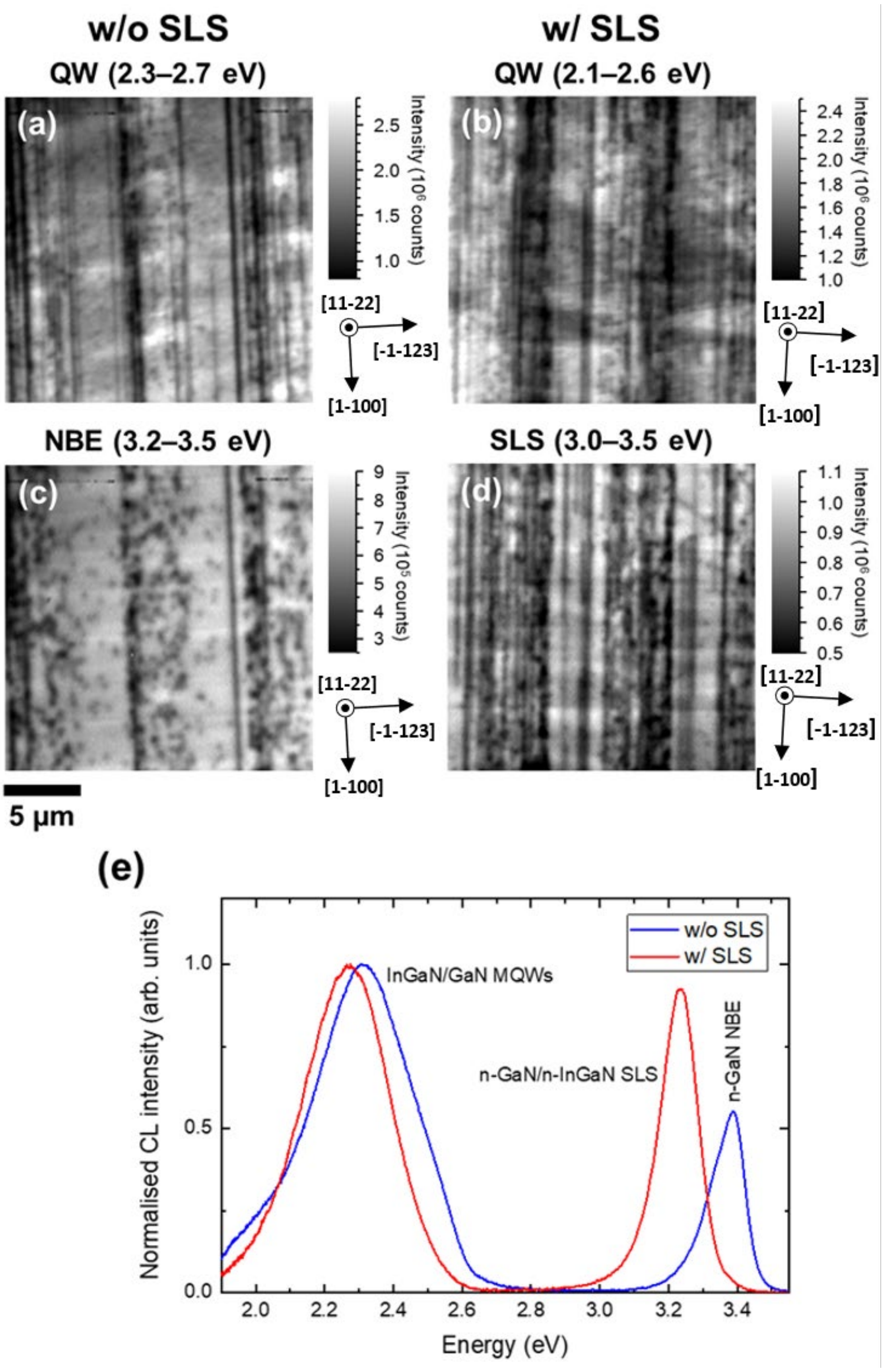

Figure 6.5: Plan-view CL imaging at room temperature: Integrated CL intensity images of the InGaN/GaN MQW peak of the LEDs (a) without and (b) with the SLS prelayer. (c) Integrated CL intensity image of the GaN NBE peak of the LED without the prelayer. (d) Integrated CL intensity image of the InGaN/GaN SLS peak of the LED with the prelayer. (e) Mean CL spectra of the LEDs with and without SLS prelayer.

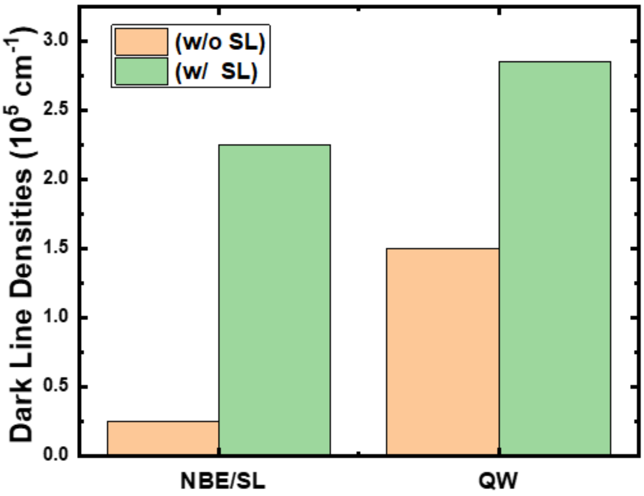

Figure 6.6: CL maps Dark line densities shown in the CL maps corresponding to Figure 6.5 a-d.

In all four intensity images in Figures 6.5 (a) to (d), a number of dark lines and dark spots can be clearly observed. As for c-plane material, dark spots are associated with non-radiative recombination at threading dislocations. Dark lines in CL images of semi-polar III-nitrides are generally caused by non-radiative recombination at stacking faults or misfit dislocations [25], [26]. The density of dark lines is higher in Figure 6.5 (b) compared with Figure 6.5 (a). The majority of dark lines in the MQW CL image (Figure 6.5 (a)) of the sample without the prelayer can be associated with misfit dislocations forming at the interfaces of the MQW structure generated by slip in the (0001) basal plane, since these dark lines do not appear in the CL intensity image of the GaN NBE emission (Figure 6.5 (c)). The more pronounced dark line on the right-hand side of the Figure 6.5 (c) is attributed to a stacking fault as it appears at the same place in both the GaN NBE and MQW intensity images. In contrast to stacking faults, misfit dislocations do not penetrate through the entire layer. They are generally generated at interfaces when a threading dislocation bends into the plane of the interface. Hence, a high density is observed in the MQW intensity image, but not in the GaN NBE intensity image. Comparison of the MQW intensity images of the samples with and without the prelayer shows that the sample with the prelayer exhibits a higher density of dark lines. This indicates that the sample with the SLS prelayer has a higher misfit dislocation density than the sample without a prelayer. Figure 6.6 shows the dark line densities estimated from the CL maps shown in Figures 4 a-d, which can be supposed to be proportion to the MD density [27]. Clearly, the inserted SL dramatically increases the dark line density under the MQWs from 0.25×10^5 cm^{-1} to 2.25×10^5 cm^{-1}. Meanwhile, in the MQW region, the dark line density is increased from 1.5×10^5 cm^{-1} to 2.8×10^5 cm^{-1}, which is in good accord with what discussed above. Thus, one can conclude that the existence of SL will increase the density of MDs in the MQW regions.

Additionally, the CL intensity image generated from the SLS peak (Figure 6.5 (d)) shows a high density of dark lines, implying that a large number of misfit dislocations were generated at the interfaces in the SLS prelayer even before the growth of the MQW structure. The generation of misfit dislocations for the sample without a prelayer is largely due to the InGaN/GaN MQWs as a result of the large lattice-mismatch between InGaN and GaN. However, the enhanced misfit dislocation observed on the sample with the SLS prelayer is clearly due to the SLS prelayer. The critical thicknesses for stress relaxation via the formation of misfit dislocations depends on growth orientation. Detailed studies confirm that the critical thickness of InGaN grown on (11-22) GaN is much thinner than for growth on c-plane GaN or (20-21) semi-polar GaN [26], [28]–[31]. Therefore, although the InN content in the InGaN of the SLS prelayer is as low as 3%, misfit dislocations are still generated. It therefore can be concluded that the insertion of the SLS indeed generates extra misfit dislocations.

Point defects such as nitrogen vacancies or surface point defects generated during high temperature growth of GaN layer. Common imaging techniques fail to capture these defects as it is one-dimensional and well below practical detection limits. However, based on previous study, the point defects can be captured by a low-temperature grown InGaN prelayer [10]–[12]. As a result, the performance of the semi-polar (11-22) LEDs with the SLS prelayer can be improved due to a reduction in point defect density. However, the insertion of the SLS also introduces extra misfit dislocations acting as NRCs, thus leading to a reduction in optical performance. The consequence of the competition of these two mechanisms leads to an improvement in optical performance, but the improvement is not as significant as that observed for its c-plane counterparts.

6.4 Conclusion

This chapter has systematically investigated the influence of an InGaN/GaN SLS prelayer inserted prior to the growth of the InGaN/GaN MQWs of a semi-polar (11-22) LED on patterned Si (113) on the optical performance. It was demonstrated that the semi-polar LED with the SLS prelayer exhibits an improvement in both IQE and light output as expected, which is similar to its c-plane counterparts. However, unlike c-plane LEDs, the SLS prelayer also introduces extra misfit dislocations. Consequently, the performance improvement is not as significant as that for its c-plane counterparts. For example, the IQE can be enhanced from 13% for the semi-polar LED without a prelayer to 23% for the semi-polar LED with a SLS prelayer (factor of 1.8), while the enhancement in IQE for its c-plane counterpart can be up to a factor of 3.5.

Reference

[1] T. Sugahara *et al.*, “Role of dislocation in InGaN phase separation,” *Jpn. J. Appl. Phys.*, vol. 37, no. 10B, p. L1195, 1998.

[2] R. D. Dupuis, J. B. Limb, J. Liu, J.-H. Ryou, C. Horne, and D. Yoo, “InGaN MQW green LEDs using p-InGaN and p-InGaN/p-GaN superlattices as p-type layers,” in *Gallium Nitride Materials and Devices III*, 2008, vol. 6894, p. 68941D.

[3] Y. Liu *et al.*, “Improved performance of GaN-based light-emitting diodes by using short-period superlattice structures,” *Prog. Nat. Sci. Mater. Int.*, vol. 20, pp. 70–75, 2010.

[4] T. Akasaka, H. Gotoh, T. Saito, and T. Makimoto, “High luminescent efficiency of InGaN multiple quantum wells grown on InGaN underlying layers,” *Appl. Phys. Lett.*, vol. 85, no. 15, pp. 3089–3091, 2004.

[5] N. Otsuji, K. Fujiwara, and J.-K. Sheu, “Electroluminescence efficiency of blue In Ga N∕Ga N quantum-well diodes with and without an n-In Ga N electron reservoir layer,” *J. Appl. Phys.*, vol. 100, no. 11, p. 113105, 2006.

[6] A. Hangleiter *et al.*, “Suppression of nonradiative recombination by V-shaped pits in GaInN/GaN quantum wells produces a large increase in the light emission efficiency,” *Phys. Rev. Lett.*, vol. 95, no. 12, p. 127402, 2005.

[7] P. T. Törmä *et al.*, “Effect of InGaN underneath layer on MOVPE-grown InGaN/GaN blue LEDs,” *J. Cryst. Growth*, vol. 310, no. 23, pp. 5162–5165, 2008.

[8] M. J. Davies *et al.*, “A study of the inclusion of prelayers in InGaN/GaN single-and multiple-quantum-well structures,” *Phys. status solidi*, vol. 252, no. 5, pp. 866–872, 2015.

[9] N. Nanhui *et al.*, “Improved quality of InGaN/GaN multiple quantum wells by a strain

relief layer," *J. Cryst. Growth*, vol. 286, no. 2, pp. 209–212, 2006, doi: 10.1016/j.jcrysgro.2005.09.027.

[10] A. M. Armstrong, B. N. Bryant, M. H. Crawford, D. D. Koleske, S. R. Lee, and J. J. Wierer Jr, "Defect-reduction mechanism for improving radiative efficiency in InGaN/GaN light-emitting diodes using InGaN underlayers," *J. Appl. Phys.*, vol. 117, no. 13, p. 134501, 2015.

[11] C. Haller, J. F. Carlin, G. Jacopin, D. Martin, R. Butté, and N. Grandjean, "Burying non-radiative defects in InGaN underlayer to increase InGaN/GaN quantum well efficiency," *Appl. Phys. Lett.*, vol. 111, no. 26, 2017, doi: 10.1063/1.5007616.

[12] C. Haller *et al.*, "GaN surface as the source of non-radiative defects in InGaN/GaN quantum wells," *Appl. Phys. Lett.*, vol. 113, no. 11, p. 111106, 2018.

[13] J. Bai *et al.*, "(11-22) semipolar InGaN emitters from green to amber on overgrown GaN on micro-rod templates," *Appl. Phys. Lett.*, vol. 107, no. 26, p. 261103, 2015.

[14] T. Wang, "Topical Review: Development of overgrown semi-polar GaN for high efficiency green/yellow emission," *Semicond. Sci. Technol.*, vol. 31, no. 9, p. 93003, 2016.

[15] T. Takeuchi, H. Amano, and I. Akasaki, "Theoretical study of orientation dependence of piezoelectric effects in wurtzite strained GaInN/GaN heterostructures and quantum wells," *Jpn. J. Appl. Phys.*, vol. 39, no. 2R, p. 413, 2000.

[16] J. E. Northrup, "GaN and InGaN (11 2_ 2) surfaces: Group-III adlayers and indium incorporation," *Appl. Phys. Lett.*, vol. 95, no. 13, p. 133107, 2009.

[17] A. Strittmatter *et al.*, "Semi-polar nitride surfaces and heterostructures," *Phys. status solidi*, vol. 248, no. 3, pp. 561–573, 2011.

[18] H. Sato *et al.*, "High power and high efficiency semipolar InGaN light emitting diodes," *J. Light Vis. Environ.*, vol. 32, no. 2, pp. 107–110, 2008.

[19] S. Yamamoto *et al.*, “High-efficiency single-quantum-well green and yellow-green light-emitting diodes on semipolar (2021) GaN substrates,” *Appl. Phys. express*, vol. 3, no. 12, p. 122102, 2010.

[20] S. Shen, X. Zhao, X. Yu, C. Zhu, J. Bai, and T. Wang, “Semi-Polar InGaN-Based Green Light-Emitting Diodes Grown on Silicon,” *Phys. status solidi*, vol. 217, no. 7, p. 1900654, 2020.

[21] J. H. Na *et al.*, “Dependence of carrier localization in In Ga N⁄Ga N multiple-quantum wells on well thickness,” *Appl. Phys. Lett.*, vol. 89, no. 25, p. 253120, 2006.

[22] R. Smith, B. Liu, J. Bai, and T. Wang, “Hybrid III-nitride/organic semiconductor nanostructure with high efficiency nonradiative energy transfer for white light emitters,” *Nano Lett.*, vol. 13, no. 7, pp. 3042–3047, 2013.

[23] B. Liu, R. Smith, J. Bai, Y. Gong, and T. Wang, “Great emission enhancement and excitonic recombination dynamics of InGaN/GaN nanorod structures,” *Appl. Phys. Lett.*, vol. 103, no. 10, p. 101108, 2013.

[24] J. Bruckbauer, P. R. Edwards, T. Wang, and R. W. Martin, “High resolution cathodoluminescence hyperspectral imaging of surface features in InGaN/GaN multiple quantum well structures,” *Appl. Phys. Lett.*, vol. 98, no. 14, p. 141908, 2011.

[25] P. S. Hsu *et al.*, “Misfit dislocation formation via pre-existing threading dislocation glide in (11 2¯ 2) semipolar heteroepitaxy,” *Appl. Phys. Lett.*, vol. 99, no. 8, p. 81912, 2011.

[26] I. L. Koslow *et al.*, “Onset of plastic relaxation in semipolar (112¯ 2) InxGa1− xN/GaN heterostructures,” *J. Cryst. Growth*, vol. 388, pp. 48–53, 2014.

[27] T. Lin, Z. Y. Zhou, Y. M. Huang, K. Yang, B. J. Zhang, and Z. C. Feng, “Strain-controlled recombination in InGaN/GaN multiple quantum wells on silicon substrates,” *Nanoscale Res. Lett.*, vol. 13, no. 1, pp. 1–7, 2018.

[28] C. A. Parker, J. C. Roberts, S. M. Bedair, M. J. Reed, S. X. Liu, and N. A. El-Masry, "Determination of the critical layer thickness in the InGaN/GaN heterostructures," *Appl. Phys. Lett.*, vol. 75, no. 18, pp. 2776–2778, 1999.

[29] A. E. Romanov *et al.*, "Basal plane misfit dislocations and stress relaxation in III-nitride semipolar heteroepitaxy," *J. Appl. Phys.*, vol. 109, no. 10, p. 103522, 2011.

[30] E. C. Young, C. S. Gallinat, A. E. Romanov, A. Tyagi, F. Wu, and J. S. Speck, "Critical thickness for onset of plastic relaxation in ($11\bar{2}2$) and ($20\bar{2}1$) semipolar AlGaN heterostructures," *Appl. Phys. Express*, vol. 3, no. 11, pp. 1–4, 2010, doi: 10.1143/APEX.3.111002.

[31] A. M. Smirnov, E. C. Young, V. E. Bougrov, J. S. Speck, and A. E. Romanov, "Stress relaxation in semipolar and nonpolar III-nitride heterostructures by formation of misfit dislocations of various origin," *J. Appl. Phys.*, vol. 126, no. 24, p. 245104, 2019.

Chapter 7

Conclusion and future work

This chapter firstly summarized the work which have been done during this project, then followed by potential approaches to further improve the performance of III-nitride based LEDs on silicon substrate as the future work.

7.1 Overgrowth and characterization of (11-22) semi-polar GaN on (113) silicon with a two-step method

A high crystal quality semi-polar (11-22) GaN on pattered (113) silicon substrate has been obtained by a two-step approach which can effectively eliminate melt-back etching even at high temperature over a long period of epitaxial growth. By means of plasma etching and anisotropic chemical etching, two (111) facets with an inclination angle of 58^{o} respect to c-direction and a (113) facet can be achieved. A thick AlN buffer layer with smooth surface and high crystal quality is grown on the silicon template by optimising the nucleation layer in order to provide a good coverage on the substrate to completely avoid the melt-back etching. Followed by selective area deposition with SiO_2 mask to ensure subsequent GaN growth can only performed on exposed (111) facets. As a result, a semi-polar (11-22) GaN with low basal stacking faults density and high crystal quality which are confirmed by low-temperature photoluminescence measurement and XRD measurement respectively. In addition, stimulated emission is observed with a low threshold at room temperature which further proves the excellent crystal quality. This approach is critical for the subsequent AlGaN growth on semi-polar GaN which requires high-temperature growth condition and able to demonstrate a high quality semi-polar (11-22) GaN film on silicon substrate.

7.2 Semi-polar InGaN-based Green Light-emitting Diodes Grown on Silicon

Based on previous approach, a one-step semi-polar (11-22) GaN growth on pattered (113) silicon substrate is developed by means of designing certain trench depth and introducing extra periodic gaps for the growth which does not require high temperature such as LED structure. As a result, semi-polar (11-22) GaN film is achieved with high crystal and low basal stacking fault density which are confirmed by X-ray rocking curve measurement and low-temperature photoluminescence measurement. Green (530nm) InGaN based light-emitting diodes are obtained on such high quality (11-22) GaN film. A significant reduction in polarization-induced piezoelectric fields is observed by excitation power-dependent photoluminescence measurements which is further confirmed the GaN materials grow along with semi-polar (11-22) direction can effectively supress the impact from internal polarization fields. In addition, electroluminescence exhibits a stable external quantum efficiency with increasing injection current compared with conventional c-plane LEDs. These results further validate the potential of manufacturing semi-polar LEDs on silicon substrates.

7.3 Investigation of the Influence of an InGaN Superlattice Prelayer on the Performance of Semi-polar (11-22) Green LEDs Grown on (113) Silicon Substrates

The last chapter has validated the potential for semi-polar (11-22) GaN materials to overcome the impact from QCSE. However, the efficiency is not showing a promising result due to the defect induced degradation from active region. Thus, a typical defect management for the MQW structure is investigated by inserting an InGaN/GaN SLS structure prior to the active region. The investigation of the influence of an InGaN/GaN SLS prelayer on semi-polar (11-22) InGaN based green LEDs is carried out by means of temperature-dependent PL, time-resolved PL, EL and CL measurements. Corresponding results exhibit that an enhanced performance in terms of IQE and light output is observed in semi-polar LED sample with SLS prelayer. Yet the improvement is not as tremendous as its c-plane case due to the extra misfit dislocations generated from the boundary between GaN buffer and SLS prelayer. Thus, the IQE of semi-polar LED with SLS prelayer only enhance with a factor 1.8 which is far from the factor of 3.5 enhancement in the c-plane case.

7.4 Future Work

For semi-polar (11-22) GaN growth with one-step approach, a large ratio of stripe width to spacing can be performed to further optimise the initial step growth and avoid the GaN footprint on the bottom of trench which is critical for the elimination of melt-back etching. In addition, silicon-on-insulator (SOI) substrate is another possible option which can effectively suppress the occurrence of GaN footprint on the bottom of the trench as shown in Figure 7.1.

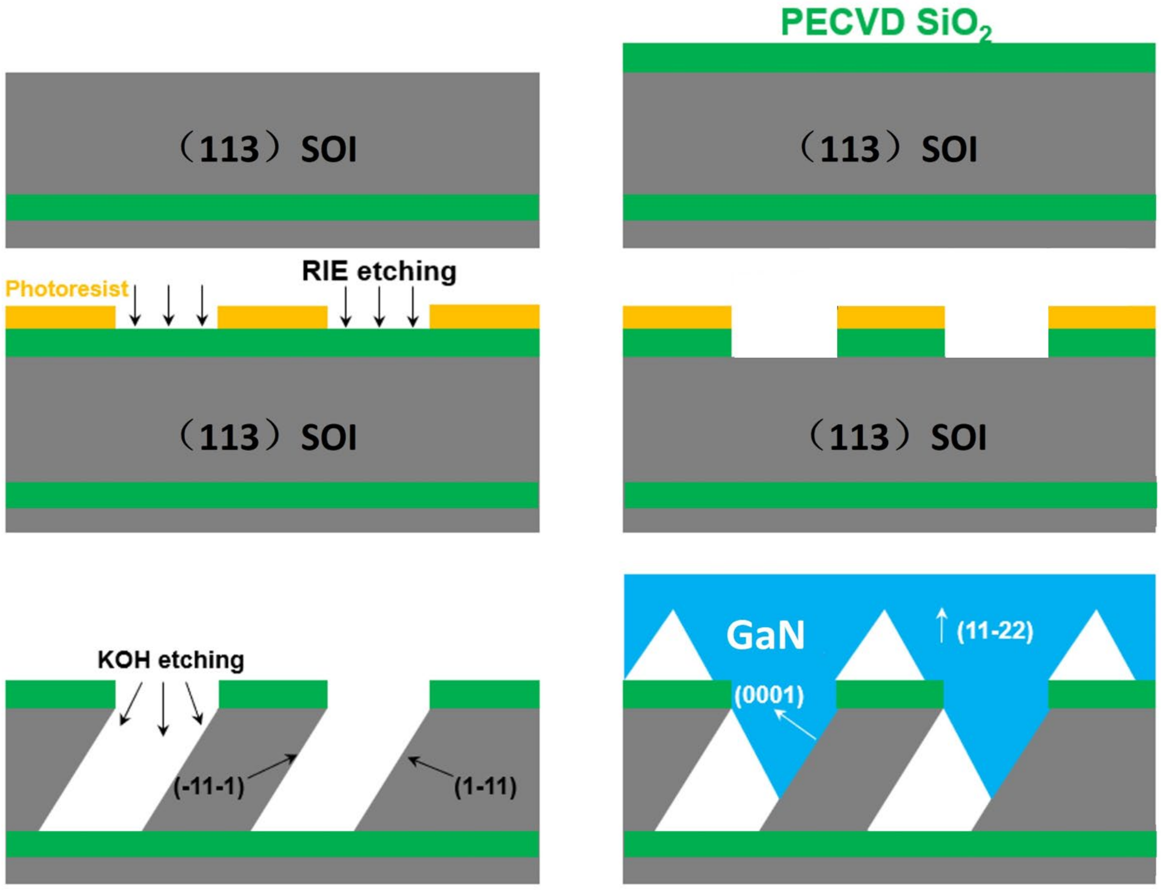

Figure 7.1: The schematic of semi-polar (11-22) LED structure growth process on patterned (113) SOI substrate.

The process of patterning SOI substrate is identical with previous as shown in Figure 5.2. After chemical wet etching process, the bottom of the trench is etched down to the SiO_2 interlayer and only expose (-11-1) and (1-11) Si facet. The MO precursors will find difficulty to nucleate on SiO_2 layer under high temperature due to the lack of similar crystalline structure, forming an absence of GaN footprint at the bottom of the trench. In the meantime, SOI substrate could also benefit the photonic integration and easy to fabricate to silicon waveguides in laser applications [1]–[3].

$In_{0.17}Al_{0.83}N$/GaN as SLS prelayer inserted prior to the MQW growth is a very promising solution for further improving the efficiency of semi-polar LEDs. Many reports have demonstrated InAlN alloy with indium content around 17-18% has lattice-matched with GaN [4]–[6] and successfully employed in III-nitride applications such as HEMTs on GaN buffer with a strain-free InAlN thin barrier [7], InAlN based electron blocking layer [8] and defect-free lattice-matched GaN/InAlN SLS distributed Bragg mirrors [9]–[11]. Similar approach has been demonstrated by W. Liu etc with 55 nm InAlN underlayer to control the defect density in active region. As a result, the PL intensity of the active region luminescence is enhanced by more than two orders of magnitude with reduced defect density [12]. Thus, a significant defect reduction especially for misfit dislocation density can be expected when $In_{0.17}Al_{0.83}N$/GaN SLS is adopted prior to MQWs structure, leading to a further improvement of quantum efficiency. In the meantime, indium atoms can stop the surface defects from penetrating to the active region, enhancing the performance of LEDs indirectly.

Reference

[1] M. W. Pruessner, T. H. Stievater, M. S. Ferraro, and W. S. Rabinovich, “Thermo-optic tuning and switching in SOI waveguide Fabry-Perot microcavities,” *Opt. Express*, vol. 15, no. 12, pp. 7557–7563, 2007.

[2] J. Van Campenhout *et al.*, “A compact SOI-integrated multiwavelength laser source based on cascaded InP microdisks,” *IEEE Photonics Technol. Lett.*, vol. 20, no. 16, pp. 1345–1347, 2008.

[3] S. Zamir, B. Meyler, and J. Salzman, “Reduction of cracks in GaN films grown on Si-on-insulator by lateral confined epitaxy,” *J. Cryst. Growth*, vol. 243, no. 3–4, pp. 375–380, 2002.

[4] K. Lorenz, N. Franco, E. Alves, I. M. Watson, R. W. Martin, and K. P. O’donnell, “Anomalous ion channeling in AlInN/GaN bilayers: determination of the strain state,” *Phys. Rev. Lett.*, vol. 97, no. 8, p. 85501, 2006.

[5] R. Butté *et al.*, “Current status of AlInN layers lattice-matched to GaN for photonics and electronics,” *J. Phys. D. Appl. Phys.*, vol. 40, no. 20, p. 6328, 2007.

[6] B. Gil, *III-Nitride Semiconductors and their modern devices*, vol. 18. OUP Oxford, 2013.

[7] M. Gonschorek, J.-F. Carlin, E. Feltin, M. A. Py, and N. Grandjean, “High electron mobility lattice-matched Al In N/ Ga N field-effect transistor heterostructures,” *Appl. Phys. Lett.*, vol. 89, no. 6, p. 62106, 2006.

[8] S. Choi *et al.*, “Improvement of peak quantum efficiency and efficiency droop in III-nitride visible light-emitting diodes with an InAlN electron-blocking layer,” *Appl. Phys. Lett.*, vol. 96, no. 22, p. 221105, 2010.

[9] J.-F. Carlin and M. Ilegems, “High-quality AlInN for high index contrast Bragg mirrors

lattice matched to GaN," *Appl. Phys. Lett.*, vol. 83, no. 4, pp. 668–670, 2003.

[10] G. Cosendey, A. Castiglia, G. Rossbach, J.-F. Carlin, and N. Grandjean, "Blue monolithic AlInN-based vertical cavity surface emitting laser diode on free-standing GaN substrate," *Appl. Phys. Lett.*, vol. 101, no. 15, p. 151113, 2012.

[11] J. Carlin *et al.*, "Progresses in III-nitride distributed Bragg reflectors and microcavities using AlInN/GaN materials," *Phys. status solidi*, vol. 242, no. 11, pp. 2326–2344, 2005.

[12] W. Liu *et al.*, "Impact of defects on Auger recombination in c-plane InGaN/GaN single quantum well in the efficiency droop regime," *Appl. Phys. Lett.*, vol. 116, no. 22, p. 222106, 2020.